

CONTROL SYSTEM FOR A HIGH PULSE-ENERGY
ATMOSPHERIC LIDAR

A Thesis
Presented
to the Faculty of
California State University, Chico

In Partial Fulfillment
of the Requirements for the Degree
Master of Science
in
Electrical and Computer Engineering

by

© Denton R Scott 2012

Fall 2012

CONTROL SYSTEM FOR A HIGH PULSE-ENERGY
ATMOSPHERIC LIDAR

A Thesis

by

Denton R Scott

Fall 2012

APPROVED BY THE DEAN OF GRADUATE STUDIES
AND VICE PROVOST FOR RESEARCH:

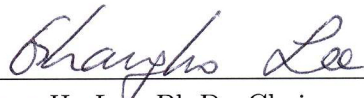


Eun K. Park, Ph.D.

APPROVED BY THE GRADUATE ADVISORY COMMITTEE:



Ben A. Juliano, Ph.D.
Graduate Coordinator



Ghang-Ho Lee, Ph.D., Chair



Anna Petrova-Mayor, Ph.D.



Shane D. Mayor, Ph.D.

PUBLICATION RIGHTS

No portion of this thesis may be reprinted or reproduced in any manner unacceptable to the usual copyright restrictions without the written permission of the author.

ACKNOWLEDGMENTS

The research described herein was supported by awards 0924407, 1104342, and 1228464 from the U.S. National Science Foundation's Physical and Dynamic Meteorology Program. The author thanks Dr. Laurie Albright and committee members for helpful suggestions in preparation of the thesis. Mr. Bruce Morley and Dr. Scott Spuler of the National Center for Atmospheric Research (NCAR) provided much appreciated technical assistance. The author thanks the many family members and friends that provided help and support.

TABLE OF CONTENTS

	PAGE
Publication Rights	iii
Acknowledgments	iv
Table of Contents	v
List of Tables.....	vii
List of Figures	viii
List of Abbreviations.....	xi
Abstract	xii
CHAPTER	
I. Introduction	1
Narration of Problem	1
Scope of the Thesis.....	2
Significance of the Thesis	3
Preview of Chapters 2 Through 5	5
II. Literature Review	7
Lidar History, Technology, and Uses.....	7
Control Theory	11
III. History and Components of the Raman-Shifted Eye-Safe Aerosol Lidar	15
History of the Raman-Shifted Eye-Safe Aerosol Lidar	15
Description of the Raman-Shifted Eye-Safe Aerosol Lidar as Currently Configured	17
IV. Experimental Procedures, Findings, and Solutions.....	22
System Variables.....	23

CHAPTER	PAGE
Laser Energy Control	38
Safe-Shutdown Feature	54
Contact Personnel Feature	57
Frequency of Control	58
Data Quality	64
Testing and Results	76
V. Summary	79
References	81
Appendices	
A. Future Work	93
B. An Overview of the LabVIEW Code for the REAL	102

LIST OF TABLES

TABLE		PAGE
1.	System Components and Corresponding Location Numbers for Fig. 5 and 6	25
2.	System Variable Measurements Distinguished by Dependency on Nd:YAG Laser Pulse	60
3.	Loop Process Time for Distinct Implementation Phases	62
4.	Full-Scale Programmable Input Range and Vertical Offset for the NI PCI-5122.....	65
5.	BSCAN Data File 30-Word Header Format	74

LIST OF FIGURES

FIGURE	PAGE
1. General Control System Diagram	11
2. Gain Scheduler Feedback Control System Diagram	12
3. Linear Feedback Control System Diagram.....	13
4. Photograph of the Lidar at the CSUC Farm.....	21
5. Cutaway of a Solid-Model of the Lidar System.....	26
6. Diagram of Component Placement on Optics Table	27
7. Control System Hardware Component Signal Flow Diagram	28
8. Photograph of the Two Gravity Referenced Tiltmeters	33
9. Photograph of the Precipitation Sensor	35
10. Photograph of the DataRay WinCamD Beam Profiler in the Transmitter of the Instrument	36
11. Typical Beam Profile Produced by the DataRay WinCamD CCD Camera	37
12. Time-Series of Several Vital Signs during the 2007 CHATS Experiment	39
13. Lidar Control System Diagram with Energy Feedback Loop	41
14. Time vs. Laser Energy and Conversion Efficiency during the 11 Increments of the Flashlamp Voltage	42

15.	Photograph of the Flashlamps Discharging in the Nd:YAG Laser Cavity	43
16.	Photograph of the Damaged Raman Cell Prism	44
17.	Color Negative Burn Paper Results from Flashlamp Voltage vs. Conversion Experiment	46
18.	Energy Density of the Nd:YAG beam at 1 μm vs. Distance from the Raman Cell Entry Window per Flashlamp Voltage	47
19.	Lidar Control System Diagram with Pulse Count Feedback Controller	49
20.	Vital Signs during the October 2012 Experiment using the Gain Scheduling Controller with Pulse Count Feedback ..	51
21.	A Comparison of Data from the CHATS Experiment and the Field Experiment with Flashlamp Voltage Control	53
22.	Photograph of Nd:YAG Laser PCU Power Key Turner	55
23.	Photograph of the Receiver Box Safety Shutter	56
24.	Backscatter Intensity Waveforms from InGaAs Detectors on Days with Clear Sky, Clouds, and a Smoke Layer	66
25.	Frequency Distribution of Single Pulse SNR of the Aerosol Backscatter Data as a Function of Range during the CHATS Experiment	67
26.	Frequency Distribution of Single Pulse SNR of the Aerosol Backscatter Data as a Function of Range during the Flashlamp Voltage Control Field Experiment	68
27.	Comparison of SNR Peak Distribution of the Aerosol Backscatter Data as a Function of Range during the Control System Field Experiment	70
28.	Distributions of Wind Velocity Component Differences as a Function of Average SNR	71

29.	Comparison of Unnormalized and Normalized Full Scan Data	72
30.	Magnified Comparison of Unnormalized and Normalized Full Scan Data.....	72
31.	BSCAN File Format Organization.....	73

LIST OF ABBREVIATIONS

BSCAN - format designator given to the raw REAL beam-by-beam data

BSU - Beam Steering Unit

CHATS - Canopy Horizontal Array Turbulence Study

CSUC - California State University, Chico

InGaAs - Indium Gallium Arsenide

Lidar - Light Detection and Ranging

LUT - Look-Up Table

Nd:YAG - Neodymium-doped Yttrium Aluminum Garnet

NI - National Instruments

PCU - Power and Cooling Unit

PID - Proportional, Integral, Derivative (control method)

REAL - Raman-shifted Eye-safe Atmospheric Lidar

RTOS - Real-Time Operating System

SNR - Signal to Noise Ratio

SRS - Stimulated Raman Scattering

UPS - Uninterruptible Power Supply

ABSTRACT

CONTROL SYSTEM FOR A HIGH PULSE-ENERGY ATMOSPHERIC LIDAR

by

© Denton R Scott 2012

Master of Science in Electrical and Computer Engineering

California State University, Chico

Fall 2012

A master's thesis that develops, tests, and implements a control system for a high pulse-energy atmospheric lidar system is presented. The control system senses in real-time system variables such as transmitter component temperature, pressure, and energy and diameter of high energy laser pulses and makes decisions on whether action is required. The control program can immediately and gracefully shut down the lidar if the system variable measurements exceed operator-defined thresholds. It can also inform operators of changes in system status. The control system includes a feedback loop to increase the Neodymium-doped Yttrium Aluminum Garnet laser flashlamp voltage incrementally thereby providing improved transmit pulse-energy stability over the 23 to 30 day lifetime of a flashlamp set. This control system facilitates unattended operation of the lidar over long periods of time with more uniform performance and the safety of a control system that can head off potentially catastrophic system failures.

CHAPTER I

INTRODUCTION

Narration of Problem

Improved spatial wind field and atmospheric boundary layer height measurements are needed in a number of practical applications. Wind resource assessment requires long-term monitoring to determine wind energy potential in challenging to reach locations and altitudes (for example, offshore measurements) [1]-[4]. Wind turbines are more efficient if incoming wind vector measurements are used to optimize the pitch of rotor blades and yaw of the hub [5]. Air quality forecasting can be improved with measurements of boundary layer height [6], [7]. Dispersion of potentially hazardous emissions from industrial sites can be tracked [8]. Airport safety and efficiency can be increased with observations of wake vortices and wind shears that may be hazardous to aircraft [9]-[11].

Scanning lidars enable remote observations of the two dimensional spatial structure and movement of the clear atmosphere. As a lidar scans, pulses of radiation propagate through the atmosphere illuminating volumes containing air molecules, aerosol particles, and hydrometers. A small portion of the radiation is scattered back to the lidar where the intensity is detected and recorded. Horizontal scans reveal the advection of features, such as aerosol plumes, as they drift with the wind. Vertical scans reveal the atmospheric boundary layer that tends to contain a higher density of aerosol particles in contrast to the rest of the troposphere which is

more clear. Computer algorithms can be applied to the image sequences to determine the wind field and atmospheric boundary layer height [12], [13].

The Department of Physics at California State University, Chico (CSUC) operates a scanning lidar for atmospheric research. This instrument is well-suited to measure the wind field and atmospheric boundary layer height as (1) the laser pulses emitted into the atmosphere have high peak power and yet are eye-safe, (2) cross-sections of the atmosphere are produced quickly (one scan approximately every 15 seconds), and (3) computer algorithms implemented by the research group can calculate two-component wind vectors from sequential scans and atmospheric boundary layer heights from individual scans [12].

The above applications require spatial wind field and boundary layer height measurements to be collected over long periods of time. In order to be cost-efficient and reliable over long periods of time (months, preferably years), the high pulse-energy atmospheric lidar at CSUC must operate continuously, unattended, and in a fail-safe manner. This study addresses these challenges.

Scope of the Thesis

This study develops a control system for a high pulse-energy atmospheric lidar to facilitate continuous, unattended, and fail-safe operation. System failure cases were analyzed and characteristics of the system operation were explored. Specific system components and processes were optimized to improve data quality and control. A field experiment was conducted with the proposed control system in place. Data were collected and performance was compared to that of a previous experiment that used a design with no control system [14]-[16]. Recommendations are provided for future work that will lead to enhanced performance.

Significance of the Thesis

This study represents a milestone in the development of the instrument at CSUC: the first automatic flashlamp voltage adjustment and fail-safe operation of the high pulse-energy atmospheric lidar. This instrument transmits high energy, eye-safe pulses into the atmosphere at a rate of 10 Hz. Each pulse produces backscatter radiation with a sufficiently high signal-to-noise ratio (SNR) that, after a 15 second scan of the atmosphere, spatial atmospheric structure is revealed to ranges typically up to 3 to 5 km. This high performance is largely the result of the high energy transmitter which, in particular, benefits from a control system.

The SNR of backscatter radiation data is affected by the conditions of the atmosphere as well as the performance of the instrument. For example, an increase in atmospheric particle concentration will result in stronger SNR. Similarly, reduction of electronics noise in the receiver subsystem will result in stronger SNR. Given a constant atmosphere, the SNR is strongly dependent upon the “power-aperture product” of the lidar [17]. An increase in SNR may be the result of an increase in power transmitted or an increase in receiver aperture size. There are different ways to obtain the same power-aperture product.

Consider two lidars with equivalent receiver apertures. One lidar transmits high energy pulses and the other low energy pulses. Both lidars can have the same power-aperture product if equal amounts of power are transmitted into the atmosphere. Transmit power is equal to the total transmit energy per unit of time. The lidar used in this study nominally transmits 170 mJ of energy into the atmosphere every 0.1 seconds. A lidar with a pulse-energy of 1 mJ could achieve an equivalent power-aperture product by integrating over the energy of 170 pulses emitted in the same 0.1 seconds time interval.

The lidar at CSUC transmits high energy pulses to facilitate rapid scanning of the atmosphere. High energy pulses produce sufficient SNR typically out to 5 km in range with one pulse and, therefore, eliminate the need to integrate over backscatter radiation from multiple pulses. In order to produce the high energy pulses, a flashlamp pumped Nd:YAG laser is used. As the cathodes deteriorates slightly with each pulse of the 20 million pulse lifetime (about 23 days) of each flashlamp set, the flashlamp energy emission decreases [18]. This decrease in flashlamp energy reduces the energy that produces 1 μm pulses in transmitter. This degradation, if left unchecked, ultimately results in slowly decreasing transmit energy of the lidar. Flashlamp voltage adjustment is, therefore, required to maintain the desired transmit energy level. In order for this high energy transmit pulse to be eye-safe, a Raman cell is used to convert the high energy 1 μm Nd:YAG pulse to a more eye-safe wavelength of 1.5 μm . Otherwise, the non-eye-safe nature of the high energy transmit pulse would limit the practical applications of the lidar.

Micropulse is a class of lidar that, in contrast to the lidar at CSUC, transmit low energy pulses that do not pose as great a risk to optics and system components. These pulses are typically produced by diode-pumped solid-state lasers that have a lifetime of more than a year (more than a billion pulses) and require no significant voltage adjustment to maintain a desired transmit energy level [19]. However, atmospheric micropulse lidars do not usually scan the atmosphere. To produce the equivalent SNR of a high pulse-energy lidar, a micropulse lidar must integrate over the backscatter radiation of multiple pulses (usually thousands). This integration necessitates slowing the scan in order to reveal small spatial scale aerosol features in the area of interest. Slowing a scan defeats the purpose which is to capture images before wind and turbulence have advected and distorted the aerosol features appreciably. Micropulse lidars typically

stare in a single direction and observe atmospheric particulate matter in the path (often a vertical column) of the pulses over time [20]-[22]. This method of observation is limited in comparison to the spatial atmospheric cross-sections observed over time with a scanning lidar.

Because the instrument used in this study incorporates a high pressure cell containing flammable gas and a laser that produces a beam capable of high energy densities, failures have the potential to escalate quickly. An increase in the energy density of the laser beam may damage optics and sensors in the system. Diffraction patterns caused by one damaged optic may lead to damage (such as coating failures and inclusions) on others as well. Although it has never happened, it is conceivable that such failures may initiate a chain of events culminating in a catastrophic failure such as a rupture in the window of the high pressure cell.

A control system is needed to detect and prevent problems from escalating during long-term, unattended operation of the instrument. The high pulse-energy atmospheric lidar at CSUC, with the control system presented in this study, will facilitate advancements in meteorological research by encouraging routine long-term, unattended use of the instrument in studies of the wind and atmospheric boundary layer height.

Preview of Chapters 2 Through 5

Chapter II is a brief review of the theories that apply to the lidar system used and control systems tested in this study. Chapter III is a history and technical description of the specific lidar system used in this study. Chapter IV describes the experimental work conducted, including sensors and subsystems used by the control system that was developed and tested. Chapter V is a summary of the thesis. Appendix A lists future engineering projects that would further improve the

lidar. Appendix B provides an overview of the control system as written in the LabVIEW programming language.

CHAPTER II

LITERATURE REVIEW

Lidar History, Technology, and Uses

Although the term lidar was not conceived until the 1950s, light detection and ranging technology have roots as far back as the 1930s. Even though lidar technology originated from searchlights and telescopes, in 1938 flashlamps were used to send pulses of light into the atmosphere that would reflect off cloud formations. Light pulse round-trip time measurements were used to calculate the altitude of clouds. This was the first application of atmospheric lidar [23].

The invention and development of the laser in the 1960s opened new possibilities for lidar technology [24]. Soon lidars were transmitting high energy pulses at specific wavelengths. This was the launch point from which both laser and lidar technologies rose to their present importance. Today lidar most commonly refers to the use of laser radiation detection. In 1976, E. D. Hinkley further validated lidar technology with the publication of the first lidar text book, *Laser Monitoring of the Atmosphere* [23], [25].

Today, lidar technology is commonly used for remote velocity detection of hard targets (lidar gun) [26]; terrain mapping [27]; scene scanning [28], [29]; and, as in this study, remote sensing of atmospheric and meteorological variables such as wind, aerosol, and boundary layer heights [30]-[36]. The instrument used for this study is an active, high pulse-energy, distributed target (atmospheric) lidar. It is distinct from hard-target lidars that have the benefit of a bright impulse returned

from solid objects. The atmospheric lidar must detect backscatter signal from microscopic particles distributed through the atmosphere.

Active vs. Passive Sensing

Active sensing technologies, such as lidar and radar, involve emitting energy and sensing the backscatter energy as it encounters targets of interest. In a lidar, a telescope collects this backscatter energy and, with the help of additional smaller optics, focuses it onto a photo detector. A passive sensing instrument (i.e., a radiometer) senses radiation from sources.

Cameras use both passive and active sensing. When capturing outside photographs on a sunny day, a common camera will sense that light is sufficient and not require a flash. This is passive sensing. A dark environment requires active sensing. Using the flash bulb, the camera emits broadband radiation and captures the radiation reflected from distant surfaces. The lidar in this study is an active sensing instrument and the subject is the clear atmosphere. However, unlike a camera, the lidar provides range-resolved information.

Hard vs. Distributed Target

Laser radiation from a lidar can be used to detect hard or distributed targets. Because hard target backscatter radiation is relatively intense, lidars for this application do not in general require high pulse-energy transmitters. Hard targets produce a large signal-to-noise ratio (SNR) impulse that allows precise measurements of round-trip time (for target distance measurements) or frequency shift (for target velocity measurements).

Lidars that sense distributed targets measure range-dependent, backscatter intensity from air particulate matter (aerosol particles), and hydrometers (clouds and precipitation) [37]-[39]. For example, when radiation is emitted into the atmosphere, the population of particles in the path of the pulse

scatter very low quantities of energy back to be detected by the instrument [37]. As the pulse propagates through the atmosphere, radiation is scattered and detected by the lidar as a function of time. The initial backscatter radiation detected represents aerosol backscatter intensity at short ranges and delayed radiation represents aerosol backscatter intensity at longer ranges. This backscatter energy can be detected until the pulse encounters a hard target or the pulse-energy is attenuated below an SNR equal to one. The targets detected in this study are distributed aerosol particles and any backscatter intensity data point represents the collective backscattering radiation resulting from a very large number of particles. This is a result of the size of the lidar pulse which illuminates a large volume of particles at any one instant.

A lidar that senses distributed targets may detect one or both of two forms of scattering: elastic or inelastic. Elastic scattering describes a process whereby radiation incident on a particle is redirected and no wavelength change occurs because the incident radiation is not absorbed by the particle. Inelastic scattering (includes, for example, Raman and fluorescence scattering) describes a process whereby incident radiation is absorbed by a particle and re-emitted as radiation at a different wavelength. Both elastic and inelastic scattering are involved in the lidar used in this study. The lidar detects *elastic* backscatter from atmospheric particles (radiation transmitted and radiation detected have the same wavelength of $1.5 \mu\text{m}$). However, *inelastic* scattering takes place in the Raman cell of the transmitter (radiation enters the cell at a wavelength of $1 \mu\text{m}$ and a percentage is absorbed and re-emitted at a wavelength of $1.5 \mu\text{m}$). The inelastic scattering in the Raman cell is known as stimulated Raman scattering (SRS). Therefore, the elastic lidar used in this study is not to be confused with “Raman

lidars” which detect inelastic backscatter radiation at a wavelength different from that transmitted [40]-[42].

Low vs. High Energy

Lidars may be categorized based on the manner in which they deliver power: high pulse rate, low energy pulses (micropulse) [43] and low pulse rate, high energy pulses [44]. In designing a lidar, engineers have the choice of transmitting one high energy pulse that could have the equivalent SNR of a large number of weaker pulses. Because of the reliability of a low pulse-energy transmitter, there are more low pulse-energy lidars in operation. A low pulse-energy laser requires a faster pulse rate to produce equivalent power and photon-counting (digital) receivers are generally used to detect the weak backscatter signal [31]. Low pulse-energy laser also present a lower risk to system components such as optics and sensors.

Alternately, a high pulse-energy laser presents a greater risk of damaging components during routine operation and, therefore, requires careful monitoring. However, the high pulse-energy laser does not need to pulse as frequently to produce the same average power as a low pulse-energy laser.

Though the most popular applications of low pulse-energy lidars sense hard target returns such as lidar guns, terrain mapping, and scene scanning, there are also distributed target applications for low pulse-energy lidars in atmospheric research [45]. High pulse-energy lidars are more commonly applied in the remote sensing of atmospheric quantities. This study uses a high pulse-energy lidar.

Rayleigh vs. Mie Scattering

Distributed targets scatter radiation in all directions as the pulses propagate through the atmosphere. Two theories describe how distributed targets of different size scatter electromagnetic radiation [46]. Two types of elastic scattering are Rayleigh and Mie. Rayleigh scattering theory describes the

redirection of electromagnetic radiation that occurs when the particles are much smaller than the wavelength of the radiation [47], [48]. For example, visible radiation with a wavelength of about 0.5 microns will cause Rayleigh scattering as it propagates through pure air since nitrogen and oxygen molecules are more than 1000 times smaller. The lidar used in the study transmits laser radiation at 1.54 microns wavelength. Therefore, Rayleigh scattering is also produced from the air [49]. However, the intensity of Rayleigh scattering scales as the one over wavelength to the 4th power. Therefore, Rayleigh scattering from the lidar is extremely weak. Most of the backscatter radiation detected by the REAL can be described through Mie Scattering theory which applies when the particles are spherical and approximately the same size as the wavelength of the radiation.

Control Theory

Control theory, an aspect of dynamic system engineering, guides a given system to a desired output by using a previous output to alter an input to that system. The control uses one or more system outputs in an algorithm that calculates the next input for the system. One or more system measurement outputs are input to the control as a feedback variable. Fig. 1 illustrates a general control system flow diagram.

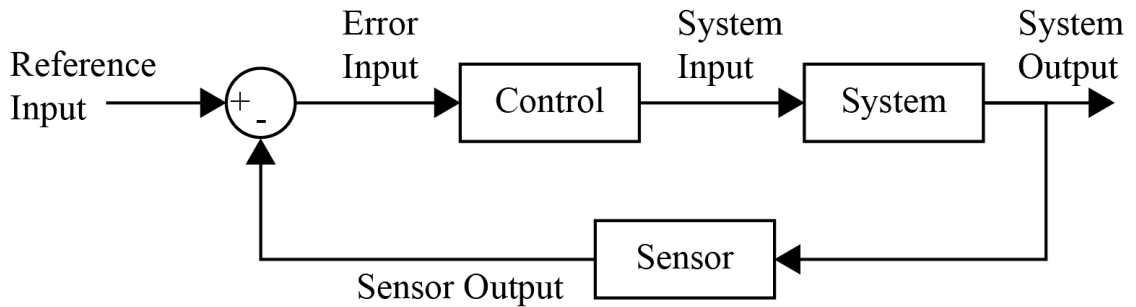


Fig. 1. General control system diagram.

Gain scheduling is one method of control. Gain scheduling maps a control input directly to a control output using a look-up table [50]. This is a common controller for simple, robust dynamic systems [51]. The control separates system operating conditions into areas to be analyzed individually. For the current area of operation, the pre-calculated control gains are applied to the control algorithm to produce the desired system response. Fig. 2 illustrates the system flow diagram.

Gain scheduler controllers have a wide range of applications, from linear controllers applied to known linear dynamic systems, to adaptive controllers applied to time-variant, nonlinear dynamic systems. The proportional, integral, and derivative (PID) controller is commonly used in conjunction with the gain scheduler method. Because each of the three gains correlates with a response characteristic, the PID controller is a comprehensive method of control. The proportional gain adjusts the rise-time, the integral gain adjusts the state-steady error, and the derivative gain adjusts the settling-time of the response.

Given the system characteristics in the form of a system transfer function and known operating conditions, the three PID controller gains can be calculated using a number of known methods. However, this control may perform

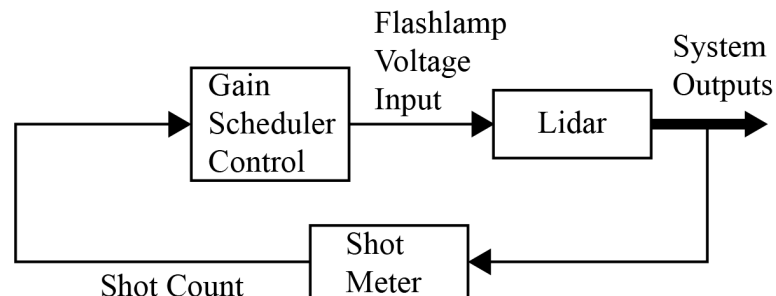


Fig. 2. Gain scheduler feedback control system diagram.

better under one range of operating conditions than another. The gain scheduling method calculates the three PID gains for several ranges of operation. These gains are then loaded into a look-up table in the controller design. As the system operating conditions change, the controller applies the gains optimally calculated for that range of conditions.

An airplane operating at a wide range of altitudes illustrates this method. The altitude control may be calculated to perform over the whole range. This may result in a desirable response at mid-range altitudes, but low and high altitude responses may suffer. A gain scheduler control could have three sets of control gains, one each for low, mid-range, and high altitude operating conditions. This same approach can also be used for the velocity control and other characteristics that change with operating conditions.

Linear feedback control is another method of control investigated in this study. This control produces a system input as a function of a system output measurement and a desired system output as shown in Fig. 3.

Submarine underwater depth is an example of a system implementing linear feedback control. Underwater pressure increases linearly as depth increases. Underwater pressure is directly related to underwater depth by a linear function.

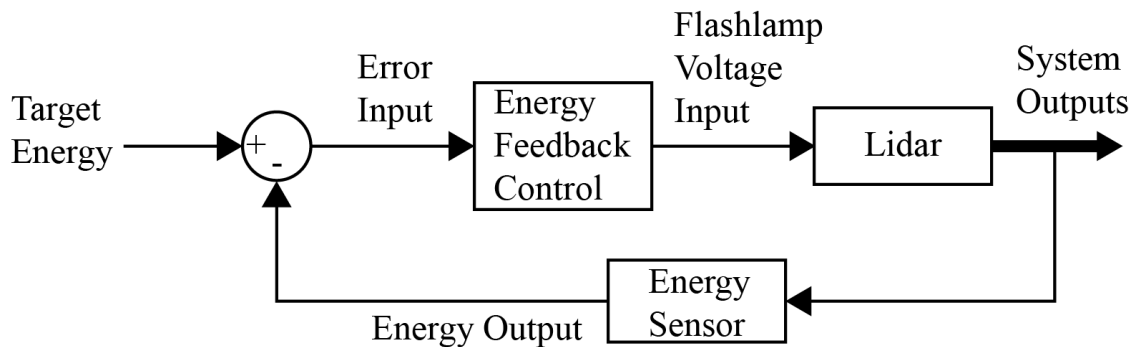


Fig. 3. Linear feedback control system diagram.

This facilitates the implementation of a linear feedback control that will adjust the system inputs to produce optimal performance at all depths.

For optimized computation, most dynamic systems utilize a real-time operating system or a microcomputer enabling extensive control of the timing and process allocation [52]. Even though a number of components in the lidar at CSUC could benefit from a dynamic control, this study is focused on performance stabilization, process synchronization, data acquisition, data transmission, and communication.

CHAPTER III
HISTORY AND COMPONENTS OF
THE RAMAN-SHIFTED EYE-
SAFE AEROSOL LIDAR

History of the Raman-Shifted Eye-Safe
Aerosol Lidar

Prior to the Raman-shifted Eye-safe Aerosol Lidar (REAL), high pulse-energy atmospheric lidars either presented ocular hazards or had limited performance capabilities [53]. The REAL successfully produces, with an eye-safe beam, high spatial and temporal resolution aerosol data with sufficient SNR to reveal atmospheric structure up to ranges of 3 to 10 km depending on atmospheric conditions.

The development of the REAL began in 2002 at the National Center for Atmospheric Research (NCAR) in Boulder, Colorado [54]. Dr. Shane Mayor and his group at NCAR were successful in creating an eye-safe lidar using SRS for wavelength conversion. The REAL nominally transmits 170 mJ pulses at a 10 Hz rate into the atmosphere. These parameters allow high spatial resolution scans to be produced at 15 second intervals typically.

The first major experiment involving the REAL was the Pentagon Shield field program in Washington, DC from April 9th to May 16th, 2004 [55]-[57]. The REAL was deployed as a surveillance instrument to reveal otherwise undetectable aerosol activity in the area. The experiment was successful, and in 2005 a

reproduction of the REAL was installed near the Pentagon and operated for over eight years [58]-[60]. Unfortunately, the control system of the reproduction was a proprietary component and the intellectual property was not shared for use in the prototype instrument.

The same REAL used in the Pentagon Shield field program was deployed in Dixon, CA, from March 15 to June 11, 2007 in the Canopy Horizontal Array Turbulence Study (CHATS) [14]-[16]. The REAL operated almost continuously at CHATS for three months and collected data that have been a subject of analysis since. Data and experience gained during the experiment have been useful in the continued refinement of the REAL.

Although the REAL has been deployed in multiple field experiments, the Pentagon Shield field program and CHATS represent milestones in the development of the instrument. The Pentagon Shield field program was the debut for the REAL as a scanning, eye-safe, and high pulse-energy lidar and was the first opportunity to demonstrate the capability in a dense urban environment. Similarly, CHATS was the first long-term (3 months) experiment that captured data from both horizontal and vertical scans of the atmosphere over an agricultural forest canopy. Within the CHATS data, density current fronts have been discovered [61] and two dimensional horizontal images of fine-scale canopy waves have been revealed [62]-[64].

In August 2008, the REAL arrived at California State University, Chico (CSUC). With the support of three grants from the National Science Foundation (NSF awards 0924407, 1104342, and 1228464), the REAL has been a source of research opportunities for students and faculty from several departments. Projects include analysis of fine-scale gravity waves, atmospheric boundary layer height analysis, wind vector algorithm development, web application development, and engineering projects [65].

Description of the Raman-Shifted
Eye-Safe Aerosol Lidar as
Currently Configured

Lidar Transmitter

The transmitter of the lidar has three main components: (1) a 1 μm wavelength, flashlamp-pumped, Nd:YAG laser; (2) a 1.5 μm wavelength seed laser; (3) and a Raman cell that facilitates SRS of the 1 μm wavelength energy. Together, the elements produce nominally 170 mJ pulses at a rate of 10 Hz at a wavelength of 1.5 μm . The beam is expanded to a 10 cm diameter before being projected into the atmosphere [53]. At this energy density and wavelength, the instrument is eye-safe according to the American National Standard Institute [66]. The Nd:YAG laser is a Continuum Surelite III capable of producing 900 mJ pulses at 1.064 μm , a pulse length of 6 to 9 ns, and a pulse rate of 10 Hz. The output energy of the laser can be adjusted by the flashlamp voltage and the Q-switch delay either manually from the front panel of the power and cooling unit (PCU) or remotely from a computer to the PCU through an RS-232 connection. The flashlamp voltage input range is 1.47 to 1.57 kV in increments of 0.01 kV.

The wavelength converter, the Raman cell, is a cylindrical chamber 80 cm in length that is pressurized with 9.5 parts methane and 4.1 parts argon to 1379 kPa (200 psi) [67]. A folded cell geometry with prisms enables the Nd:YAG beam to achieve a 3 meter interaction path length in the gas mixture. The Nd:YAG beam excites the methane in the cell and the first-Stokes SRS re-emits energy at a wavelength of 1.5 μm . The argon gas in the cell acts as a buffer gas to prevent Raman scattering at higher-order Stokes and anti-Stokes lines which are not necessarily in the eye-safe region of the spectrum and are capable of damaging

optics. Internal fans circulate the gas mixture to prevent thermal blooming from compromising the beam quality of subsequent pulses.

The Raman cell is injection seeded with a ThorLABS WDM8-C-33A-20-NM DFB laser that produces a continuous wave (cw) beam of 20 mW at $1.54373 \mu\text{m}$. This beam is essential in the Raman-shifting process, as it seeds the first-Stokes SRS process within the Raman cell. The seed laser improves the conversion efficiency by stabilizing the Stokes output and improves beam quality by reducing beam divergence [53], [57], [67]. The Nd:YAG laser can be injection seeded as well to increase the conversion efficiency further [67]. However, the system at CSUC does not currently contain such a feature.

Two beams exit the Raman cell: (1) the $1.5 \mu\text{m}$ wavelength, and (2) the residual $1 \mu\text{m}$ beam. They are physically separated by a prism in order to block the $1 \mu\text{m}$ beam.. When optimized, the SRS process using an unseeded Nd:YAG beam has a conversion efficiency near 30%. The nominal 170 mJ of $1.5 \mu\text{m}$ wavelength energy is typically sufficient to generate good SNR at ranges of up to 3 to 5 km or more, depending on atmospheric conditions and other aspects of instrument performance. Other factors that affect instrument performance include, for example, optical efficiency of the telescope and beam steering unit, alignment of the transmit beam and receive field-of-view, and gain and noise levels in the detection subsystem.

The optical components used in the $1 \mu\text{m}$ wavelength Nd:YAG beam (before reaching the Raman cell) include a Faraday isolator, a beam reducer, and 25 and 50 mm diameter turning mirrors. The $1.5 \mu\text{m}$ seed laser beam uses a collimator, isolator, half wave plate, and turning mirrors to co-align the seed laser beam with the Nd:YAG beam before it enters the Raman cell. A short-wave-pass dichroic mirror, pellen broca prism, holographic splitter, corner cube, and beam

block remove the excess $1.064 \mu\text{m}$ energy from the transmit beam. A beam expander lowers the energy density of the $1.5 \mu\text{m}$ wavelength pulses to be eye-safe. Turning mirrors direct the transmit beam into the atmosphere through the beam steering unit (BSU). Two Molectron energy meters and a DataRay WinCamD Beam Profiler monitor transmitter performance. A temperature sensor and pressure sensor monitor the Raman cell.

Beam Steering Unit

The elevation over azimuth style BSU, designed and built at NCAR, directs both the transmit beam and the receiver field of view in the atmosphere. The BSU is a series of two Zerodur, gold-coated, light-weight mirrors on rotating axes. Two Anamatic servo motors, SM2340D and SM3420D, rotate the azimuth and elevation mirrors, respectively. The elevation motor receives power and communication through a 16-channel slip-ring to facilitate continuous scanning in one direction. Each mirror is designed to have a flatness of within 3 wavelengths ($0.9 \mu\text{m}$ of sag) across the full aperture [54]. The beam steering unit operates on a control loop independent from the program being executed on the system PC. Once issued a command, the BSU motors will repeat the command without further communication with the lidar control program until another command is issued.

Receiver and Data Acquisition

The primary telescope mirror, 40.6 cm in diameter, collects backscatter radiation and focuses it into a receiver subsystem [54]. The receiver is composed of a collimating lens, a set of neutral density filters, an interference filter, a half-wave plate, and a beam splitter. The beam splitter separates the two polarization components of the backscattered radiation and each is focused on to a detector. The detectors are InGaAs avalanche photodiodes (Perkin Elmer part number C30659-1550-R2A). The InGaAs detectors [53] produce a voltage waveform

representing backscatter energy received as a function of time. The backscatter energy waveform is amplified with an AD829 [37] and digitized by a National Instruments (NI) PCI-5122 digitizer operating at 100 MS/s with a 14-bit resolution. The digitizer is read by a LabVIEW program being executed on the system PC, a Dell T7500 running a Windows 7 Professional 64-bit operating system with an Intel(R) Xeon(R) E5620.

The REAL is connected to the network on the main campus by a 2 km wireless connection to the CSUC Farm office and another 6 km wireless connection to campus. The connection to the CSUC Farm office is a 36 Mb/s, 2-channel connection. The bandwidth between the CSUC Farm office and the campus is 400 Mb/s.

Container and Environment

A custom-designed shipping container (6 x 2.5 x 2.5 meters) houses the lidar on a flat-bed semi-truck trailer as shown in Fig. 4. Air conditioning units, heating units, and insulation keep the container temperature-controlled independent of instrument operation and a HEPA filter system purges the transmitter subsystem with particle-free air. Temperature within the housing container varies between 22 to 28 degrees Celsius. The optical components are mounted on a 5-meter-long optics table. Interior environmental sensors include temperature sensors, platform attitude sensors, a utility power sensor, and a security system.

The lidar is located at the California State University, Chico (CSUC) Farm, 3 km outside the city limits of Chico, California and 6 km from the CSUC campus. The instrument is surrounded by fields of corn, alfalfa, sunflowers, and almond orchards. The weather is similar to a typical Mediterranean climate - dry and sunny from spring to the fall and rain in the winter.



Fig. 4. Photograph of lidar at the CSUC farm. The container on the left is used as a field office. The container on the right houses the lidar. The BSU is on the top of the right container.

LabVIEW Language and Signal Flow

The majority of the system that operates and controls the lidar is written in LabVIEW, a graphical object language. National Instruments (NI) develops and supports this language and hardware products that easily interface with LabVIEW programs. The program used to operate the lidar implements a state machine that executes a main loop upon receiving a trigger signal from the Nd:YAG laser.

The original LabVIEW program that controlled the REAL when it arrived at CSUC was written by Mr. Bruce Morley at NCAR. It provided basic ON/OFF capabilities for the instrument. This program was rewritten as this study developed and new features were added. The resulting program uses many of the same sub-programs while implementing multiple new control features, a restructured state machine, and multiple redesigned processes. The REAL LabVIEW program is detailed further in Appendix B.

CHAPTER IV
EXPERIMENTAL PROCEDURES,
FINDINGS, AND SOLUTIONS

The high pulse-energy atmospheric lidar at CSUC is a scientific instrument used in meteorological research. The lidar provides detailed wind field and atmospheric boundary layer measurements over several square kilometers. In the system's transmitter, a high pulse-energy 1 μm wavelength laser pulses at a rate of 10 Hz. These pulses are coaligned with a seed laser through a pressurized gas cylinder called a Raman cell. A portion of the 1 μm laser energy entering the Raman cell is converted from the 1 μm wavelength to an eye-safe 1.5 μm wavelength with an efficiency of about 30%. The residual 1 μm energy is separated from the laser path before the 1.5 μm energy is expanded and projected into the atmosphere by the beam steering unit (BSU). The backscatter radiation (which is extremely low energy) is collected by a primary telescope mirror and directed toward two avalanche photodiode detectors, each 200 μm in diameter, in the receiver subsystem. The design, testing, and implementation of the control system for this instrument required organizing dependencies between control loop frequencies, variable characteristics, process execution, and operating system constraints.

The design presented in this study incorporates control system design concepts applicable to systems with a process loop distinct from that of the control loop. Every system design has a timing aspect that plays a vital role in the effectiveness of the control. Although it is generally better to apply a control

sooner than later, the quality of the control depends on the data collected since the application of the previous control. Just as the operating system is the brain, the sensors are the fingers that sense instrument performance. Quality of operation depends largely on analog-to-digital converters (ADC) that read sensors and digital-to-analog converters (DAC) that apply controls.

The frequency at which system variables are sampled and controls applied determines the design of the code layout and hardware that control the instrument. System variable measurements are recorded and used to flag the “safe-shutdown” and “contact personnel” features of the control system. The voltage applied to the flashlamps pumping the Nd:YAG laser is stepped over time in an effort to stabilize the transmit energy. Data quality is improved through a redesign of the backscatter data normalization algorithm and the implementation of a control that can utilize one of the digitizer resolution settings available for reading the photo detectors.

System Variables

The high pulse-energy atmospheric lidar used for this study transmits laser pulses at a wavelength that is obtained through a process known as stimulated Raman scattering (SRS). This process introduces components into the system than would otherwise not be present such as a Raman cell pressurized with flammable gas. This, along with the high pulse-energy Nd:YAG laser, could potentially cause failures that are hazardous to components in the system.

An image of the container housing the lidar is shown in Fig. 5 with the locations of components and sensors as indicated. The optical table is similarly illustrated in Fig. 6. All the sensors throughout the instrument are read by ADCs and the measurements are input to the main program being executed on the

system PC in the housing container. The main program then executes the control algorithm that produces system flags to shut down gracefully, contact personnel, or adjust the flashlamp voltage to stabilize transmit energy as described in Fig. 7. Herein, the term “vital signs” refers specifically to at least the following system variables: Nd:YAG beam energy, transmit beam energy, wavelength conversion efficiency, and transmit beam radius. Otherwise, the term “system variables” refers to all variables used by the program operating the system. The location numbers in Fig. 5 and 6 are described in Table 1 with vital signs indicated with a \star .

Most system variables are sampled at a rate of 10 Hz with each pulse from the Nd:YAG laser. Samples are averaged over the period of time required to make one cross-sectional scan of the atmosphere. Therefore, one set of system variable measurements corresponds to one scan. These once-per-scan records are created, but not used, by the control system. These records allow for trends and correlations to be identified between system variables during post-operation processing and analysis performed by operators. For example, a correlation could be investigated between the temperature of the Nd:YAG laser cavity and the beam energy or radius.

TABLE 1
SYSTEM COMPONENTS AND CORRESPONDING LOCATION
NUMBERS FOR FIG. 5 AND 6

System Component	Location Number
Transmitter optics table	1
Receiver optics table	2
★Energy meter for 1.064 μm beam	3
★Energy meter for 1.543 μm beam	4
Temperature sensor for housing container	5
Temperature sensor for optics table	6
Nd:YAG laser head	7
Temperature sensor for Nd:YAG laser head	7
Raman cell	8
Temperature sensor for Raman cell	8
Pressure sensor for Raman cell	9
CCD camera to monitor ★ beam radius and centroid position of the transmit beam	10
Precipitation sensor	11
Nd:YAG PCU - reads flashlamp count and flashlamp voltage	12
Sensor for absolute platform attitude	13
Sensor for utility power	14
InGaAs Detector Control Voltage	15
InGaAs detectors	15
Sensor for BSU direction/movement	16
System PC - execute LabVIEW program, monitor available disk space, and calculate ★ Raman cell conversion efficiency	17
Launch mirror	18
Primary mirror	19

A list of the system components with the corresponding location number for Fig. 5 and 6. In some cases location number labels are used to represent multiple components due to size and limited detail of figures.

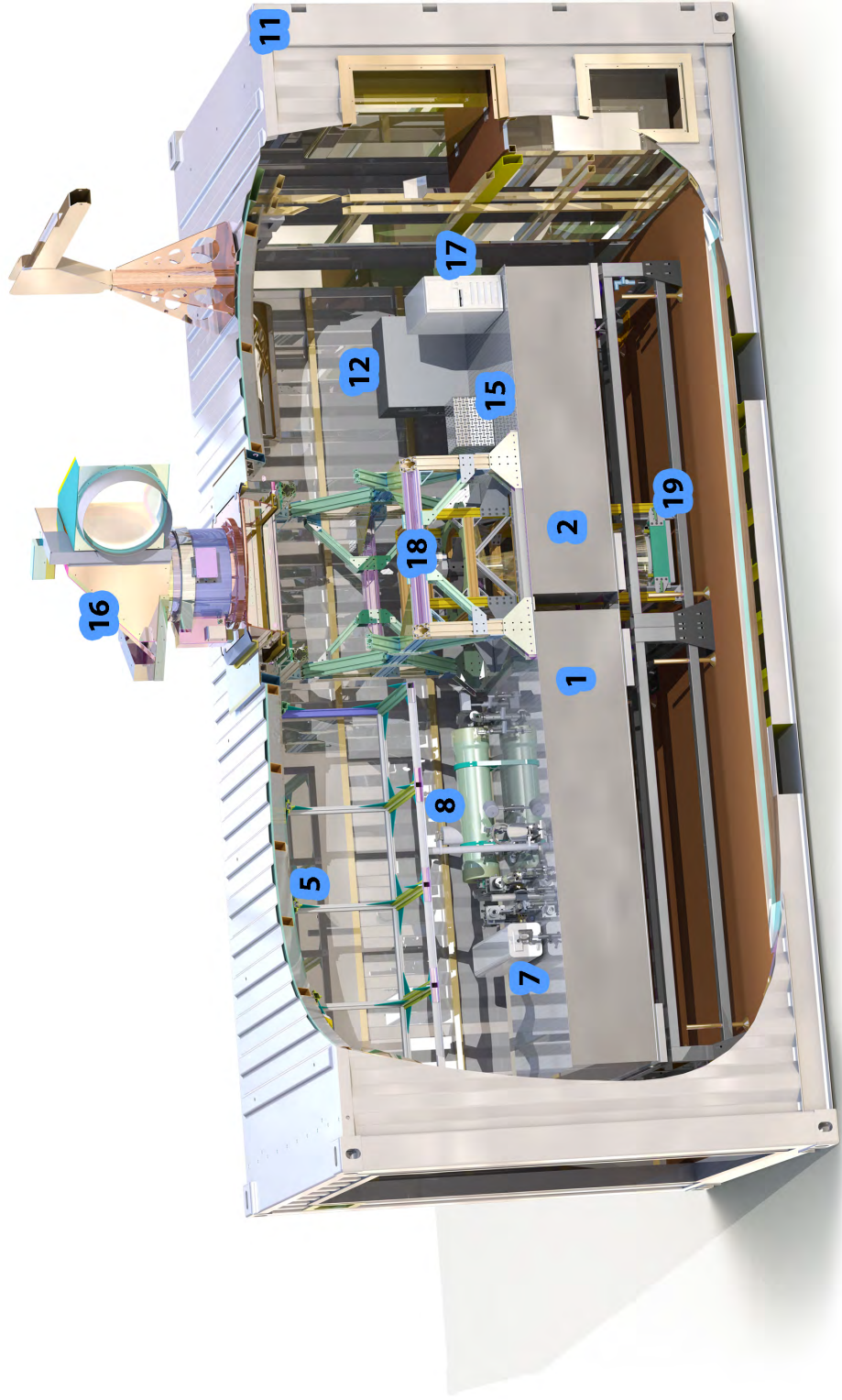


Fig. 5. (Color required.) Cutaway of a solid-model of the lidar system. Location number labels described in Table 1.

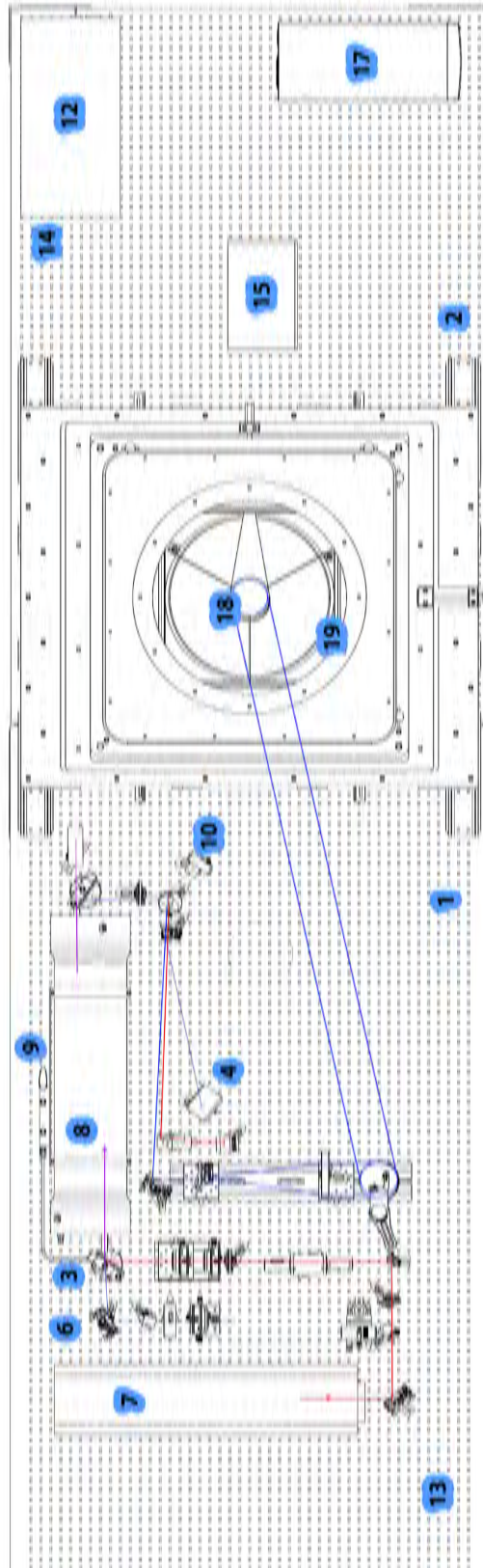


Fig. 6. Diagram of component placement on optics table. Location number labels described in Table 1.

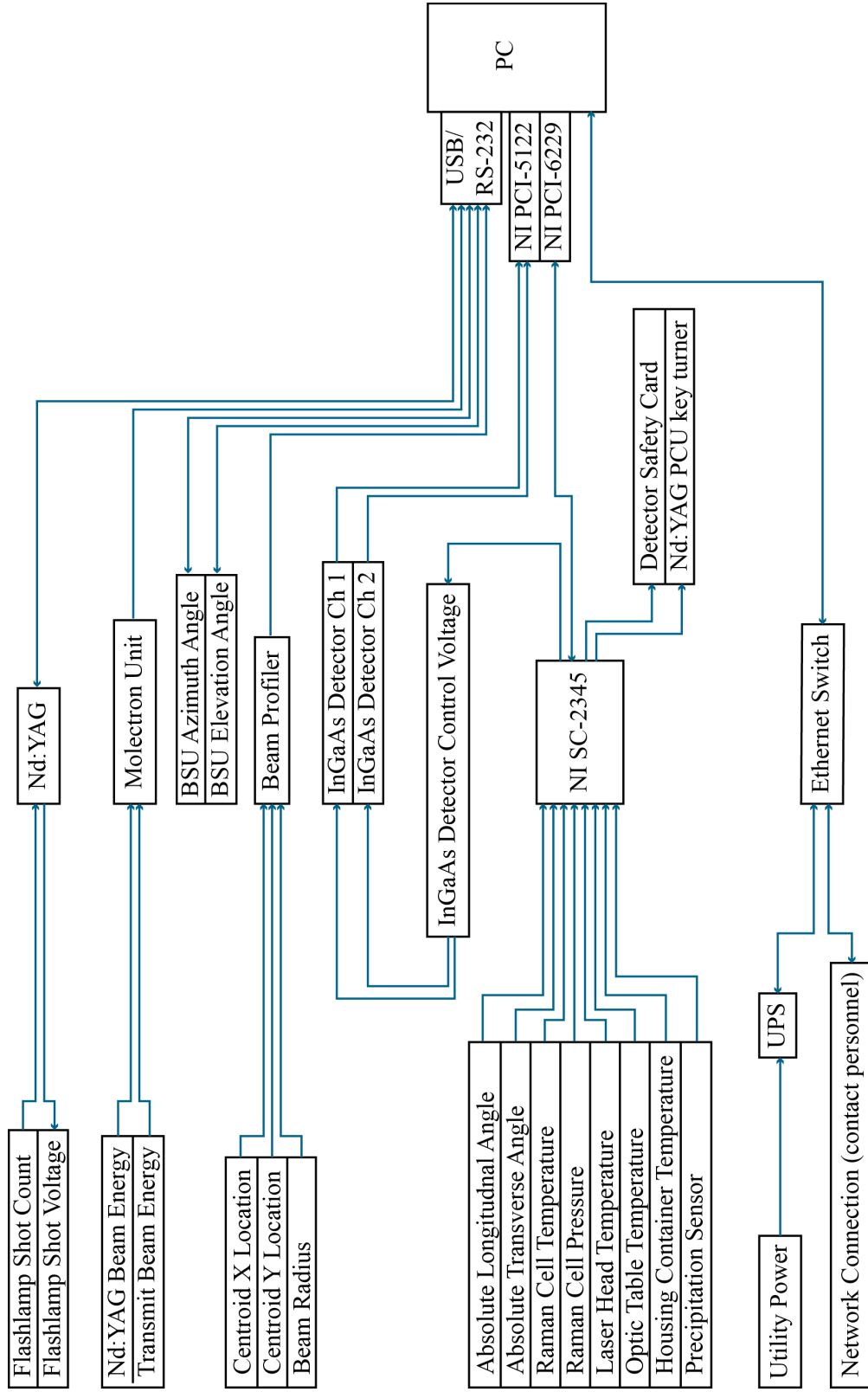


Fig. 7. Control system hardware component signal flow diagram.

Temperature Sensors

Sensors monitor the temperature of the interior of the housing container, the optics table surface, the Nd:YAG laser head, and the exterior surface of the Raman cell. Though extreme temperatures may cause or be symptoms of failures in the system, even small variations in temperature do indeed affect the overall performance of both the transmitter and the receiver. One hypothesis is that temperature variation affects thermal lensing in the Nd:YAG rod that changes the convergence and energy density and therefore conversion efficiency. In the receiver, the InGaAs detector sensitivities also vary with temperature [37]. Three of the sensors are K type thermocouples read by the National Instruments (NI) SC-2345 with three NI SCC-TC01 modules. The container temperature sensor is a pt 3750 type resistance temperature detector read by the NI SC-2345 with a NI SCC-RTD01. The InGaAs detectors in the receiver also have a built-in temperature sensing diode to adjust a bias voltage for stability in detector sensitivity.

Pressure Sensor

The Raman cell is pressurized with 9.5 parts methane (CH_4) and 4.1 parts argon (Ar) to 1310–1448 kPa. A decrease in pressure will affect the wavelength conversion efficiency and result in a decrease in transmit energy [53]. A sudden decrease in pressure from a leak in the Raman cell will cause the release of the flammable gas into the instrument housing container. The pressure is measured using an Ashcroft 2F249 pressure transducer which is read by the NI SC-2345 with a NI SCC-FT01 module. The SCC-FT01 measures the voltage drop created as the 4–20 mA output of the transducer passes through an external 249 ohm resistor.

Energy Meters

Two pyroelectric Molelectron energy meters quantify the total energy in each pulse just before entering the Raman cell and again after exiting the Raman cell. Before the Raman cell, the total energy of the 1 μm Nd:YAG pulse is measured. After the Raman cell, the total energy of the 1.5 μm transmit pulse is measured. The efficiency of the stimulated Raman scattering in converting the wavelength of the pulse in the Raman cell is a key indicator of system performance. These two energy readings are used to calculate this conversion efficiency.

$$\text{conversion efficiency percentage} = \frac{\text{Energy at } 1.543 \mu\text{m}}{\text{Energy at } 1.064 \mu\text{m}} \times 100 \quad (1)$$

Flashlamp Pulse Count and Voltage

The Nd:YAG Continuum Surelite III laser includes a head unit with a power and cooling unit (PCU) that are located approximately 5 m apart on the optics table. The PCU and laser head are connected by water lines, power cables, and control cables, each approximately 7 m in length. The main LabVIEW control program interfaces with the PCU via RS-232. The two commands that are used most frequently are a flashlamp pulse count read and a flashlamp voltage write. Other commands check for errors, turn the flashlamps ON or OFF, turn the laser head shutter ON or OFF, adjust the Q-switch delay (pulse-energy), adjust the pulse rate, and open or close the communication port.

The flashlamp pulse count command returns the number of pulses the Nd:YAG laser has discharged in its lifetime. This metric is used in the transmit energy control algorithm. At the beginning of this study the unit's pulse count was 86 million. The flashlamp count is determined by subtracting the number of pulses on the unit when the present flashlamps were installed. The flashlamp voltage is

the output of the laser energy control algorithm. This voltage is written to the unit on startup and during operation once per scan.

Beam Steering Unit Direction and Movement Sensors

The elevation over azimuth style beam steering unit (BSU) operates on a control loop independent from the main system. At the beginning of operation, the BSU receives a command that is stored within the BSU motor onboard computers and repeatedly executed until a different command is issued. A command is generally a scan sequence such as: (1) initial azimuth and elevation angles, (2) a scan rate, (3) final azimuth or elevation angle for horizontal or vertical scans, respectively, then (4) a reset to the initial angles. Two Anamatic servo motors, SM2340D and SM3420D, rotate the azimuth and elevation mirrors, respectively. If the power to the motors is interrupted, the motors will stop and require a reinitialization before continuing. Reinitialization is required for correct azimuth and elevation axis orientation. Power and communication to the BSU motor controlling elevation are delivered through a 16-channel slip ring to enable continuous scanning in one direction. The BSU is bolted to a large tip-tilt stage attached to a tower made of 80/20 extruded aluminum. This tower is fastened to the transmitter/receiver optics table so that the BSU and optics table form a monolithic structure independent of the housing container.

Prior to this research, the encoders built into the BSU motors were determined to be insufficiently accurate. Angular decoders were installed that produce measurements with 10^{-4} of a degree precision. The decoders are read by the NI SC-2345 through digital counter ports. These high precision decoders allow for a more accurate and reliable measuring of the BSU direction. However, due to the nature of scan sequence types and timing, the control algorithms for the BSU

are limited. For example, a new scan is defined as the moment the current BSU angle is greater than the previous angle. The scan has ended when the current angle is less than the previous angle. This assumes that the lidar will always scan in the same direction, which is true as currently configured. A freeze (failure caused by momentary loss of power) is defined to be true after a pre-determined number of seconds pass without the start of a new scan. A future feature will include a timed scan interval in which each scan will commence after a operator-defined interval of time greater than the length of the scan. This will be done by recognizing that a scan has been completed and commanding the BSU to return to point in the start direction and hold. The moment the scan interval has elapsed, the program will issue a command to the BSU to begin scanning again. This feature is needed to produce scans and wind measurements at consistent, operator-defined intervals, and to coordinate scans with other lidar systems in field research.

Absolute Attitude Sensors

The high pulse-energy atmospheric lidar can collect backscatter signal from ranges of more than 10 kilometers. Any pitch or roll movements in the housing of the instrument will result in a beam displacement in the atmosphere. Two Applied Geomechanics Model 801 Tuff Tilt Uniaxial Tiltmeters are used to monitor the pitch and roll of the instrument. Each tiltmeter has an angular range of ± 0.5 degrees and a resolution of 10^{-6} degrees. These gravity-referenced electrolytic tilt transducers produce a voltage read by the NI SC-2345 using a NI SCC-FT01. A photograph of the two tiltmeters is shown in Fig. 8.

The longer-term goal for these devices is to use them for precise laser beam positioning at far ranges. Pitch and roll measurements will be used to adjust BSU elevation angle just before each laser pulse to compensate for movement in the instrument and maintain precise control of the altitude of the beam above the



Fig. 8. Photograph of the two gravity referenced tiltmeters. The sensors measure pitch and roll angles of the instrument to 10^{-6} of a degree.

surface of the earth. Instead of micro positioning the housing container, any tip or tilt in the instrument will be compensated for in the pointing direction of the BSU. Because the BSU and the optics table form a monolithic structure, the sensors can be placed on the optics table and provide the pitch and roll adjustments necessary to point the BSU in the desired direction. The incremental progress made toward that goal during this thesis research project was to specify and procure the sensors, install and interface them, and record the angles. Further description is found in Appendix A.

Utility Power Meter

The lidar system receives electrical power from the local utility. Uninterruptible power supplies (UPSs) are installed that can maintain power to the instrument for about a half an hour following a power outage. In the case of a power outage, network cards in each UPS alert the control system and the instrument shuts down gracefully in less than a minute. It is possible that a power

outage could prevent communication with personnel through the Ethernet network connection. The security system, which can operate by battery for days, has a feature that uses GPRS (cellphone) communication channels to contact personnel in the event of a power outage.

Disk Space Meter

The computer executing the control system program has two physically independent 2 terabyte hard disk drives for storage of the backscatter data. The files on each disk are duplicates (RAID 1) for safety. The available disk space is monitored and personnel are notified or the system is shut down if the available space is less than a predetermined threshold. Disk space usage rate depends on the resolution and range of data being saved. Two terabytes of data (saving data to 5.8 km range at 1.5 meters per gate at 10 Hz) will be recorded after three months of continuous operation which corresponds to three sets of flashlamps.

Precipitation Sensor

Operation of the lidar is not optimal when precipitation is falling. Precipitation attenuates the transmitted pulses and backscatter radiation which significantly limits the range of useful data. In addition, the BSU azimuth motor is more exposed to precipitation when the BSU is scanning the atmosphere, and water drops on the face of the protective glass BSU window cause unwanted backscatter of the transmit beam and obstruct the receiver field of view. Therefore, a Thies Clima 5.4103.10.700 precipitation monitor detects hydrometers and flags the control system to enter a sleep mode. This sensor activates a relay when 1 to 15 drop incidences are detected and switches back 25 to 375 seconds after the last drop incidence, as set by the operator. The precipitation sleep mode stops operation, stows the BSU into a protective posture covering the azimuth motor, and allows

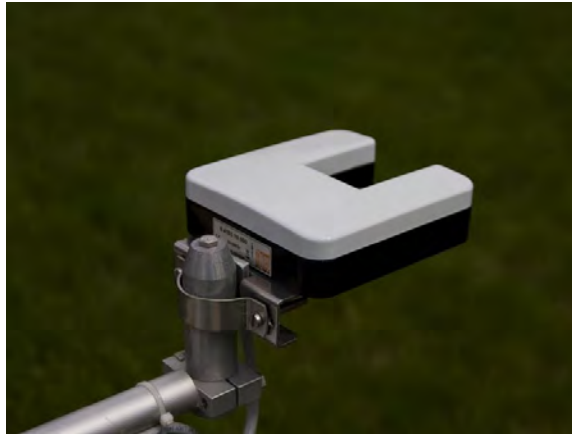


Fig. 9. Photograph of the precipitation sensor. The system enters a sleep mode when the precipitation sensor detects rain.

the system to sleep and then wake to continue operation after precipitation has stopped. A photograph of the precipitation monitor is shown in Fig. 9.

Beam Profiler

The Nd:YAG laser beam profile is monitored constantly with a DataRay WinCamD-UCD12. This sensor is a CCD camera that, with the DataRay software, can display the laser beam cross-section. The profiler is interfaced into the control system and drivers are used to extract three variables from the camera: centroid's X location and Y location, and beam radius. These measurements are made from the raster image produced by the CCD camera and an algorithm on board the camera's computer. The DataRay software shows high beam energy density as warm colors (i.e., white, red) and low energy density as cool colors (i.e., blue, green). Centroid location is determined to be the center of total energy density. The beam radius is measured at the $\frac{1}{e^2}$ level as for a Gaussian beam profile. Power and communication are delivered via USB. The device is not fast enough to capture each pulse at 10 Hz and therefore measurements may be held for two to three pulses

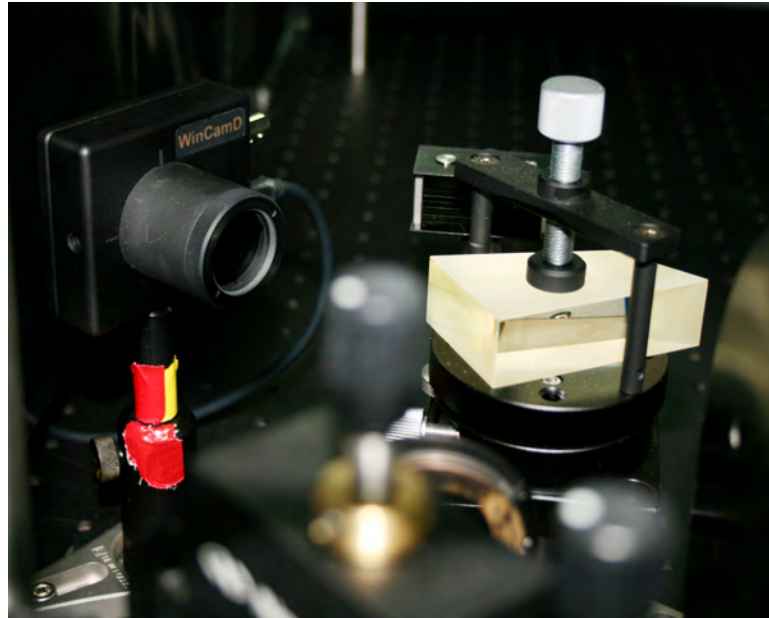


Fig. 10. Photograph of the DataRay WinCamD beam profiler in the transmitter of the instrument. The pellin broca prism that directs a sample of the Nd:YAG laser beam to the CCD camera is shown on the right side of the photograph.

before a new measurement is made. A photograph of the CCD camera is shown in Fig. 10 and Fig. 11 shows an example of the raster image produced by the sensor.

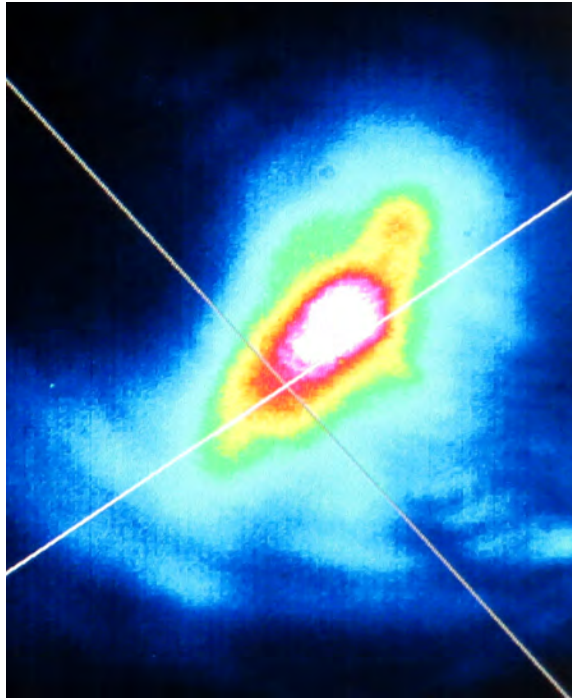


Fig. 11. (Color required.) Typical beam profile produced by the DataRay WinCamD CCD camera. The cross-section shows the center of the beam to have a high energy density with the centroid indicated by the intersection of the two lines.

InGaAs Detector Control Voltage

The parallel and perpendicular polarized components of the backscattered radiation are focused onto two Perkin-Elmer C30659-1550-R2A InGaAs Avalanche Photodiode Detectors in the receiver subsystem. This compact detector has an active area of 0.03 mm^2 . The detector has a pre-amplifier and a temperature diode that is used to control the bias voltage that regulates detector sensitivity. The temperature diodes are monitored by the NI SC-2345 using two NI SCC-FT01 modules. The input is processed and bias voltages are driven using another pair of NI SCC-FT01 modules. The output waveforms of the detectors

each pass through a post-amplifier before being read by the NI PCI-6229 high speed digitizer.

Laser Energy Control

During the Canopy Horizontal Array Turbulence Study (CHATS) experiment of 2007 the flashlamp voltage was increased manually with computer every week or so and could not be changed unless the system was stopped. Truly continuous operation requires that the voltage be changed without interrupting data collection. Unattended operation requires that this change be made without the assistance of an operator. When this requirement is met, the constraint on continuous operating time is the life of the flashlamps, between 23 and 34 days of round-the-clock operation. A trained person may change the flashlamps in less than 30 minutes.

Vital sign and system temperature data from the CHATS experiment are displayed in Fig. 12 [68]. Notice the transmit (SRS) energy at $1.5 \mu\text{m}$ on the lower graph has a sawtooth pattern. The steady increase in beam size and decrease in transmit energy is due to the aging of the flashlamps in the Nd:YAG laser. After the transmit energy has decreased by some amount, an operator manually incremented the flashlamp voltage in an effort to increase the transmit energy back to the original level.

Manual voltage adjustment during the experiment was inconsistent with varying increment size and interval. The voltage increment range is between 1.47 and 1.57 kV with minimum increments of 0.01 kV. This represents 11 available voltage settings for the lifetime of a set of flashlamps. According to the CHATS record, which spans the life of three sets of flashlamps, the voltage would have had to be adjusted 4 or 5 times during the life of a flashlamp set as indicated by the

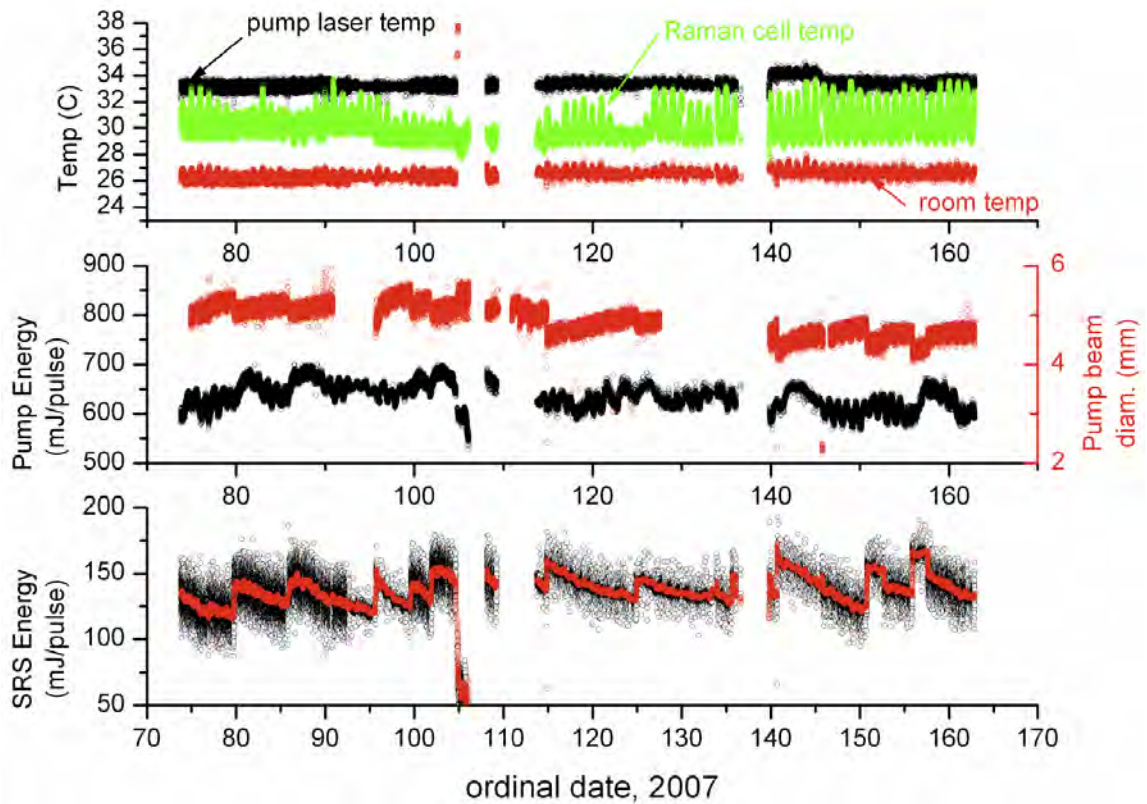


Fig. 12. (Color required.) Time-series of several vital signs during the 2007 CHATS experiment. This experiment was performed from March 19 to June 11, 2007 with no control system. The X-axis units are Julian days of the year 2007. The sawtooth shape of the transmitted (SRS) energy (bottom plot) is a result of aging of the flashlamps and manually increasing the flashlamp voltage periodically.

steps in the bottom plot of Fig. 12. Sometimes the voltage was increased by just 0.01 kV and other times by 0.02 kV. This does not take full advantage of the 11 flashlamp voltage settings available. This study identified two methods of flashlamp voltage control: a linear feedback method and a gain scheduler method.

The linear energy feedback control is designed to stabilize the laser beam energy by adjusting the voltage regardless of the increment size and interval required. In other words, stabilization can be achieved by changing the voltage by any amount as frequently as needed. In contrast, the gain scheduler control is

designed to change the voltage at fixed increments and time intervals regardless of whether the laser energy is at the desired level or not.

Linear Energy Feedback Control

The linear energy feedback control was the first control method investigated in this research. This control type uses operator-set transmit energy level thresholds to trigger incremental increases in the flashlamp voltage as the average transmit energy decreases with time. The feedback control is designed to produce an optimal laser energy over the life of the flashlamps. The feedback control may or may not use all 11 flashlamp voltage settings and it may or may not adjust the voltage at equal intervals. This method is designed to keep the energy at or above a operator-specified value. This method is designed to produce a beam energy that is constant over the lifetime of the flashlamps.

A critical piece of the design of the linear feedback control method is the operator-defined energy threshold, shown as the input in Fig. 13, that triggers the voltage incrementation. If the energy threshold is too low, the voltage will not optimally use all 11 values of incrementation that are available and will therefore produce a lower transmit energy over the life of the flashlamps. At the end of their lifetime, the flashlamps would theoretically have “life” remaining. However, if the energy threshold is too high, the voltage will increment too quickly and use all 11 values of incrementation before appropriate for the age of the flashlamps. At best, this would produce a higher transmit energy over the life of the flashlamps but exhaust their range of control quickly. At worst, the voltage would increase faster than the flashlamps are designed to operate, thus shortening their lifetime. Limits might need to be enforced on the control voltage to prevent a “run-away” voltage.

This method also assumes that the pulse-energy decreases linearly over the lifetime of a flashlamp set. This is a theory that has not yet been confirmed. If

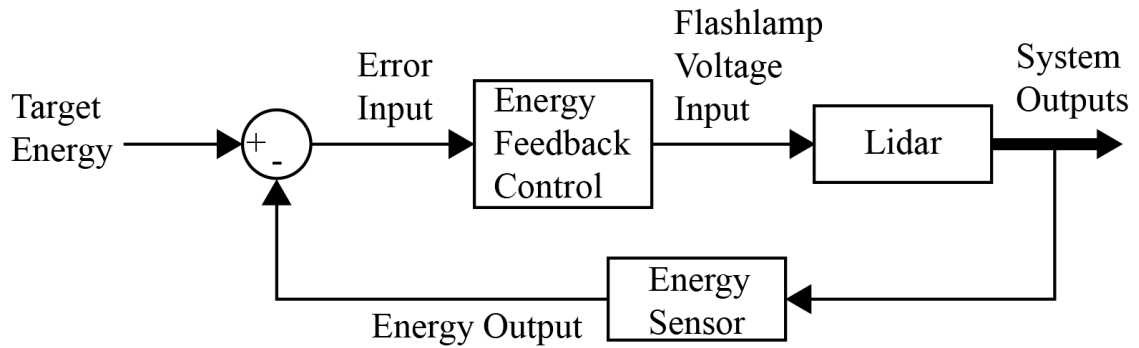


Fig. 13. Lidar control system diagram with energy feedback loop.

the theory is wrong and the beam energy decreases non-linearly then a constant energy threshold may not be appropriate. Such a non-linear feature in the system would require a more complicated algorithm. A flashlamp voltage experiment was devised to study the effect this control system might have on the performance of the instrument.

Flashlamp Voltage Experiment

To study how the flashlamp voltage affects the performance of the instrument, an experiment was conducted. For 1 hour the system was operated for 5 minutes at each of the 11 flashlamp voltage settings with less than 2 minutes of rest between each interval. During the 2 minutes of rest, the flashlamps were not pulsing while the voltage was being adjusted. Performance was recorded and three variables are displayed in Fig. 14. A photograph of the flashlamps discharging in the laser head cavity is shown in Fig. 15.

The 1 μm Nd:YAG laser energy (top, Fig. 14) increases in a step-like fashion but both the transmit energy (middle, Fig. 14) and the conversion efficiency (bottom, Fig. 14) increase steadily and then level off about halfway through the experiment. Toward the end of the experiment even a slight decrease was noted in the trend of each variable. After completion of this experiment it was

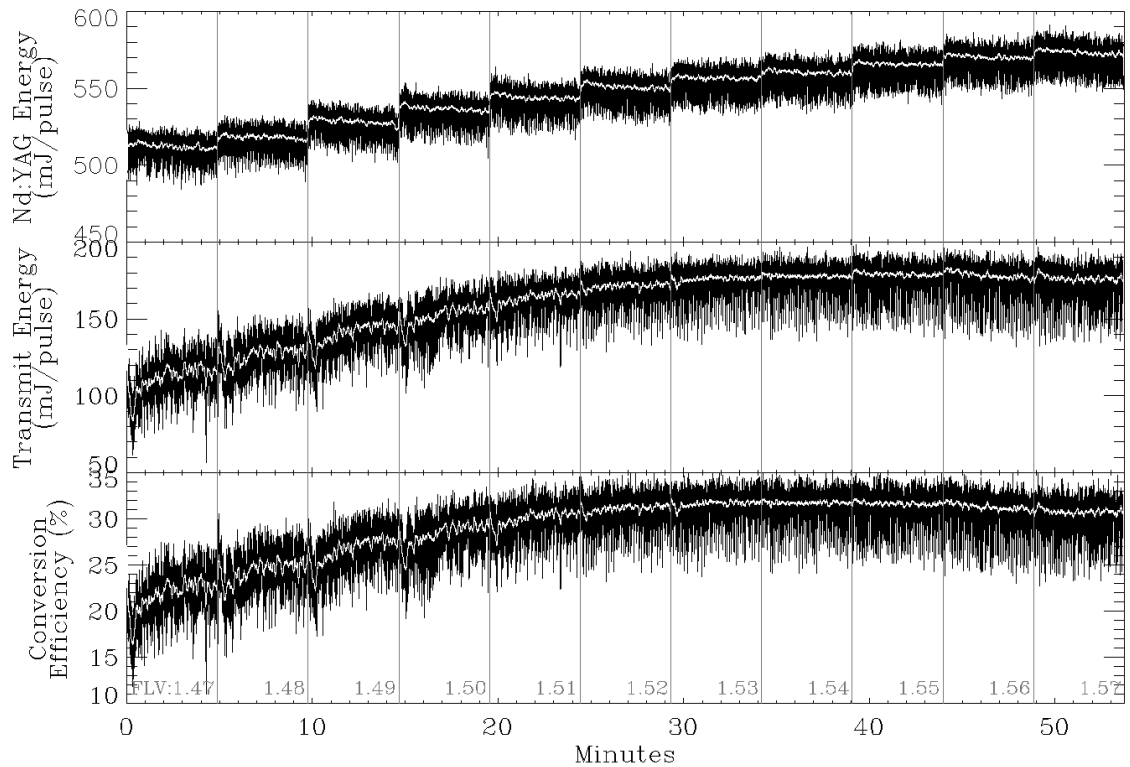


Fig. 14. Time vs. laser energy and conversion efficiency during the 11 increments of the flashlamp voltage. The system was operated for approximately five minute periods at each of the 11 flashlamp voltage levels beginning with 6,393,146 pulses on the flashlamps. This was a study of the effect of the flashlamp voltage on the vital signs of the instrument.

concluded that the system should be operated at the flashlamp voltage corresponding to the maximum conversion efficiency, about 1.55 kV. This voltage represents the voltage that the linear energy feedback control would determine appropriate to maximize transmit energy. Prior to this experiment, the flashlamp voltage was set to 1.47 kV for the current flashlamps.

At this point it is noted that the manual for this Nd:YAG laser indicates that a flashlamp set may be used for 20 to 30 million pulses. The pulse count for the beginning of this experiment was 6,393,146 pulses which represents between 21-32% of the lifetime of the flashlamp set. If the voltage increments were

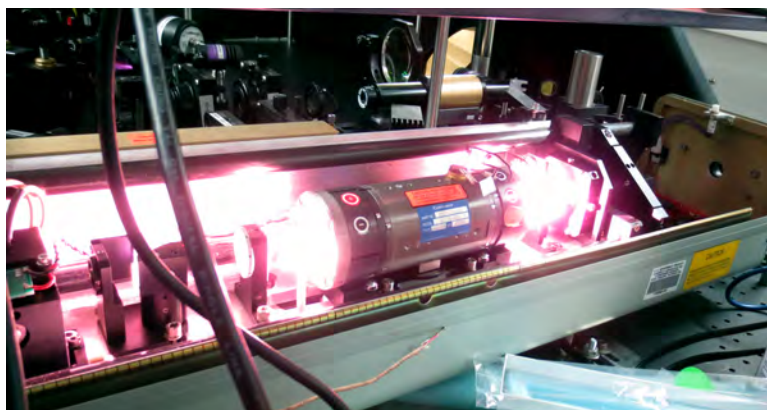


Fig. 15. Photograph of the flashlamps discharging in the Nd:YAG laser cavity.

distributed over the lifetime of the flashlamps evenly, the 6,393,146 pulse count would correspond to a setting between 1.49 and 1.51 kV.

The instrument was operated for a 10-hour day with the flashlamp voltage set at 1.55 kV and then shut down by the operator. The next morning the instrument was restarted. After one and a half hours a failure occurred. Fortunately, a section of the fail-safe feature of the control system (discussed in the next section of this chapter) was already implemented and it detected the failure which manifested as a sudden decrease in transmit energy. The fail-safe feature shut the instrument down quickly (after 500 ms or 5 pulses) and gracefully before the failure could affect other components of the system.

Investigation revealed that one of the four prisms in the Raman cell had been damaged. It was hypothesized the prism may have been damaged by an increase in energy density in the beam through the Raman cell. An experiment was devised to validate this theory.

Beam Conversion Through Raman Cell Experiment

At the time of the failure of the Raman cell prism, there were 10,779,826 pulses on the flashlamps. Again, it is noted that this corresponds to 36 to 54% of the life of a flashlamp set. Also, if the voltage increments were distributed over the lifetime of the flashlamps evenly, the 10,779,826 pulse count would correspond to a setting between 1.50 and 1.53 kV.

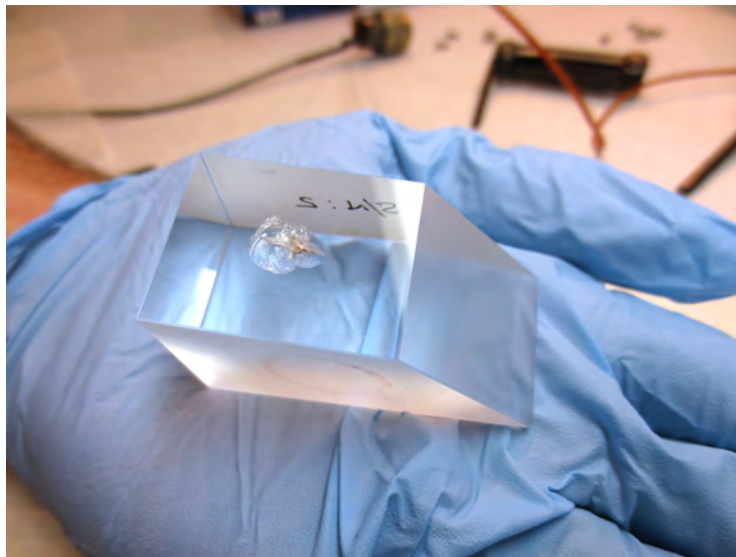


Fig. 16. Photograph of the damaged Raman cell prism.

After removing and repairing the Raman cell, data analysis was performed to estimate the $1 \mu\text{m}$ wavelength energy density through the Raman cell. It was expected that increasing the flashlamp voltage moved the waist of the beam from beyond the Raman cell where it should be, to inside the Raman cell. If this expectation were true, the waist, being the point of smallest beam cross-section and

thus highest energy density, could have been located on or near a prism and caused the damage.

The system is designed with the waist of the beam beyond the Raman cell because, although high energy densities improve wavelength conversion efficiency, the waist of the beam may have high enough energy density to optically break down the gas and cause sooting [69], [70]. A slight convergence of the beam through the cell provides optimal conversion efficiency while preventing damage to the optics.

The beam energy density through the Raman cell was measured using laser burn paper to measure the beam radius at 20 cm increments for 3 meters starting from the position of the entrance window of the Raman cell. This length represents the path length of the beam folded in the Raman cell. Fig. 17 displays the results of the experiment. The images in Fig. 17 are a negative color representation of what appears on the burn paper for clarity in print. The burn paper is actually black and burn spots are white and yellow.

Several characteristics of the beam are identified in this experiment by visual inspection of the burn paper. The first is that the overall shape of the beam profile changes with an increase in either distance or voltage. The beam profile starts as an oval shape and changes to the diamond-star shape with four distinct corners. The measurement at 180 cm with a voltage of 1.55 kV was erroneous and therefore, was omitted from the figure, and was interpolated based on neighboring data points. Conversion trends are readily apparent as the voltage and distance increase.

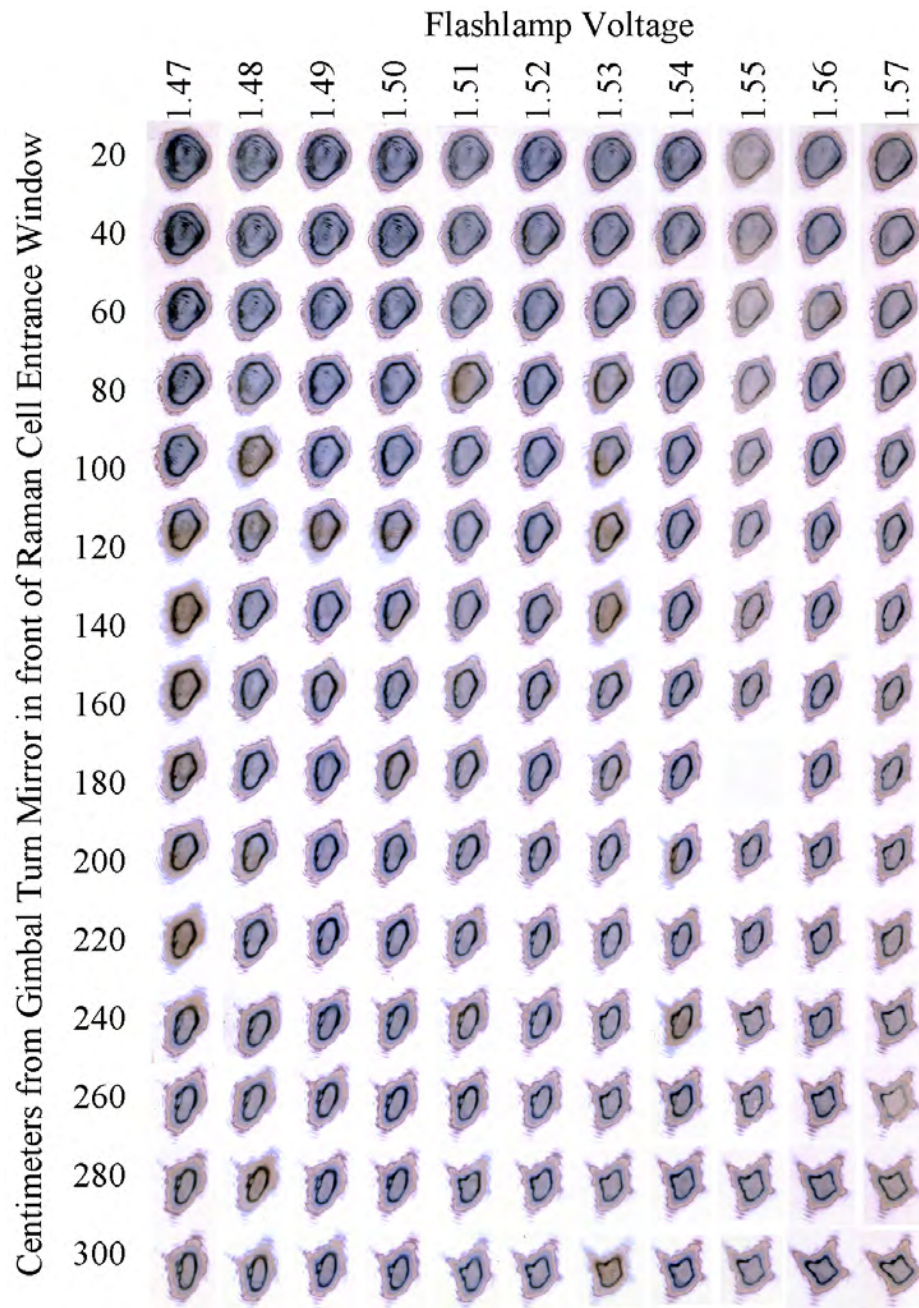


Fig. 17. (Color required.) Color negative burn paper results from flashlamp voltage vs. conversion experiment. ZAP-IT laser alignment paper was set at distances between 20 and 300 cm, at increments of 20 cm, from the mirror that turns the beam into the Raman cell. This was repeated for each of the 11 flashlamp voltage settings available to measure beam energy density, beam waist movement, and beam profile shape through the Raman cell vs. flashlamp voltage.

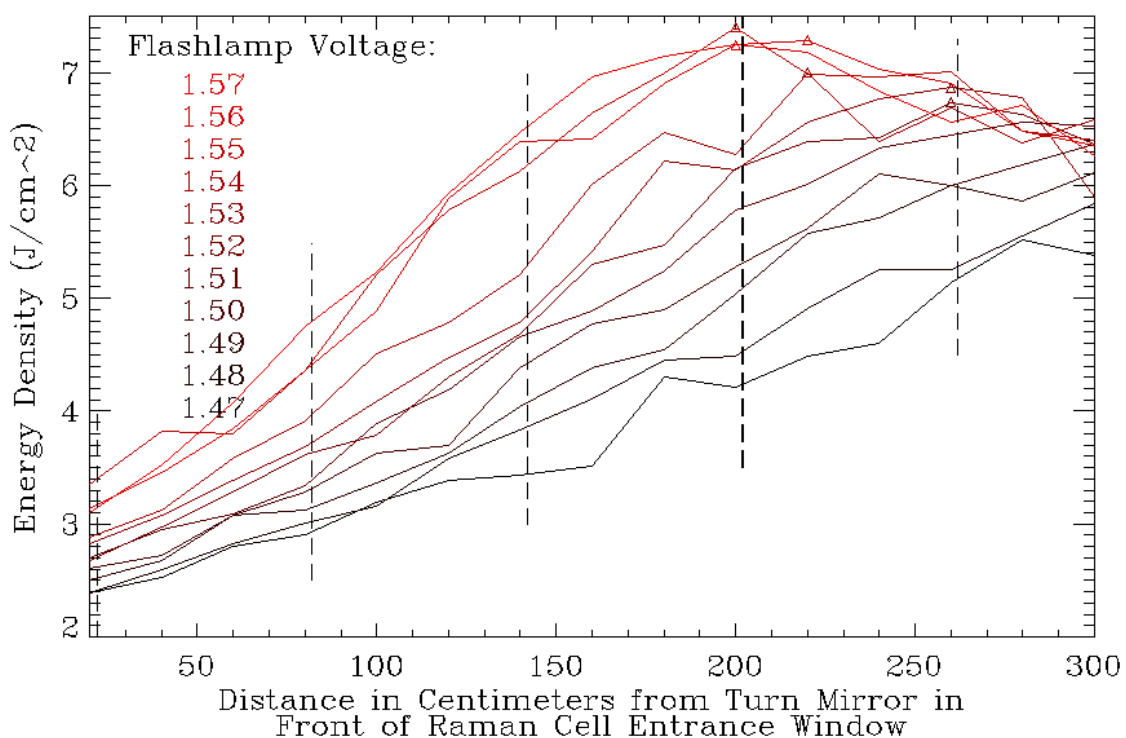


Fig. 18. (Color required.) Energy density of the Nd:YAG beam at $1 \mu\text{m}$ vs. distance from the Raman cell entry window per flashlamp voltage. The triangles represent the actual peaks of those curves. The peaks represent the highest energy density in the beam, also referred to as “the waist.” The vertical dashed lines indicate the approximate locations of the Raman cell prisms. The thicker vertical dashed line represents the approximate location of the Raman cell prism that was damaged. Notice that the curves corresponding to flashlamp voltages 1.52 to 1.57 kV have peaks within Raman cell.

A Java-based computer program, ImageJ, was used to measure the area of the beam’s centroid. The burn paper was scanned into a computer at 1200 dpi. ImageJ was used to find the area in pixels of the centroid of each pulse. The centroid was taken to be the area inside the ring that was most distinct. Because burn paper is an uncalibrated measurement media, exact energy density is approximated using the energy levels of the flashlamp voltage experiment as shown in Fig. 14.

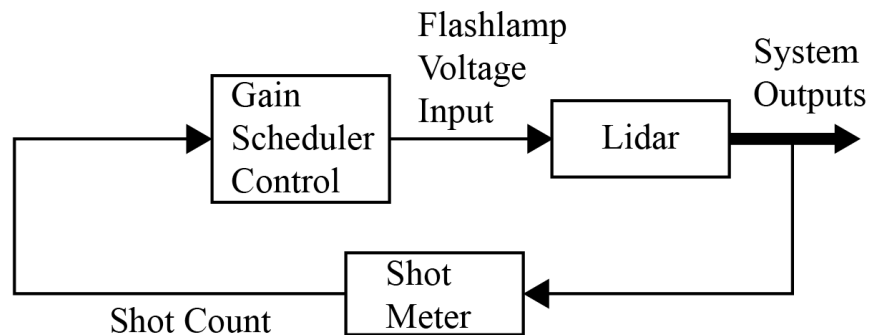
The results of the experiment are revealed in Fig. 18 with dashed vertical lines marking the approximate positions of the four prisms inside the Raman Cell. The bold line represents the prism that was damaged. Maxima in the energy density are marked with Δ . Note that the maxima for each curve represent a waist in the beam and a peak in energy density. For low voltages the waist is located beyond the exit window of the Raman cell (a distance of three meters from the entrance window) as expected. As the voltage is increased the waist moves into the Raman cell and may result in energy densities that are higher than the damage threshold of the optics. As expected, the voltages that produce a beam with a waist inside the Raman cell are voltages 1.52 to 1.57 kV as identified with the Δ .

This experiment confirmed the theory that prematurely increasing the flashlamp voltage moves the beam waist from beyond the Raman cell to inside thus increasing beam energy density above the damage threshold of the optics. The linear energy feedback control does not, therefore, have all 11 flashlamp voltage settings available at all times. The control would need to know the location of the waist which is not possible with the present configuration of the instrument.

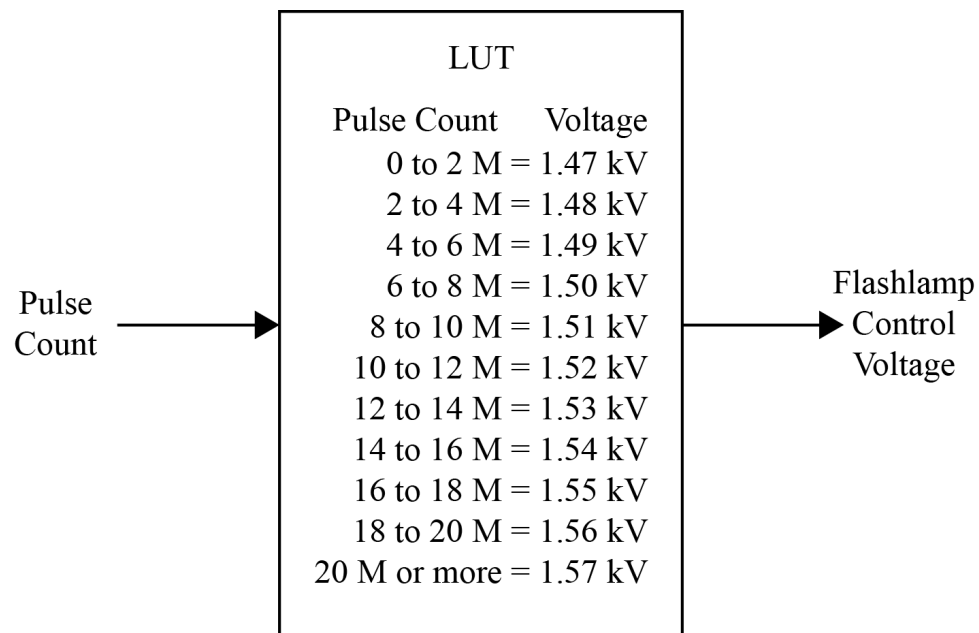
This experiment concluded that the linear energy feedback control has limited capabilities in stabilizing the transmit energy and introduces high energy density risks to the wavelength converting part of the instrument. It was decided that the gain scheduler control would be investigated as a solution that would provide more stable transmit energy.

Gain Scheduler Control

The gain scheduler method implements a look-up table (LUT) to set the flashlamp voltage based on the number of flashlamp discharges. The LUT is designed to take advantage of the full range of voltage settings, incrementing ten times in the life of the flashlamps at even intervals. The gain scheduler system



(a) Lidar control system diagram with pulse count feedback controller.



(b) Pulse count feedback controller implemented as a look-up table (LUT).

Fig. 19. Lidar control system diagram with pulse count feedback controller. The pulse count feedback controller is implemented as a look-up table (LUT). This was the control implemented for the field experiment performed in this study.

diagram and LUT are shown in Fig. 19. The beam energy may decrease or increase over the lifetime of a flashlamp set but should be more uniform and consistent. The flashlamp voltage will increase every two to three million pulses depending on the expected flashlamp lifetime of 20 or 30 million pulses, respectively.

An experiment was performed to collect new data that were compared with the data from the CHATS experiment (Fig. 12). The lidar was operated continuously and unattended from October 2 to October 22, 2012. On October 22, a rain storm interrupted the experiment but operation resumed on October 25 and continued through October 30. The flashlamp voltage was adjusted according to a 20 million pulse lifetime. The results are shown in Fig. 20.

By comparing Fig. 12 with Fig. 20, several differences can be observed. It is important to note the scale of the vertical axis on the plots. The main goal in this experiment was to stabilize the Nd:YAG energy. A scaled comparison of the Nd:YAG beam energy and the transmit beam energy is shown in Fig. 21.

In Fig. 20 it was expected that the flashlamp voltage would have a considerable effect on the beam energy and the SRS conversion efficiency and it did. However, the goal was to stabilize the transmit power so that it does not decrease over time with the aging of the flashlamps. It actually increased which means the lidar will produce even better measurements over time. Experiments will be performed in the future to investigate how transmit pulses from the early life of the flashlamps might have energy levels similar to pulses from the later life of the flashlamps. It is possible that the cause of this increase in energy is the result of a flashlamp voltage incrementation schedule calculated for a 20 million pulse lifetime. An incrementation calculated for a 30 million pulse lifetime might produce a transmit energy more constant over the flashlamp lifetime. However, this energy level would be closer to the starting energy level which is lower than the energy

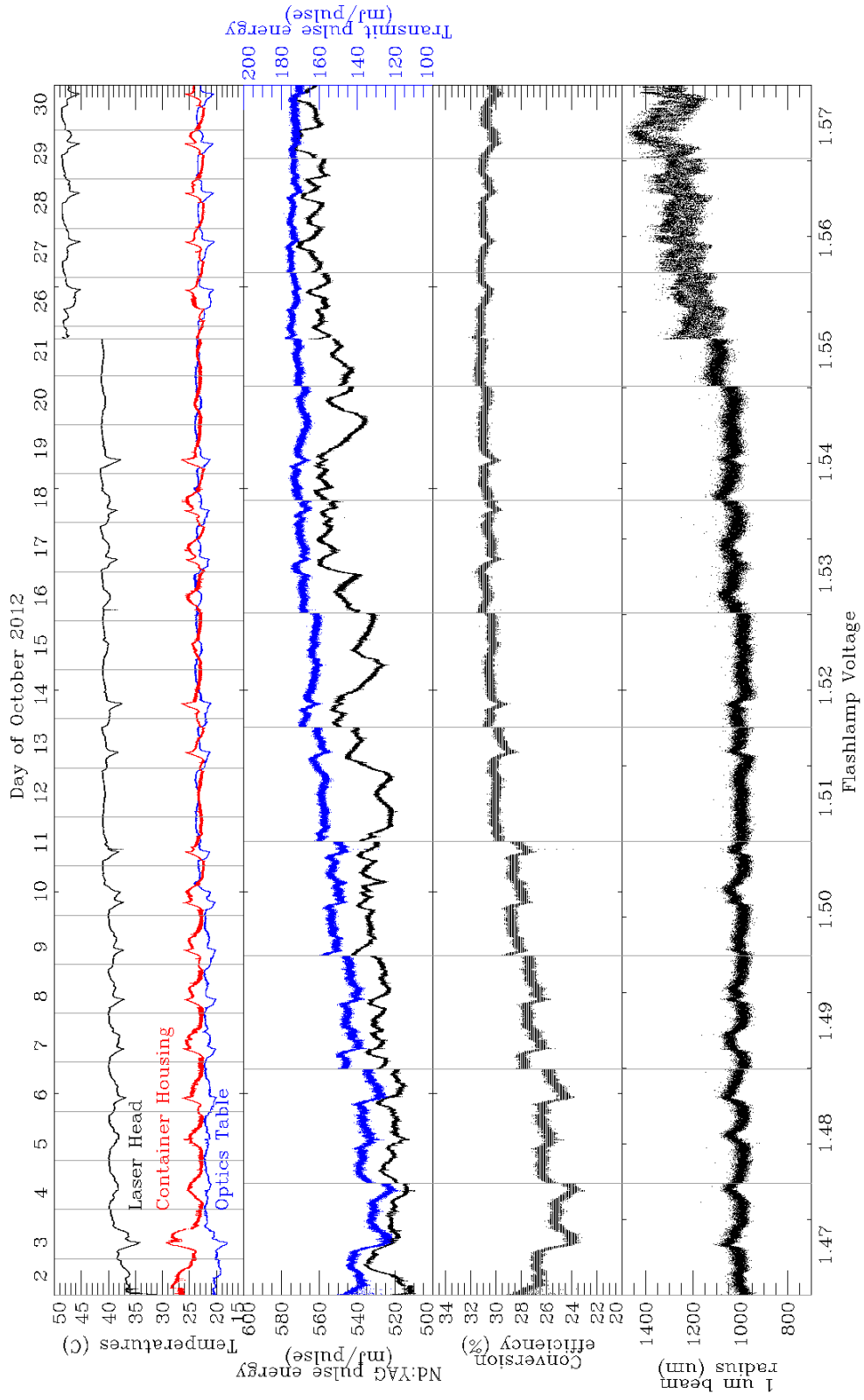


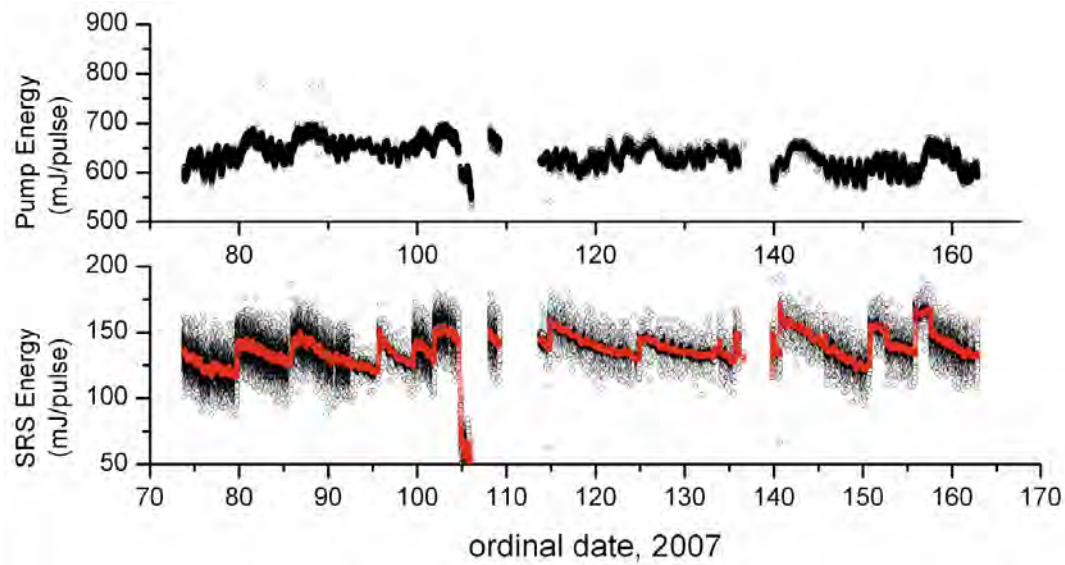
Fig. 20. (Color required.) Vital signs during the October 2012 experiment using the gain scheduling controller with pulse count feedback. A strong correlation between temperature and laser beam energy and radius is noted. Both the Nd:YAG and the transmit beam energies were noted to have an increasing trend as the flashlamp voltage increases.

levels toward the end of the experiment. This is because flashlamp voltage incrementation rate would be more proportional to the deterioration rate of the flashlamp cathodes.

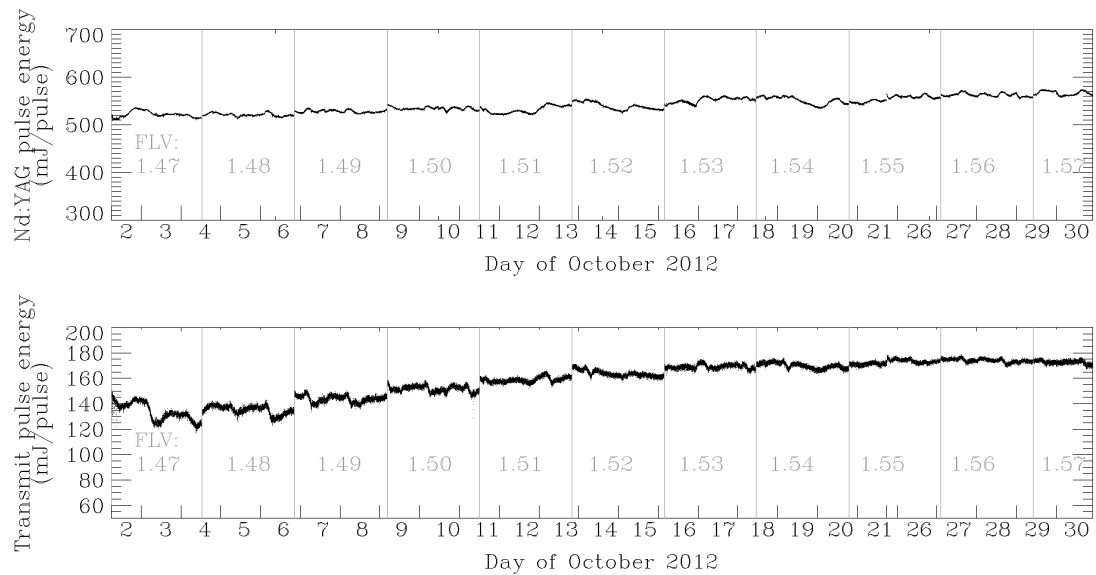
The 1.5 μm beam radius was monitored closely during the experiment. The slight increase in radius toward the end of the experiment suggests that the waist is moving farther from the exit window of the Raman cell as the flashlamps age. Because beam energy density is increasing while the radius is decreasing, energy density, and therefore conversion efficiency, remain more stable.

System temperatures are highly correlated with both beam energies, and therefore, with conversion efficiency and the beam radius. A strong dependency on temperature was not expected, but was found. It is hypothesized that the vital signs are more sensitive to temperature than expected through the effects of thermal lensing. The Nd:YAG rod used in this study is relatively long and manifests thermal lensing as the rod is heated more on the axis of the beam than on the outer regions. This temperature variation in the rod causes some transverse gradient of the refractive index of the rod. Temperature variations in the laser head accentuate this effect. Thermal lensing alters the intended convergence of the beam thus affecting the vital signs of the instrument.

This finding will lead to further experiments to study the effect of temperature and how it can be controlled to produce more stable results of the instrument. The Nd:YAG rod temperature is stabilized using circulating water. A future experiment might provide a larger reservoir of circulatory water thus increasing the thermal mass and the temperature stability of the laser head. The current reservoir is approximately one liter in size.



(a) Nd:YAG and transmit beam energies from the CHATS experiment



(b) Nd:YAG and transmit beam energies from the field experiment with flashlamp voltage control

Fig. 21. A comparison of data from the CHATS experiment (upper two plots, a) and the field experiment with flashlamp voltage control (lower two plots, b). The control designed in this study was tested on a new set of flashlamps to verify the effect on the beam energy over the lifetime of the set. This comparison verifies the ability of the control to stabilize the beam energy.

Safe-Shutdown Feature

Prior to this study, unattended operation of the original REAL required accepting the risk that a problem would go undetected and might initiate a chain reaction of costly additional component failures and data loss. To reduce this risk associated with long-term unattended operation, a safe-shutdown (or “fail-safe”) feature was added to the control system. A fail-safe feature significantly reduces the risk of catastrophic failures or data loss because out-of-range variables are immediately detected and actions automatically taken to trigger a graceful shutdown of the entire system.

The backbone of the safe-shutdown feature is a collection of thresholds that will set a flag when violated by a measurement of the appropriate system variable. Each variable in the system has at least one set of thresholds that acts as a preventative measure against failures and damage to system components by notifying personnel of system status and/or gracefully shutting down the instrument. The threshold values are derived using component specifications and data records.

The procedure for shutting down the system starts by closing a safety shutter at the entrance to the receiver box, thus preventing any radiation from reaching the InGaAs detectors, which are the most vulnerable components in the system. At the same time the safety shutter is closed, a command is sent to the Nd:YAG laser PCU to stop the flashlamps. Stopping the flashlamps prevents further damage to system components that might have been caused by the Nd:YAG laser, the most powerful component. The rest of the shutdown procedure involves contacting personnel, closing communication ports, moving the BSU into the stow posture, and cooling the laser head.

Nd:YAG PCU Key Turner and Safety Shutter

An underlying goal of this research was to enable the lidar to operate remotely using a connection from the main campus. Two obstacles that were overcome were remotely powering on the Nd:YAG laser PCU and protecting the InGaAs detectors. Dr. Eric Ayars from the Department of Physics at CSUC designed and fabricated a microcontroller that activates a servo motor. The key turner is a LabVIEW controlled servo motor and controller secured to the face of the Nd:YAG laser PCU. When activated, this servo motor turns the power key to the ON position. The key turner allows for remote control of laser power without altering the existing equipment. A photograph of the key tuner is shown in Fig. 22.

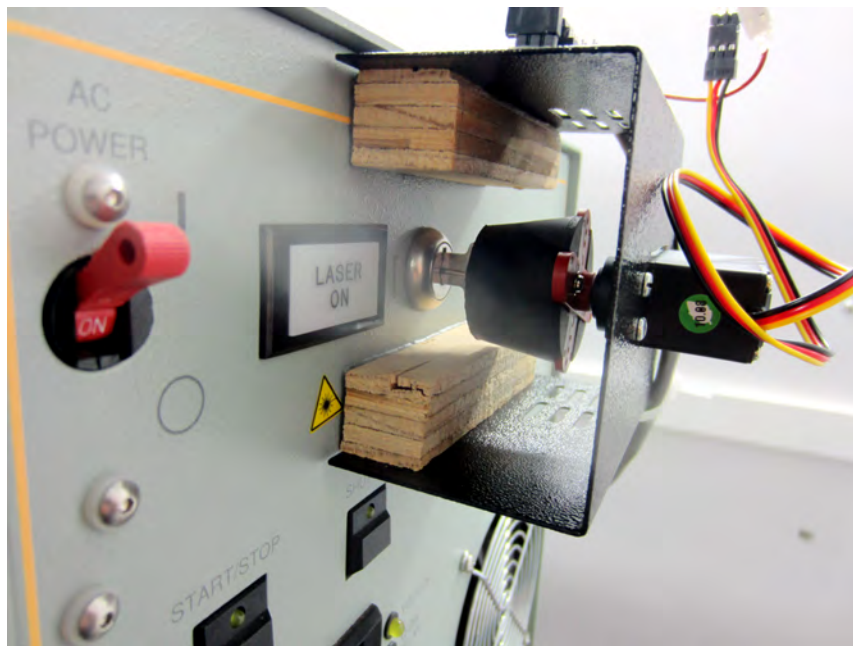


Fig. 22. Photograph of Nd:YAG laser PCU power key turner. A microcontroller with a servo motor facilitates remote operation of the lidar.

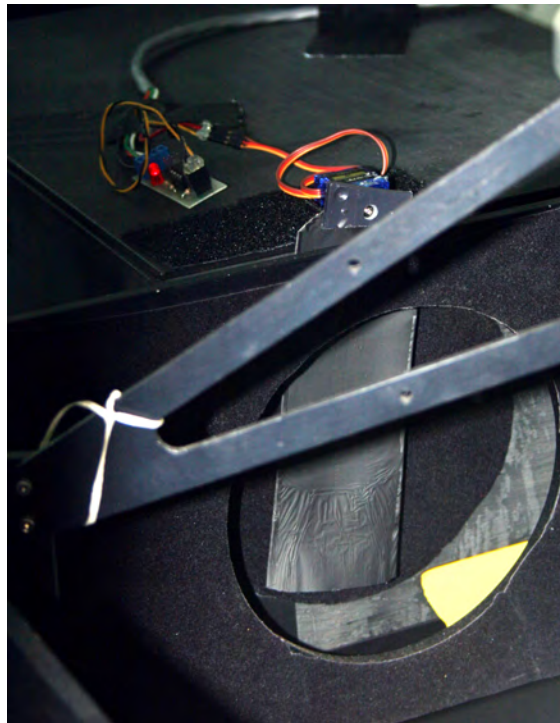


Fig. 23. Photograph of the receiver box safety shutter. A microcontroller with a servo motor facilitates remote protection of the InGaAs photo detectors.

The safety shutter is another servo with a controller and a matte black, rigid, and light-weight card attached to the head. When activated, the card swings down to block any backscatter radiation from entering the receiver box. The safety shutter is shown in Fig. 23 in the position that blocks backscatter radiation from entering the receiver box. The safety shutter provides remote-controlled protection for the most sensitive components of the system.

These devices, along with network controlled uninterruptible power supplies (UPSs) and power distribution units (PDUs), enable complete remote operation of the instrument. This is done across a wireless network connection from the lidar facility to the CSUC Farm office. Security cameras also assist by allowing operators to view various components and conditions during remote operation.

Contact Personnel Feature

It is convenient to contact personnel as soon as a system variable exceeds a preset threshold. Doing so enables engineers and operators to investigate and take corrective action if necessary. Variables that are out of normal range trigger warning or shutdown procedures that contact personnel via SMTP. Messages sent to personnel include: (1) the name of the system variable that triggered the flag, (2) the value of that variable, (3) the threshold the variable violated, and (4) the time the event occurred. Messages are sent in the form of emails or text messages to mobile phones. These text messages have been the quickest method of communication. Currently, it is programmed to send an email to two addresses or phone numbers. Personnel can respond to the messages and failures by logging on to the system PC remotely through the network or traveling to the instrument to adjust system components, perform maintenance, perform necessary repairs, or simply restart the system.

There is one known risk in this design: messages are dependent on a two-kilometer wireless signal from the lidar facility to the CSUC Farm office and another from the Farm office to the main campus before accessing the Internet. If a network failure occurred during unattended operation and personnel was not made aware, the instrument would still be shut down gracefully. The system could potentially be inactive for hours or days before personnel became aware of the change, resulting in loss of time and data. This can be prevented by operators simply checking a web application that posts the most recent system variable measurements. If the data on the web application is not current and a message has not been received, a system failure has occurred, the instrument has safely shut down, and the network was not able to deliver the message to the operator.

Frequency of Control

A vital piece of the control design is the frequency at which it performs. The Nd:YAG laser, pulsing at a frequency of 10 Hz, is not controlled by the main program. The command to start lasing is issued by the main program and the laser begins pulsing at 10 Hz independent of the control loop. Much of the preliminary work on the control design was deciding whether to control at a faster rate, a slower rate, or the same rate as the firing of the laser. After some research it was apparent that a control loop that executed at any rate other than the 10 Hz of the laser would unnecessarily introduce significantly more complexity to the system.

A slower control loop would likely occur once per scan of the atmosphere and the control frequency would, therefore, depend on the duration of a scan. When a scan is complete, the BSU returns quickly to the azimuth and elevation angles that were specified for the beginning of the scan. During this time, sometimes referred to as the “fly-back”, the transmitter will continue to pulse, but backscatter data will not be recorded. The time the fly-back takes to occur is usually between 400 to 800 ms depending on the angular width of scan. The 100 ms period of the Nd:YAG laser loop might constrain calculations that would be possible during the fly-back time. If the control loop is executed faster than once per scan it will happen inbetween laser pulses that need to be recorded. This limits the control to what can be executed within the 100 ms period. If the control is designed to execute more frequently than once per scan it might as well execute every time the Nd:YAG laser pulses.

A control frequency of once per scan would be less computationally demanding, but the control would not be fast enough to catch all failure cases in an appropriate amount of time. For example, if the energy density in the Raman cell

exceeds damage thresholds, an immediate shutdown should occur. Data analysis indicated that the 10 Hz control loop detected the drop in energy associated with the damaged prism and shut down the system within 500 ms or 5 laser pulses. If the control executed once per scan and the scan at the moment of energy density increase was a wide, slow horizontal scan, it is possible that the scan could last up to a minute. This is enough time to allow hot spots in the beam to begin damaging other components.

In researching methods of timing control, National Instruments support network was contacted. One of their suggestions included a master/slave architecture. A master/slave architecture configures the 10 Hz Nd:YAG laser pulse loop as the master loop that would execute the control loop, acting as the slave, as often as possible. The slave loop executes independently of the master loop at a rate that could be slower than 10 Hz, but it is as fast as the system PC will allow. Because the slave loop executes independently, the master loop will record the backscatter data for each pulse to prevent data loss. This would be an excellent solution if the control could not execute within the 100 ms period of the master loop. However, because the control can execute within the 100 ms period it was decided to execute the control at least once per pulse to take advantage of some additional capabilities of this method.

If the control loop executes at least once in the 100 ms period between Nd:YAG laser pulses, one set of measurements could be collected from the system variables for each laser pulse. This has proven essential for diagnosing a failure in post-operation data analysis. In the case of the energy density increase in the Raman cell that resulted in damage to a prism, data from the last three pulses were used to identify the possible causes of the failure.

TABLE 2
SYSTEM VARIABLE MEASUREMENTS DISTINGUISHED BY
DEPENDENCY ON ND:YAG LASER PULSE

System variable measurements dependent on a Nd:YAG laser pulse	System variable measurements independent of Nd:YAG laser
★Nd:YAG laser beam energy	Housing temperature
★Transmit beam energy	Optic table temperature
★Raman cell conversion efficiency	Raman cell temperature
★Transmit beam radius	Nd:YAG laser cavity temperature
Transmit beam centroid X location	Raman cell pressure
Transmit beam centroid Y location	Precipitation sensor
Flashlamp count	Absolute attitude of platform
Flashlamp control voltage	Utility power
InGaAs Detector Control Voltage	BSU pointing direction
	BSU movement
	Disk space availability

The system variable measurements that are dependent on the Nd:YAG laser pulse cannot be used in a control frequency faster than the pulse rate of the laser. Relatively few variables are left if such a controller is implemented. Vital signs are marked with a ★.

A faster control loop would significantly complicate the main program code of the system. This type of design was considered until the role of the system variables was investigated. Table 2 lists the system variable measurements that are dependent on and independent of the Nd:YAG laser pulse with the vital signs marked with a ★.

This analysis revealed that all vital sign measurements require the discharge of the Nd:YAG laser. Then the question became “Is a frequency of 10 Hz adequate to control all variables?” Each system variable has a different rate of change. Temperature in the housing container, for example, will not change faster than about three degrees Celsius per minute. Beam energy, however, could drop dramatically from one pulse to the next if, for example, an optic is damaged.

Analysis revealed that no system variable could be controlled fast enough to prevent a failure from developing between the 10 Hz pulses.

Along with the rate at which system variables change, the rate at which sensors can be sampled and the signal-to-noise ratio of each sensor were considered in the design. Each system variable has a control option that will calculate running average samples. This allows noisy measurements to be smoothed out to a more representative value. The Molectron energy detectors, for example, are relatively noisy. A measurement may range between 140 and 170 mJ. A running average of ten samples would produce a smoother measurement that can be used to control more precisely. However, with an average of ten samples, failure detection is slowed. The system can collect ten samples in one second while the beam energy can change substantially within that period. It was decided that a running average of three samples would provide sufficiently smooth values and would maintain the desired control speed.

The beam radius sensor produces noisy measurements that range from 8 to 12 mm. This sensor is also slow with a sampling frequency of 2 to 10 Hz (measurements are held for 1 to 4 pulses until a new measurement is taken). Due to the noise and sampling frequency of the sensor, a running average of 20 samples or more is used to smooth the beam radius value. The sensors measuring tip and tilt of the housing container, on the other hand, have little noise and are capable of fast sampling frequencies. These sensors do not require a running average.

As the main program was expanded to include various control features, the interpulse period of 100 ms became a concern. The time spent processing each cycle of the main loop was measured as the time period from the moment the program received the loop trigger from the Nd:YAG laser, to the time the program had completed all instructions and was waiting again for the next trigger. This

TABLE 3
LOOP PROCESS TIME FOR DISTINCT IMPLEMENTATION PHASES

Design phase	Min(ms)	Avg(ms)	Max(ms)
Original	60	70	80
Control added	80	95	100
Code parallelizing	70	80	90
SNR calculation and black box added	90	110	120
Subroutine optimization	80	90	100

Time required to complete all tasks in the control system.

measurement was recorded through most of the design and implementation process. Table 3 reveals that the process time of the various phases of design was close to or even exceeded the allotted period.

There are two explanations for the success of the operation despite the apparent violation of the allotted time period. The first is that methods for measuring the timing with the functions available in LabVIEW are limited. These measurements do not reflect any parallel processing, system priority settings, or display processing. Although the measurement is more relative than absolute, the effect the changes had on the process time was apparent. The second explanation is that there are multiple buffers in the system. The detectors, digitizer, processors, and graphic displays all have buffers that store data while the system is busy with calculations. This allows some flexibility in the execution priority and calculation timing.

Other options were considered in an effort to speed up processing to make execution time available for additional features. The limitation in control frequency begins with the speed of the computer currently executing the main program, a Dell Precision T7500 running a Windows 7 operating system on a Intel(R) Xeon(R) E5620 with 3 GB of RAM. The nature of a commercialized operating system such as Windows 7 is that it specializes in prioritizing a variety of

tasks and programs that may be running at one time. When the lidar control program is running on such a machine it is possible to prioritize execution in favor of LabVIEW, but such control is very limited and not very effective. The solution would be to implement an operating system that executes only this program.

National Instruments offers a Real-Time Module that would provide the desired solution. The NI Real-Time Module would effectively transform the computer executing the main LabVIEW program into a machine with a real-time operating system (RTOS). The RTOS would then be run on another machine. This setup allows the RTOS to do one thing: control the lidar.

A RTOS would provide the control necessary to push the hardware to meet the timing requirements of the 10 Hz loop. The NI Real-Time Module implementation could cost up to \$3,000, depending on hardware implemented, and would require a significant amount of time to design, configure, install, and implement. For this reason, this research focused on optimizing the processing time required for each loop (with the current hardware).

It is possible that future high pulse-energy atmospheric lidars could use lasers with faster pulse rates than are used in this study, such as 20 Hz, 50 Hz, or 100 Hz. The current system with its software and hardware would not be able keep up with the faster-rate lasers. However, the introduction of RTOS would solve that problem.

LabVIEW is a very serial language. Some effort was spent optimizing the code to be more parallel in nature. This significantly improved the speed of the loop but also made the code more challenging to read. It was determined that the improvement in speed was worth the increase in code complexity.

A timing profiler is available for LabVIEW programs. This profiler reports the time and memory each routine and subroutine utilize in execution. This

was helpful in identifying subroutines that could have the greatest impact if optimized. The profiler report identified the black box feature as a memory intensive routine and was hard coded to optimize usage. The email feature was identified as a time consuming routine and was optimized as a subroutine to minimize execution time. It was concluded, however, that for a thorough analysis and optimal design, a NI Real-Time Module would need to be purchased, and a RTOS would need to be implemented.

Data Quality

Data acquisition is at the heart of this study. Backscatter data is captured and used in other algorithms to deduce wind and boundary layer height. System variable measurements are recorded that represent system conditions. These two sets of data encompass most of what is known about the system when in operation. A number of steps were implemented to improve backscatter data quality.

Optimizing Digitizer Resolution

The InGaAs detectors produce a waveform that represents the backscattered signal intensity from the atmosphere. This voltage has an amplitude of up to 1 volt. A 100 MS/s, 14-bit NI PCI-5122 digitizer reads the backscatter signal into the computer. The 14-bit range provides 16,384 counts of digitization. Digitizer resolution can be set by adjusting voltage input range and offset to be captured by the 16,384 counts. The available settings are shown in Table 4 [71].

Adjusting resolution settings optimizes the digitized signal on the data type used. A wide voltage input range offers a coarse resolution that would best capture the larger dynamic range of data on days when the atmosphere contains regions of very strong backscatter signal (such as clouds, smoke plumes or layers).

TABLE 4
 FULL-SCALE PROGRAMMABLE INPUT RANGE
 AND VERTICAL OFFSET FOR THE NI PCI-5122

Range (V_{pk-pk})	Vertical offset Range (V)	Resolution ($\mu\text{V}/\text{count}$)
0.2	± 0.1	12
0.4	± 0.2	24
1	± 0.5	61
2	± 1	122
4	± 2	244
10	—	610

The signal read from the InGaAs sensors usually ranges from +0.4 volts to -0.6 volts. This restricts the range setting to 0.4 volts or greater, given that a range of 0.2 volts with a maximum offset of 0.1 volts will not read the +0.4 volt signal.

Such waveforms are digitized and plotted in red and green in Fig. 24. A narrow voltage input range offers fine resolution that would best resolve waveforms on days when the atmosphere is clear. The blue curve in Fig. 24 offers a sample waveform from a clear day.

The voltage range of the digitizer is set to ten volts by default. This is wide enough to capture the entire waveform from the InGaAs detectors that is never more than one volt in amplitude. The lighter horizontal lines in Fig. 24 mark the two narrowest voltage ranges on the digitizer. The narrowest is a range of 0.2 volts. This range is wide enough to capture more than 97% of the waveform at 50 times the resolution the default setting would provide. Unfortunately, the 0.2 volt range does not accommodate the waveform read from the detectors as most of the data is represented by voltages greater the 0.3 volts and the greatest voltage read by the digitizer with a 0.2 volt range is 0.2 volts, including the 0.1 volt offset. The next narrow voltage range is 0.4 volts which captures more than 87% of the

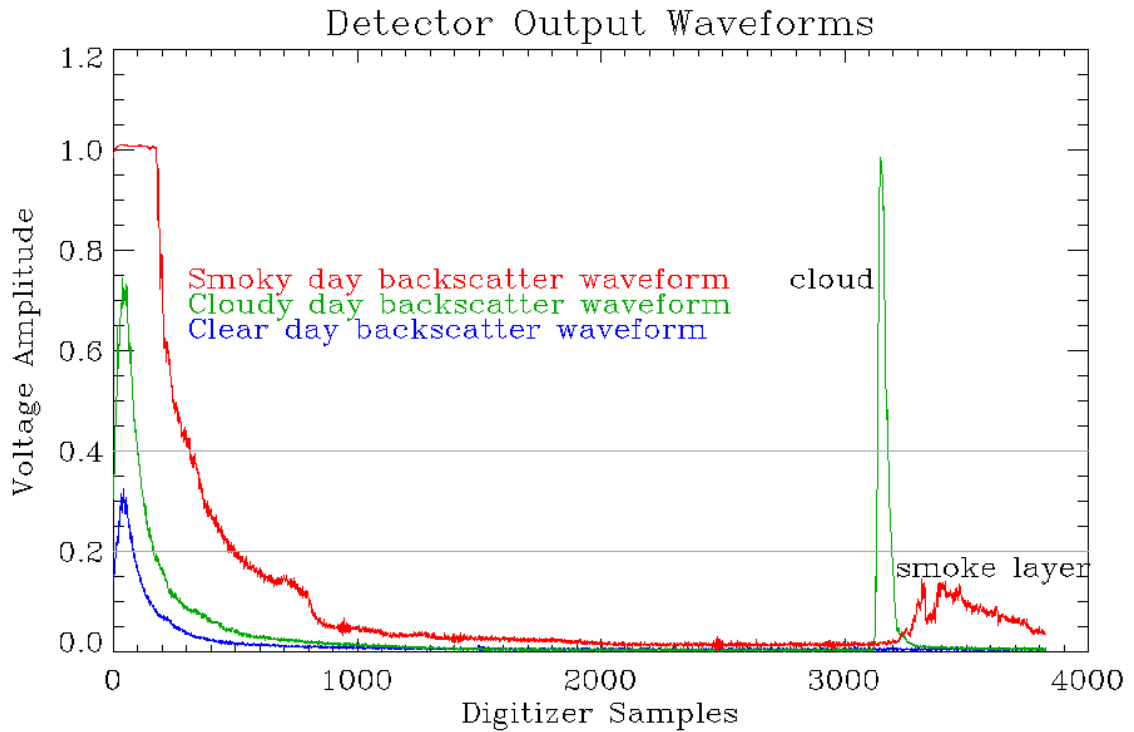


Fig. 24. (Color required.) Backscatter intensity waveforms from InGaAs detectors on days with clear sky, clouds, and a smoke layer. A day with clouds will produce about a one volt range from the InGaAs sensors. Days with clear sky and possibly a smoke layer could take advantage of a high resolution setting on the detectors as shown in Table 4.

waveform with a cloud layer at 25 times the resolution the default setting would provide.

A computer control has been implemented to change the resolution during operation without interruption. Ideally the voltage range would never need to be more than 1 volt and could adjust between ranges of 1 and 0.4 volts automatically as atmospheric conditions change. This feature will be considered for future projects.

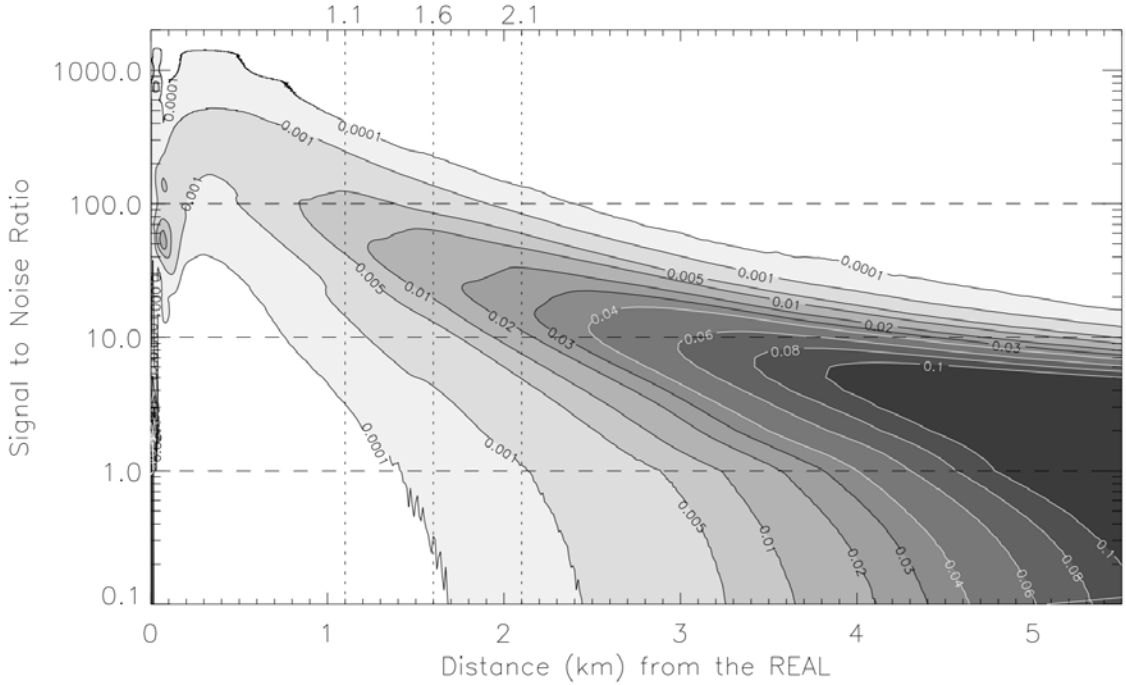


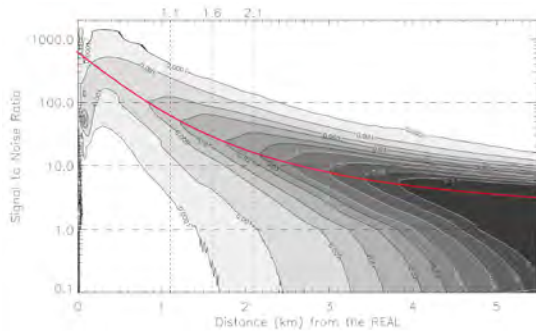
Fig. 25. Frequency distribution of single pulse SNR of the aerosol backscatter data as a function of range during the CHATS experiment [12].

An experiment was performed to study the effects of digitizer resolution on the signal-to-noise ratio (SNR). In this study the SNR is calculated as

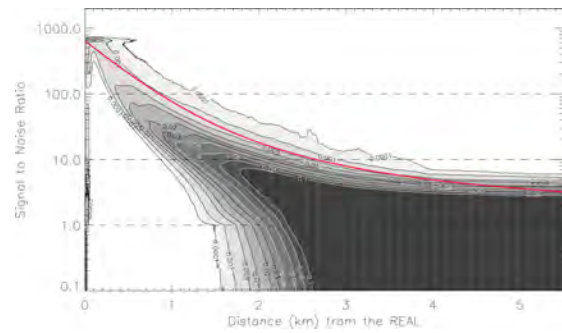
$$SNR(r) = \frac{S(r) - S_b}{\sigma_b} \quad (2)$$

where $S(r)$ is the data point in question, S_b is the mean of the 375 digitizer samples recorded during the $3.75 \mu\text{s}$ before the Nd:YAG laser pulses, and σ_b is the standard deviation of those same 375 samples. Analysis of the data recorded during the CHATS experiment revealed the SNR plot in Fig. 25 [12].

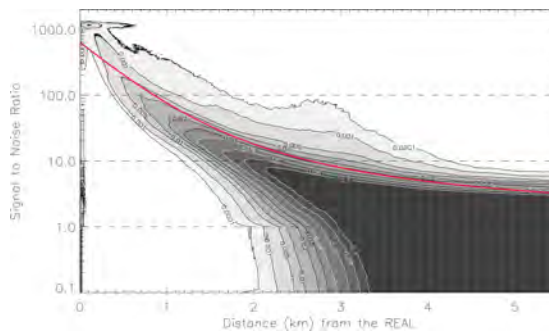
Similar graphs, shown as Fig. 26, were made by applying the same method used for the CHATS data to the data from the control system field experiment from October 2 to 30, 2012. Each panel represents a different digitizer resolution setting as indicated in the caption. The red line is the peak SNR



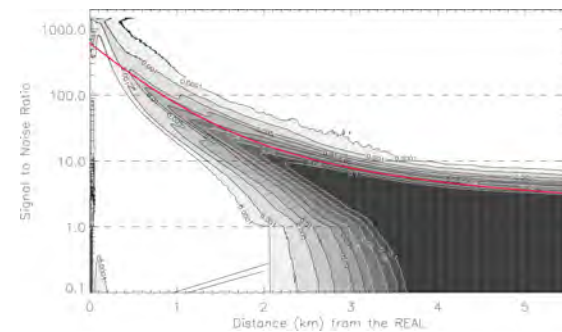
(a) Digitizer range of 10 volts. Duration of 80 days in the CHATS experiment of 2007.



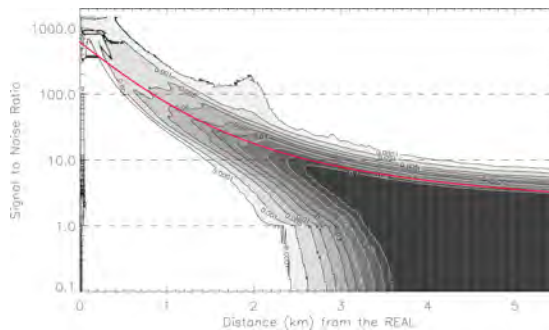
(b) Digitizer range of 10 volts. Duration of 7 days (Oct. 2–9, 2012).



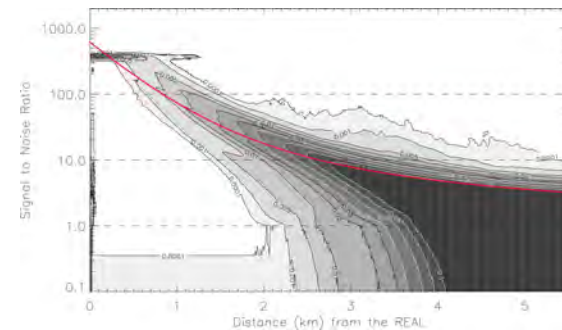
(c) Digitizer range of 4 volts. Duration of 3 days (Oct. 9–12, 2012).



(d) Digitizer range of 2 volts. Duration of 3 days (Oct. 12–15, 2012).



(e) Digitizer range of 1 volt. Duration of 3 days (Oct. 15–18, 2012).



(f) Digitizer range of 0.4 volts. Duration of 3 days (Oct. 18–21, 2012).

Fig. 26. (Color required.) Frequency distribution of single pulse SNR of the aerosol backscatter data as a function of range during the flashlamp voltage control field experiment.

distribution for the data from the CHATS experiment for comparison against SNR from the control system field experiment.

The SNR is affected by instrument performance and aerosol properties which vary with the day to day weather. Instrument performance includes both the transmit energy as well as the digitizer resolution. During the period of operation from the control system field experiment from which these data are taken, the transmit energy was relatively constant, as shown in Fig. 21. Also, aerosol properties for the operating period were similar from day to day. Although Fig. 26 shows changes in SNR due mainly to adjustments in the digitizer resolution, a future test will include a low elevation-angle stare without scanning for about ten minutes for each digitizer resolution setting. This will ensure a more constant atmosphere and transmit energy to produce SNR results that will manifest the effect of the digitizer resolution setting as much as possible.

Taking instrument performance and atmospheric condition assumptions into consideration, a significant improvement in SNR is noted during the control system field experiment. Fig. 26 suggests that the instrument started out with a lower SNR in the control system field experiment than in the CHATS experiment. With adjustments to the digitizer the SNR was improved to above that of the CHATS experiment. Fig. 27 reveals the improvement in SNR during the control system field experiment alone. The yellow line indicates the peak SNR distribution for the default 10 volt range setting on the digitizer. The blue line indicates the peak SNR distribution for the 0.4 volt range setting.

The maximum resolution setting during the control system field experiment produced an SNR distribution peak of 200 at a range of 1 km. This is double the SNR distribution peak at a range of 1 km from the CHATS experiment. The control system field experiment revealed a greater improvement in SNR from the lowest resolution setting to the highest. The SNR distribution peak of 200 at a range of 1 km is one order in magnitude greater than that of the SNR distribution

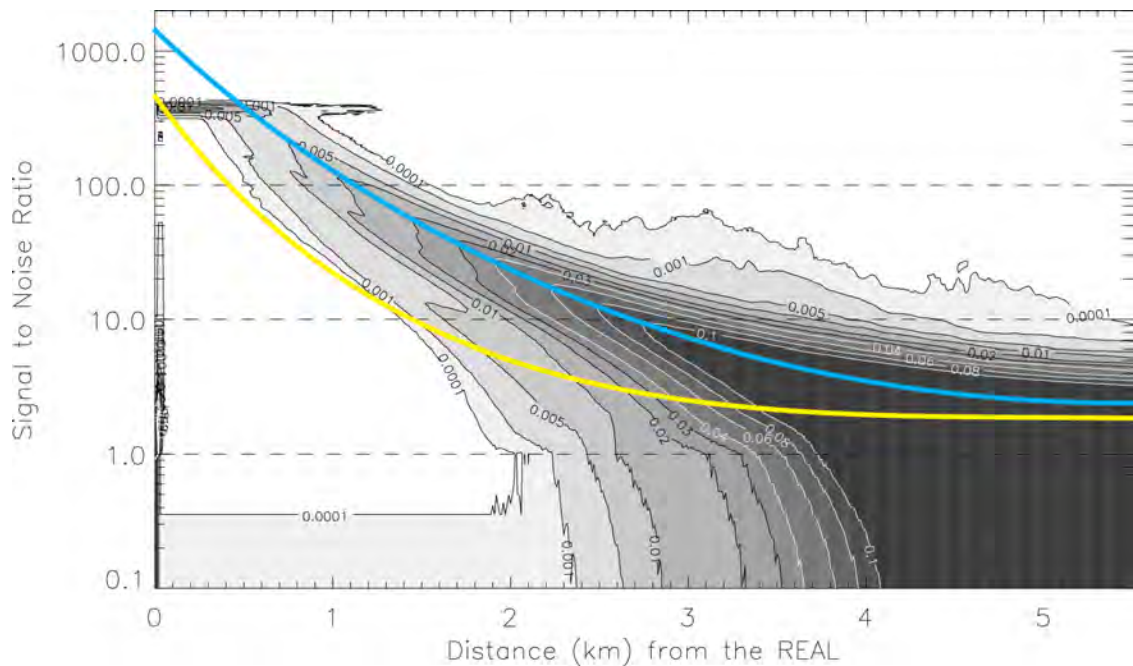


Fig. 27. (Color required.) Comparison of SNR peak distribution of the aerosol backscatter data as a function of range during the control system field experiment. The yellow line indicates the peak SNR distribution for the default 10 volt range setting on the digitizer and the blue line for the 0.4 volt range setting. Overall improvement at 1 km range during the experiment was an SNR of about 20 to an SNR of about 200.

peak of 20 at a range of 1 km for the lowest resolution setting in the same experiment. The digitizer setting resolution has a significant impact on the performance of the system.

A study was performed prior to this work to analyze how SNR is related to the spatial wind field measurements of the lidar [12]. Fig. 28 shows the distributions of velocity component differences in lidar measurements and sonic anemometer measurements as a function of average SNR for the CHATS experiment. As SNR increases, the distribution in measurement difference narrows. This shows that the wind measurement benefits from efforts to improve the SNR of the backscatter data.

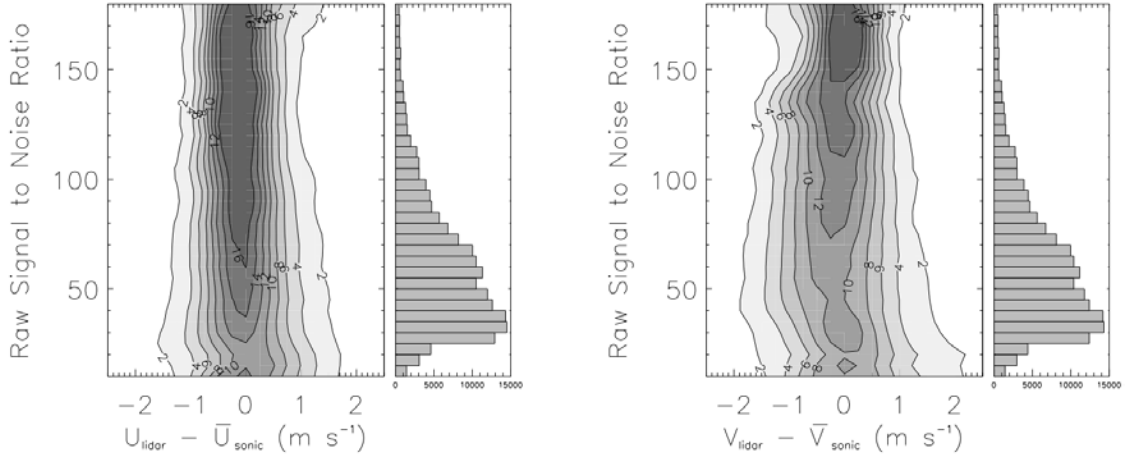


Fig. 28. Distributions of wind velocity component differences as a function of average SNR in the cross-correlation blocks used to derive the lidar vectors. Contour interval labels are in percent. The bar chart to the right of each contour plot shows the number of data points in each SNR bin interval. The width of the distribution of velocity component differences tends to decrease as the SNR increases [12].

Data Normalization

Prior to this research the backscatter waveforms captured by the digitizer appeared to have a random vertical offset from one pulse to the next. This produced radial striations visible in scan images. The leading hypothesis theorized it was the result of transmit energy variation from pulse to pulse. However, when the voltage produced from the InGaAs detector was observed directly, the vertical offset was not present. The background signal, calculated from pre-trigger samples recorded before the pulse of the laser was sensed, maintained a constant level. The erratic vertical offsets were a result of a previous unsuccessful effort to normalize the backscatter data.

Therefore, the normalization process was completely redesigned to normalize the signal by offsetting the average background (pre-trigger) level of each channel to a constant. This process does not change the amplitude of the

waveforms but shifts them to have equal average background levels. The erratic vertical offsets were minimized and the radial striations were significantly reduced. Fig. 29 highlights the differences between the unnormalized (Fig. 29a) and the normalized (Fig. 29b) data. Fig. 30a and Fig. 30b magnify the striations to more clearly show the differences.

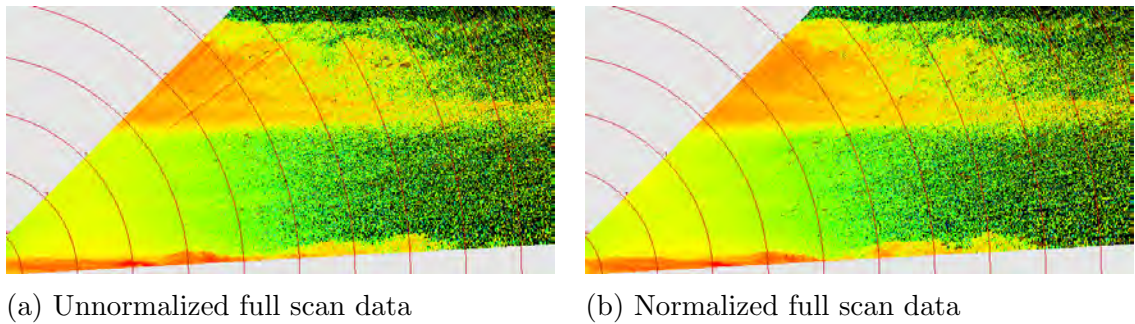


Fig. 29. (Color required.) Comparison of unnormalized (left) and normalized (right) full scan data. These images are examples of vertical scans that can reveal the atmospheric boundary layer at lower altitudes and clouds aloft.

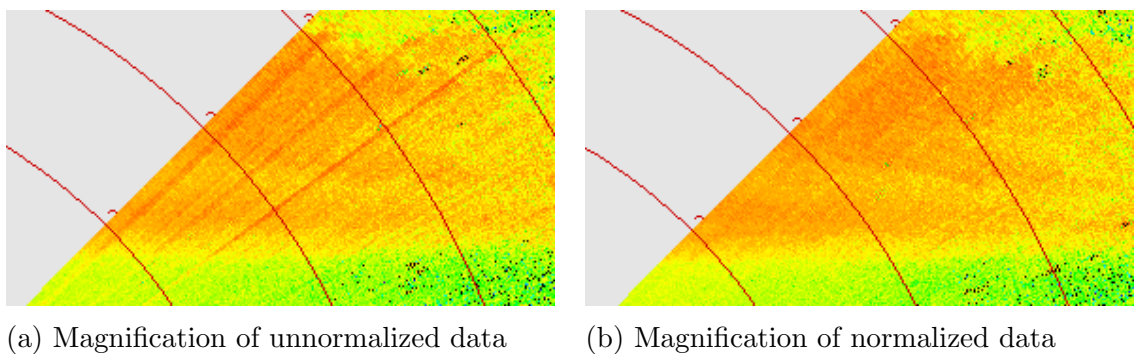


Fig. 30. (Color required.) Magnified comparison of unnormalized and normalized full scan data.

Darker red radial stripes shown in Fig. 30a are, at times, more or less apparent. This case is considered typical. The normalization was applied to each pulse from one scan to the next and, therefore, these two scans are separated in time by about 20 seconds.

BSCAN File Header

Atmospheric backscatter signal is detected, digitized, and written to disk in the BSCAN file format. These files are written in the form of a two-dimensional array as shown in Fig. 31. Each row represents the result of a single pulse into the atmosphere. The first 30 words of a row make up the header for each record in a BSCAN file. A description of the header is given in Table 5. Following the 30-word header are the two waveforms: the first channel of the digitizer followed by the the second. There is one channel for each component of polarization in the received backscatter signal.

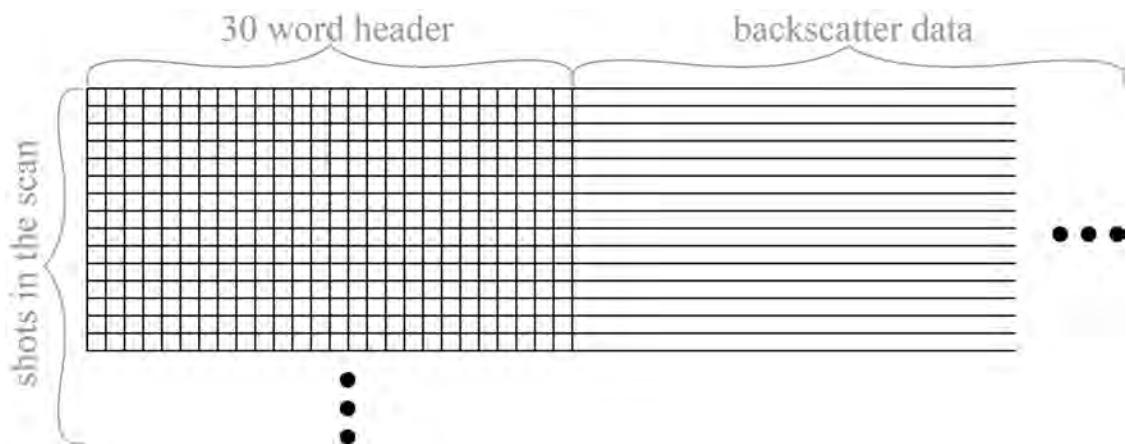


Fig. 31. BSCAN file format organization. Rows represent laser pulses. The first 30 columns represent the header and the other columns hold the backscatter data.

TABLE 5
BSCAN DATA FILE 30-WORD HEADER FORMAT

Number	Header Word Name	Units
1	Hour	
2	Minute	
3	Second	
4	GPS Altitude	Meters
5	Platform Roll	Degrees
6	Platform Pitch	Degrees
7	BSU Azimuth from North	Degrees
8	BSU Elevation Above Horizon	Degrees
9	Beam Centroid X Location	Pixels
10	Beam Centroid Y Location	Pixels
11	Beam Radius	Millimeters
12	Month	
13	Day	
14	Year	
15	Laser Pulse Repetition Frequency	Hertz
16	Transect Number	
17	REAL Identifier 220	
18	(not used)	
19	Latitude	Degrees
20	Longitude	Degrees
21	Range of First Data Point	Meters
22	Range Bin Size	
23	(not used)	
24	Number of Header Words	
25	(not used)	
26	(not used)	
27	Channel A Normalization Energy	
28	Channel B Normalization Energy	
29	Number of Lidar Profile Data Points	
30	Scan Number	

This table lists the variables stored in each of the 30 words of the BSCAN data file header. The file contains one header per record and one record per laser pulse.

The 30 words contained in the BSCAN header are available for recording system data other than backscatter. There were nine words available in the header

that were not used at the time of this study. The header was modified to include beam centroid location on the X and Y axes, the beam radius, and the absolute attitude of the platform on the pitch (longitudinal) and the roll (transverse) axes. The centroid location and beam radius are critical indicators of the beam quality and it was decided that a per pulse record would be very useful for post operation data analysis. Absolute attitude angles were included for use in future work to precisely determine the position of the beam as a function of range. This is discussed in more detail in Chapter V.

One Scan per BSCAN File

Prior to this study the BSCAN files were about 1.5 gigabytes in size and contained many scans. The large size of these files made network transfer problematic. Therefore, the BSCAN files were limited to contain only one scan per file. The size of the files now is directly related to the duration of the scan and typically ranges from 3 to 8 MB.

One sweep per BSCAN file creates files of manageable sizes that are easily organized, transferred, and processed in near-real-time. Each BSCAN file name includes the date and time of the beginning of the sweep. Data directories are now easily navigated when looking for a specific time interval or scan. The smaller size of the files also aids in the transfer of data to the server on the main campus via secure file transfer program (SFTP). Once on the server, the data are immediately available to web applications and further processing without affecting the instrument. This facilitates additional near-real-time processing of the data.

System Variable Measurements File

System variable measurements were recorded once per minute prior to this study. In the new system design these files are recorded once per BSU sweep to correspond with the BSCAN files. The system variable measurements file naming

convention also contains the same date and time as the BSCAN files. This provides a record with an average measurement of each system variable that corresponds to each BSCAN file. These files are also transferred to the main campus server via SFTP and are used in analyzing performance and diagnosing failure symptoms.

Black Box

After a system failure, engineers need to know as much as possible about the system conditions that lead to the failure. The system variable measurements are recorded once per scan (normally about once every 15 to 20 seconds). However, in the case of a system failure that developed quickly, a low-rate record with data samples a few times a minute may be inadequate for diagnosing the cause. Therefore, a “black box” was designed that records system variable measurements for each laser pulse for the last operator-specified number of minutes of operation. Now that this black box is installed, high-rate data is available for detailed analysis to determine the reason for the shutdown.

During the October 2012 testing, BSU failures occurred during horizontal scans in which the BSU motors momentarily lost power and stopped responding. In the process of debugging the failure, which occurred about once every 24 hours and usually at the beginning of a horizontal scan, the azimuth and elevation angles of the BSU were added to the list of black box variables recorded. This provided an exact record of when and where the BSU lost power and stopped scanning.

Testing and Results

The majority of the control system implementation took place between March and October of 2012. As soon as a subsection of code was designed and tested, it was implemented into the instrument. The control system was built in this way: piece by piece. Each control subsection was tested thoroughly with

simulation data by an integration test procedure. The LabVIEW coding environment provides excellent code reusability features as well as subprogram isolation that made for efficient testing.

Improvements in data quality and control were made from the beginning of the study. On July 20th at 10:35 a.m., a system failure resulted in one of the prisms in the Raman cell being damaged. The fail-safe control subsection that had been implemented prior to that point recognized the problem and executed a safe shutdown procedure. The response time was less than 500 ms and damage was contained to one prism. Repairs were made to the Raman cell and the system was operational again on the evening of August 16th. Had the control system not been in place the damage might have extended to the other prisms or windows of the Raman cell before personnel noticed. If one of the two windows had been damaged, a leak of compressed gas from the Raman cell may have resulted.

Although the July 20th case was the most extreme case of system failure caught by the control system, there have been a number of smaller incidences in which changing variables were identified and adjustments were made. These smaller incidences include changes in temperature due to changes in outdoor weather conditions, changes in pressure due to a very slow, known leak in a Raman cell, changes in the utility power due to an area-wide power outage, and changes in beam quality due to the age of the flashlamps.

A whole system test was conducted to exercise the entire design. The experiment began on October 2, 2012. The purpose of this experiment was to operate the lidar unattended for the life of a set of flashlamps. The anticipated flashlamp life was set at 20 million pulses. If the instrument operated continuously, the experiment would last 23.7 days. The system took approximately 40 minutes to set up and start. Another hour was spent monitoring the system to ensure proper

variable thresholds and operating conditions. After this start-up procedure, personnel did not assist or monitor the instrument for the duration of the experiment (25 days of operation excluding a three day interruption from a rain storm).

CHAPTER V

SUMMARY

This study demonstrated that the high pulse-energy atmospheric lidar at CSUC, with the control system presented in this work, can operate in a fail-safe manner with automatic flashlamp voltage adjustment. Potential research and commercial lidar applications, in which long-term spatial wind field and atmospheric boundary layer height measurements are required, motivated this study.

During design and testing to explore which of the proposed control solutions were viable, some proved to be effective while others were discarded or modified on an on-going basis. The resulting control system enabled the instrument to be improved in the following ways: (1) control of the flashlamp voltage to increase stability of transmit energy during operation, (2) a fail-safe feature to detect emerging problems and prevent them from escalating and damaging other system components, (3) a communication feature that notifies personnel of significant changes in the status of operation, and (4) several data quality improvements that produce more uniform, organized, and optimized backscatter energy data. With this newly redesigned control system, the original REAL is now better-suited for long-term and unattended spatial wind field and atmospheric boundary layer height measurements.

After implementation and testing of the new control system, an experiment was performed that demonstrated unattended and continuous operation

for the lifetime of one set of flashlamps (about 23 days). Performance was compared to data from an experiment in 2007 during which the instrument was operated for 80 days (3 sets of flashlamps) without the fail-safe or flashlamp voltage adjustment features. The comparison revealed improvements in the trend and stability of transmit energy. A redesign of the data normalization process, digitizer resolution settings, and data file organization improved data quality.

The control system presented in this work facilitates improved spatial wind field and atmospheric boundary layer height measurements over long periods of continuous and unattended operation. This new capability of the lidar opens opportunities for deployment in meteorological research and commercial applications. These opportunities include: wind resource assessment that requires long-term monitoring to determine wind energy potential in challenging-to-reach locations and altitudes, wind turbine efficiency improvements that use incoming wind vector measurements to optimize the pitch of rotor blades and yaw of the hub, air quality forecasting improvements with measurements of boundary layer height, tracking the dispersion of potentially hazardous emissions from industrial sites, and increased airport safety and efficiency with observations of wake vortices and wind shears that may be hazardous to aircraft.

The results of this study have significantly improved the performance stability and ease of operation of the original REAL. The instrument is now better equipped to collect measurements during the experiment that will be conducted between June and November 2013 under NSF AGS 1228464.

REFERENCES

REFERENCES

- [1] W. Musial and B. Ram, *Large-Scale Offshore Wind Power in the United States*. The National Renewable Energy Laboratory, 2010. [Online]. Available: <http://www.nrel.gov/wind/pdfs/40745.pdf>
- [2] M. C. Brower, *Offshore Resource Assessment*. John Wiley & Sons, Inc., 2012, pp. 195–219. [Online]. Available: <http://dx.doi.org/10.1002/9781118249864.ch14>
- [3] B. Jimenez, F. Durante, B. Lange, T. Kreutzer, and J. Tambke, “Offshore wind resource assessment with WAsP and MM5: comparative study for the German Bight,” *Wind Energy*, Vol. 10, No. 2, pp. 121–134, 2007. [Online]. Available: <http://dx.doi.org/10.1002/we.212>
- [4] Energy Efficiency and Renewable Energy, “20% wind energy by 2030,” U.S. Department of Energy, 2008. [Online]. Available: http://www.20percentwind.org/20percent_wind_energy_report_revOct08.pdf
- [5] N. Wang, K. Johnson, and A. Wright, “Lidar-based FX-RLS feedforward control for wind turbine load mitigation,” in *American Control Conference (ACC), 2011*, Jul. 2011, pp. 1910–1915.
- [6] Committee on Urban Meteorology: Scoping the Problem, Defining the Needs; Board on Atmospheric Sciences and Climate; Division on Earth and Life Sciences; National Research Council, “Urban meteorology: Forecasting,

- monitoring, and meeting users' needs," 2012. [Online]. Available:
http://www.nap.edu/openbook.php?record_id=13328
- [7] Committee on Developing Mesoscale Meteorological Observational Capabilities to Meet Multiple Needs, National Research Council, "Observing weather and climate from the ground up: A nationwide network of networks," 2009. [Online]. Available: http://www.nap.edu/openbook.php?record_id=12540
- [8] Committee on the Atmospheric Dispersion of Hazardous Material Releases, National Research Council, "Tracking and predicting the atmospheric dispersion of hazardous material releases: Implications for homeland security," 2003. [Online]. Available:
http://www.nap.edu/openbook.php?record_id=10716
- [9] Committee on Low-Altitude Wind Shear and Its Hazard to Aviation, Aeronautics and Space Engineering Board, Atmospheric Sciences and Climate Board, National Research Council, "Low-altitude wind shear and its hazard to aviation," 1983. [Online]. Available:
http://www.nap.edu/openbook.php?record_id=558
- [10] National Academy of Sciences, *Wake Turbulence: An Obstacle to Increased Air Traffic Capacity*. National Academies Press, 2008.
- [11] M. Margulis and T. Baynard, "Clear shear," *Meteorological Technology International*, pp. 74–77, Aug. 2012.
- [12] S. D. Mayor, J. P. Lowe, and C. F. Mauzey, "Two-component horizontal aerosol motion vectors in the atmospheric surface layer from a cross-correlation algorithm applied to elastic backscatter lidar data," *J. Atmos. Ocean. Technol.*, Vol. 29, pp. 1585–1602, 2012.

- [13] K. J. Davis, N. Gamage, C. R. Hagelberg, C. Kiemle, D. H. Lenschow, and P. P. Sullivan, “An objective method for deriving atmospheric structure from airborne lidar observations,” *J. Atmos. Ocean. Technol.*, Vol. 17, pp. 1455–1468, 2000.
- [14] S. D. Mayor, “Raman-shifted Eye-safe Aerosol Lidar (REAL) observations at the Canopy Horizontal Array Turbulence Study (CHATS),” in *18th Symposium on Boundary Layers and Turbulence*. AMS, 2008.
- [15] —, “Horizontal motion vectors from cross-correlation: First application to eye-safe aerosol lidar data from CHATS,” in *25th International Laser Radar Conference*, 2010.
- [16] E. G. Patton *et al.*, “The Canopy Horizontal Array Turbulence Study (CHATS),” *Bull. Amer. Meteor. Soc.*, Vol. 92, pp. 593–611, 2011.
- [17] E. Jaska, “Optimal power-aperture balance,” in *Proc. of the IEEE Radar Conference, 2003*, May 2003, pp. 203–209.
- [18] W. Eberhardt, G. Pressler, and K. Guenther, “Cathode erosion and electrode loss power in pulsed discharges at high pressure,” *Beiträge aus der Plasmaphysik*, Vol. 14, No. 2, pp. 51–54, 1974. [Online]. Available: <http://dx.doi.org/10.1002/ctpp.19740140204>
- [19] *Technical Features*, Sigma Space Corporation, 2011. [Online]. Available: <http://dx.doi.org/10.1002/9781118249864.ch14>
- [20] J. D. Spinhirne, S. Chudamani, J. F. Cavanaugh, and J. L. Bufton, “Aerosol and cloud backscatter at 1.06, 1.54, and 0.53 μm by airborne

- hard-target-calibrated Nd : YAG/ methane Raman lidar,” *Appl. Optics*, Vol. 36, pp. 3475–3490, 1997.
- [21] C. J. Grund and E. W. Eloranta, “University of Wisconsin high spectral resolution lidar,” *Opt. Eng.*, Vol. 30, pp. 6–12, 1991.
- [22] E. W. Eloranta and D. K. Forrest, “Volume-imaging lidar observations of the convective structure surrounding the flight path of a flux-measuring aircraft,” *J. Geophys. Res.*, Vol. 97, pp. 18 383–18 393, 1992.
- [23] C. Weitkamp, *Lidar: Range-Resolved Optical Remote Sensing of the Atmosphere*, Ser. Springer Series in Optical Sciences. Springer, 2005. [Online]. Available: <http://books.google.com/books?id=8AT2smoj4MkC>
- [24] T. H. Maiman, “Stimulated optical radiation in ruby,” *Nature*, Vol. 187, pp. 493–494, 1960.
- [25] E. D. Hinkley, *Laser monitoring of the atmosphere*, Ser. Topics in applied physics. Springer-Verlag, 1976. [Online]. Available: <http://books.google.com/books?id=pNTvAAAAMAAJ>
- [26] W. Gaughan and B. Butka, “Using an FPGA digital clock manager to generate sub-nanosecond phase shifts for lidar applications,” in *Programmable Logic Conference (SPL), 2010 VI Southern*, Mar. 2010, pp. 163–166.
- [27] Y. Lin, J. Hyyppä, and A. Jaakkola, “Mini-UAV-borne lidar for fine-scale mapping,” *Geoscience and Remote Sensing Letters, IEEE*, Vol. 8, No. 3, pp. 426–430, May 2011.
- [28] C. Niclass, A. Rochas, P.-A. Besse, and E. Charbon, “Design and characterization of a CMOS 3-D image sensor based on single photon

- avalanche diodes,” *IEEE Journal of Solid-State Circuits*, Vol. 40, No. 9, pp. 1847–1854, Sep. 2005.
- [29] S. Hernandez-Marin, A. Wallace, and G. Gibson, “Multilayered 3D lidar image construction using spatial models in a Bayesian framework,” *IEEE Transactions on Pattern Analysis and Machine Intelligence*, Vol. 30, No. 6, pp. 1028–1040, Jun. 2008.
- [30] I. Razenkov, H. Cha, D. Kim, and J. Lee, “Measurement of air vertical motion in the atmosphere by aerosol micro pulse lidar,” in *The Pacific Rim Conference on Lasers and Electro-Optics, 1999 (CLEO/Pacific Rim '99)*, Vol. 2, 1999, pp. 139–140.
- [31] J. D. Spinhirne, “Micro pulse lidar,” *IEEE Trans. Geosci. Remote Sensing*, Vol. 31, pp. 48–55, 1993.
- [32] A. Ansmann, “Errors in ground-based water-vapor DIAL measurements due to Doppler-broadened Rayleigh backscattering,” *Appl. Opt.*, Vol. 24, No. 21, pp. 3476–3480, Nov. 1985. [Online]. Available: <http://ao.osa.org/abstract.cfm?URI=ao-24-21-3476>
- [33] V. A. Kovalev and W. E. Eichinger, *Elastic Lidar: Theory, Practice, and Analysis Methods*. Hoboken, NJ: John Wiley & Sons, Inc., 2005.
- [34] C. L. Korb and C. Y. Weng, “A theoretical study of a two-wavelength lidar technique for the measurement of atmospheric temperature profiles,” *J. Appl. Meteor.*, Vol. 21, pp. 1346–1355, 1982.

- [35] P. Rairoux *et al.*, “Remote sensing of the atmosphere using ultrashort laser pulses,” *Applied Physics B*, Vol. 71, pp. 573–580, 2000. [Online]. Available: <http://dx.doi.org/10.1007/s003400000375>
- [36] F. A. Theopold and J. Bösenberg, “Differential absorption lidar measurements of atmospheric temperature profiles: Theory and experiment,” *J. Atmos. Oceanic Technol.*, Vol. 10, pp. 165–179, 1993.
- [37] S. D. Mayor, S. M. Spuler, B. M. Morley, and E. Loew, “Polarization lidar at 1.54-microns and observations of plumes from aerosol generators,” *Opt. Eng.*, Vol. 46, p. DOI: 10.1117/12.781902, 2007.
- [38] E. Burrows and K.-Y. Liou, “High resolution laser lidar utilising two-section distributed feedback semiconductor laser as a coherent source,” *Electronics Letters*, Vol. 26, No. 9, pp. 577–579, Apr. 1990.
- [39] G. Busch *et al.*, “Acousto-optically tuned isotopic CO₂ lasers for long-range differential absorption lidar,” in *Summaries of Papers Presented at the Conference on Lasers and Electro-Optics (CLEO) '97*, Vol. 11, May 1997, pp. 188–189.
- [40] C. Weitkamp, *Lidar: Range-Resolved Optical Remote Sensing of the Atmosphere*. New York: Springer, 2005.
- [41] A. Ansmann, M. Riebesell, and C. Weitkamp, “Measurement of atmospheric aerosol extinction profiles with a Raman lidar,” *Opt. Lett.*, Vol. 15, No. 13, pp. 746–748, Jul. 1990. [Online]. Available: <http://ol.osa.org/abstract.cfm?URI=ol-15-13-746>

- [42] D. N. Whiteman, S. H. Melfi, and R. A. Ferrare, "Raman lidar system for the measurement of water vapor and aerosols in the Earth's atmosphere," *Appl. Opt.*, Vol. 31, No. 16, pp. 3068–3082, Jun. 1992. [Online]. Available: <http://ao.osa.org/abstract.cfm?URI=ao-31-16-3068>
- [43] N. Parikh and J. Parikh, "Reducing uncertainties in aerosol retrievals from micro pulse lidar measurements," in *Geoscience and Remote Sensing Symposium (IGARSS) 2000. IEEE International*, Vol. 2, 2000, pp. 840–842.
- [44] K. Rothe, U. Brinkmann, and H. Walther, "Applications of tunable dye lasers to air pollution detection: Measurements of atmospheric NO₂ concentrations by differential absorption," *Applied Physics A: Materials Science & Processing*, Vol. 3, pp. 115–119, 1974, 10.1007/BF00884408. [Online]. Available: <http://dx.doi.org/10.1007/BF00884408>
- [45] K. Sassen, "Advances in polarization diversity lidar for cloud remote sensing," *Proc. of the IEEE*, Vol. 82, No. 12, pp. 1907–1914, Dec. 1994.
- [46] R. Measures, *Laser remote sensing: fundamentals and applications*, Ser. Wiley-Interscience publication. Wiley, 1984. [Online]. Available: <http://books.google.com/books?id=8Z8sAQAAMAAJ>
- [47] C.-Y. She, "Spectral structure of laser light scattering revisited: Bandwidths of nonresonant scattering lidars," *Appl. Opt.*, Vol. 40, No. 27, pp. 4875–4884, Sep. 2001. [Online]. Available: <http://ao.osa.org/abstract.cfm?URI=ao-40-27-4875>
- [48] A. T. Young and G. W. Kattawar, "Rayleigh-scattering line profiles," *Appl. Opt.*, Vol. 22, No. 23, pp. 3668–3670, Dec. 1983. [Online]. Available: <http://ao.osa.org/abstract.cfm?URI=ao-22-23-3668>

- [49] J. Marshall, T. East, K. Gunn, and W. Hitschfeld, "The effect of particle shape and composition on microwave attenuation and scattering by precipitation," *Transactions of the IRE Professional Group on Antennas and Propagation*, Vol. 3, pp. 180–185, Aug. 1952.
- [50] B. Murphy and W.-J. Kim, "Intuitive representation of gain schedulers to facilitate their design and tuning," in *Proc. of the American Control Conference, 2004*, Vol. 2, Jul. 2004, pp. 1115–1120.
- [51] F. Blanchini and S. Miani, "Gain scheduling versus robust control of LPV systems: The output feedback case," in *American Control Conference (ACC), 2010*, Jul. 2010, pp. 3871–3876.
- [52] V. Alekseyev, S. Babichenko, and I. Sobolev, "Control and signal processing system of hyperspectral FLS lidar," in *11th International Biennial Baltic Electronics Conference (BEC) 2008*, Oct. 2008, pp. 349–352.
- [53] S. D. Mayor and S. M. Spuler, "Raman-shifted Eye-safe Aerosol Lidar," *Appl. Optics*, Vol. 43, pp. 3915–3924, 2004.
- [54] S. D. Mayor, S. M. Spuler, and B. M. Morley, "NCAR's New Raman-Shifted Eye-Safe Aerosol LIDAR (REAL)," in *22nd International Laser Radar Conference (ILRC 2004)*, Ser. ESA Special Publication, G. Pappalardo and A. Amodeo, Eds., Vol. 561, Jun. 2004, p. 53.
- [55] S. D. Mayor *et al.*, "Elastic backscatter lidar observations of a gust front passage over Washington DC on 7 May 2004," in *7th Symp. on the Urban Environment*. AMS, 2007.

- [56] T. Warner *et al.*, “The Pentagon Shield Field Program: Toward Critical Infrastructure Protection,” *Bull. Amer. Meteor. Soc.*, Vol. 88, pp. 167–176, 2007.
- [57] S. M. Spuler and S. D. Mayor, “Scanning eye-safe elastic backscatter lidar at 1.54 microns,” *J. Atmos. Ocean. Technol.*, Vol. 22, pp. 696–703, 2005.
- [58] P. L. Ponsardin, C. S. Kletecka, R. D. Babnick, K. Krubsack, S. D. Mayor, and S. M. Spuler, “Autonomous eye-safe lidar for continuous monitoring of atmospheric aerosols,” in *2006 International Symposium on Spectral Sensing Research (2006-ISSSR)*, 2006.
- [59] S. D. Mayor, P. Benda, C. E. Murata, and R. J. Danzig, “Lidars: A key component of urban biodefense,” *Bio Secur. Bioterror.*, Vol. 6, pp. 45–56, DOI: 10.1089 bsp.2007.0053, 2008.
- [60] R. J. Danzig, “Ideas: Lidar as a lifeline in confronting bioterrorism,” *Bull. Amer. Meteor. Soc.*, Vol. 87, pp. 731–733, 2006.
- [61] S. D. Mayor, “Observations of seven density current fronts in Dixon, California,” *Mon. Wea. Rev.*, Vol. 139, pp. 1338–1351, 2011.
- [62] E. R. Jachens and S. D. Mayor, “Lidar observations of fine-scale atmospheric gravity waves in the nocturnal boundary layer above an orchard canopy,” in *26th International Laser Radar Conference*, Jun. 2012.
- [63] S. D. Mayor, E. R. Jachens, and T. N. Randall, “Lidar observations of fine-scale gravity waves in the nocturnal boundary layer above an orchard canopy,” in *16th International Symposium for the Advancement of Boundary-Layer Remote Sensing (ISARS)*, Jun. 2012.

- [64] T. N. Randall, E. R. Jachens, and S. D. Mayor, “Lidar observations of fine-scale atmospheric gravity waves in the nocturnal boundary layer above an orchard canopy,” in *American Meteorological Society’s 20th Symposium on Boundary Layers and Turbulence*, Jul. 2012.
- [65] S. D. Mayor. (2012) Atmospheric lidar research group. California State University, Chico. [Online]. Available: <http://phys.csuchico.edu/lidar/>
- [66] American National Standards Institute and Laser Institute of America, “American national standard for safe use of lasers: ANSI Z136.1-2000,” 2000. [Online]. Available: <http://books.google.com/books?id=IfIwRAAACAAJ>
- [67] S. M. Spuler and S. D. Mayor, “Raman shifter optimized for lidar at 1.5-micron wavelength,” *Appl. Optics*, Vol. 46, pp. 2990–2995, 2007.
- [68] —, “Eye-safe aerosol lidar at 1.5 microns: progress towards a scanning lidar network,” in *SPIE Lidar Remote Sensing for Environmental Monitoring VIII*, San Diego, CA, 2007, p. DOI: 10.1117/12.739519.
- [69] E. M. Patterson, D. W. Roberts, and G. G. Gimmestad, “Initial measurements using a 1.54 micron eyesafe raman shifted lidar,” *Appl. Optics*, Vol. 28, pp. 4978–4981, 1989.
- [70] W. Carnuth and T. Trickl, “A powerful eyesafe infrared aerosol lidar: Application of stimulated raman backscattering of 1.06 micron radiation,” *Rev. Sci. Instrum.*, Vol. 65, pp. 3324–3331, 1994.
- [71] *NI PXI/PCI-5122 Specifications*, National Instruments, 2004. [Online]. Available: <http://www.ni.com/pdf/manuals/323497b.pdf>

APPENDIX A

APPENDIX A

FUTURE WORK

During the course of this research, several improvements of the lidar that would increase both the quality of backscatter data and reliability and ease of operation were identified. Ten possible improvements are listed and discussed in this Appendix.

Temperature Stabilization

As shown in Fig. 20, the time-series plot of system temperatures and vital signs from the gain scheduler control field experiment, the temperature affects the performance of the instrument. Stability in the temperature of the housing container is highly correlated to transmit pulse-energy and conversion efficiency. It is hypothesized that variations in temperature have a significant impact on instrument performance in the form of thermal lensing of the Nd:YAG rod. The Nd:YAG rod used in this study is relatively long and manifests thermal lensing as the rod is heated more on the axis of the beam than on the outer regions. This temperature variation in the rod causes transverse gradients of the refractive index of the rod. Temperature variations in the laser head accentuate this effect. The Nd:YAG beam divergence is directly related to the beam energy density and conversion efficiency through the Raman cell. Temperature stabilization in the laser head would reduce changing of the thermal lensing of the Nd:YAG rod.

The laser head is cooled with a water circulation system and a heat exchanger that exhausts hot air into the housing container of the lidar. This system circulates about a liter of water through a reservoir and two radiators. The radiators cool the water in direct proportion to the air temperature in the housing container. It is hypothesized that temperature stabilization may be achieved by increasing the size of the reservoir, and therefore the thermal mass of the water that cools the laser head. Also, the heat exchangers could be more isolated so the cooling process would not be so sensitive to slight changes in the air temperature in the housing container.

Real-Time Operating System

The control system of the lidar at CSUC has the ability to substitute the 10 Hz laser with a faster rate laser of 20 to 100 Hz. Incorporating a faster rate laser would require a real-time operating system (RTOS) which would take months to properly configure, test, and implement. Chapter IV discussed this limitation as it pertains to processing constraints and speeds of the control loop. The most viable solution found for RTOS was the NI Real-Time Module. This is a software package that allows a PC to run an RTOS that can be supervised by another PC running Windows 7. The RTOS maximizes the capabilities of the PC to execute a single operation, which in this case is the operation that controls the lidar.

Adding Beam Energies and Conversion Efficiency to BSCAN File Header

This study added beam location, beam radius, and absolute attitude of the housing container platform to the BSCAN file header. At the start of the experiment it was decided that it would also be beneficial to have the Nd:YAG beam and transmit beam energies and the conversion efficiency included in the

header. With these additions, each pulse of the lidar has on record the corresponding beam location, radius, energies, and conversion efficiency, along with the absolute attitude of the platform. As mentioned earlier in this study, these variables are the “vital signs” of performance.

Smaller Flashlamp Voltage Increments

The 11 flashlamp voltage settings limit the quality of the control available for design. This limitation is the result of the manufacturer’s design that offers a simple operator interface. The laser was meant to be adjusted manually, not automatically, which led to the design of crude adjustment increments of 10 volts. However, if the flashlamp voltage could be controlled in increments of 1 volt or even 0.1 volts, the quality of control available would be increased significantly. Modifying circuitry in the Nd:YAG laser power and cooling unit could accomplish. This project should be done in consultation or partnership with the laser manufacturer.

Experiments might also include the feasibility of transmit energy control using the Q-switch delay with or in place of the flashlamp voltage. The Q-switch delay offers a finer incrementation. For example, a range from 225 to 275 μs could be used in increments of 1 μs . The Q-switch delay does not adjust the radiation emitted from the flashlamps, as the flashlamp voltage does, but adjusts the pulse-energy output from the laser head given the radiation from the flashlamps.

Automated Digitizer Resolution

The control system designed in this study allows personnel to change the digitizer resolution (range and offset) without interrupting the continuous operation of the lidar. As the BSU returns from finishing a scan to the start angles

of the next scan, the digitizer is able to recalibrate with the updated resolution settings. A future project will automate this feature to recognize atmospheric conditions and adjust the resolution for optimal data capture. As shown in Fig. 24, the InGaAs detector waveform read by the digitizer is no more than a volt in amplitude. The two settings available for digitizer resolution adjustment are a 1.0 volt range and a 0.4 volt range. InGaAs sensor clipping at long ranges may be used to detect which amplitude would best suit atmospheric conditions. The recalibration would then take place automatically.

Beam Quality Control

In the design presented in this study, the control feature is given the number of pulses on the current set of flashlamps as an input and the flashlamp control voltage is output to the system. Other inputs were explored as possible substitutes for the pulse count. Nd:YAG and transmit beam energies were investigated but proved to have limited dependability. Conversion efficiency (1.5 μm energy exiting the Raman cell divided by 1 μm energy entering) was found to be a more stable and reliable variable that provided a better reflection of the flashlamp control voltage on the beam. This variable could be investigated as a possible input to the gain scheduler flashlamp voltage control. This project would likely be done in conjunction with the temperature stabilization project and/or the smaller flashlamp voltage increments project.

Precision BSU Control

Part of this research included writing the absolute attitude of the housing container platform in the 30 word header of the BSCAN file entries. Currently, this enables data analysts to precisely calculate the beam altitude at

long ranges in post-processing. A similar application could use these measurements to precisely direct the BSU to compensate for platform pitch and roll. The absolute attitude sensors are accurate up to 10^{-6} of a degree and the encoders on the BSU are accurate up to 10^{-4} of a degree. This will provide much more accurate beam placement especially at long ranges. Such capability should be of value in, for example, offshore wind assessments where precise beam pointing is necessary to maintain constant altitude. At a 5 kilometer range, a 1 mm roll in the housing container would displace the beam about 2 meters. An illustration of this effect is shown in Fig. A.1.

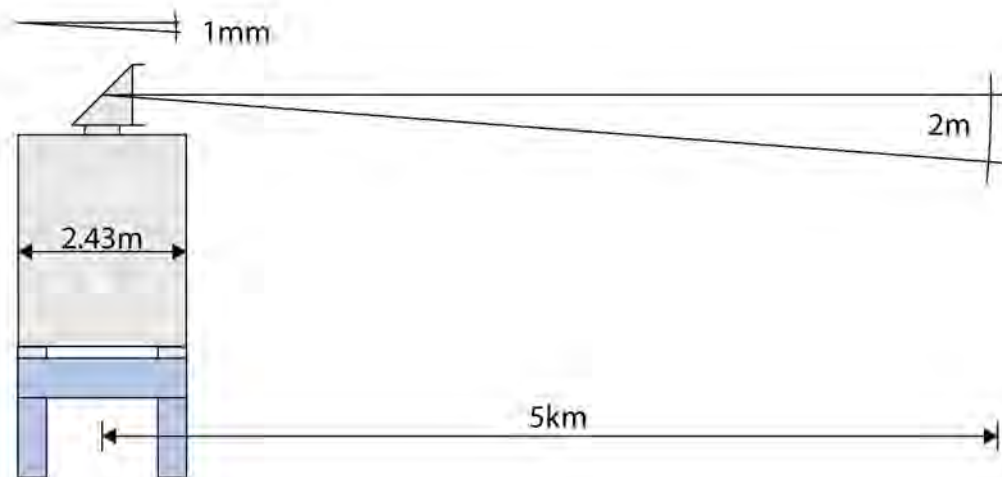


Fig. A.1. An illustration of the effect pitch and roll movements have on the beam at long range. A one millimeter roll in the housing of the container results in a two meter beam displacement at five kilometers range.

Fig. A.2 displays three days of data from the tiltmeters. A daily cycle is noted as the heating of the day and cooling of the night cause the instrument

housing to expand and contract. The left vertical axis indicates the angle of pitch and roll while the right is the corresponding vertical displacement of the beam at a range of 5 km.

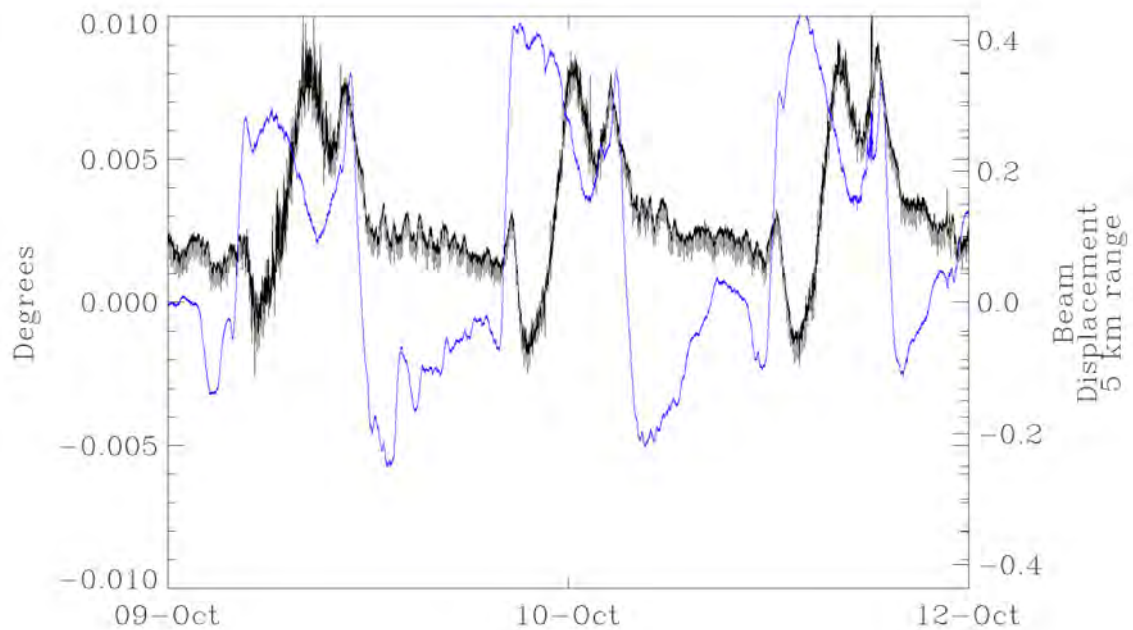


Fig. A.2. A three day time series of tiltmeter measurements for pitch and roll of the instrument housing at the CSUC field site.

The three days plotted in Fig. A.2 were similar in temperature variation and resulted in a beam displacement of less than one meter at five kilometers range. As seasons change temperature variation will increase and, therefore, beam displacement will occur. The pitch and roll of the container is also sensitive to wind and movement of personnel on the platform. During the CHATS experiment of 2007 some roll in the container, due to the semi-truck trailer slowly sinking into the soil, was noticed. Because the system was incapable of sensing its attitude and

automatically compensating for the roll, better wind measurement comparisons with the in situ sonic anemometer could not be made.

GSM Modem Communication

The network connection is used to send email and text notifications. This is sufficient as long as the network does not fail, in which case notifications will not reach personnel. A GSM (wireless) modem incorporated into the system would avoid this problem. If the network failed, the GSM modem would send a message through the wireless network using the nearest cellphone tower. Wireless communication is not part of the present design because of implementation cost and low rate of failure. If the network fails, the control still performs its tasks but personnel will not become aware until they check on the instrument. Another feature that could be included to notify personnel of instrument status is a regular check-in message. At a specific operator-defined interval, the control system would send a message to personnel indicating that everything is in order. Thus, if a message is not received at the end of the defined interval, personnel would know about a problem with the network. A similar solution would include a program on the campus server to verify the connection to the lidar site periodically and notify personnel via SMTP if there is a connection failure.

Interfacing to Security System

It could be beneficial for the system to recognize when the lidar security system has been triggered. The lidar control system could use an analog to digital converter to read an alarm output, such as a siren, and perform a safe shutdown procedure. If the system were in operation and a security alarm were tripped, the control system would perform a safe shutdown procedure.

Scan Interval Timing

There is a need to time the scans to occur at a operator-specified time interval. This feature could be used to stipulate equal amounts of time between scans (necessary for time-series analysis of wind data) or coordinate the scans with other equipment in the field. The scan interval would be required to be longer than the length of the scan. Once the scan is complete the BSU could return to the starting azimuth and elevation angles and wait for the start of the next interval. This has proved difficult to implement due to the asynchronous nature of the BSU motor control commands within the control loop.

APPENDIX B

APPENDIX B

AN OVERVIEW OF THE LABVIEW CODE FOR THE REAL

This appendix contains an overview of the LabVIEW program used to operate the REAL. Mr. Bruce Morley from NCAR wrote the original code. Throughout the course of this study the code has been altered to accommodate the newly developed features. This guide does not discuss all changes that have occurred but only the final program implemented as a result this study. This appendix assumes the reader has a basic knowledge of LabVIEW or signal flow. Due to the graphical nature of LabVIEW, code is somewhat self-explanatory. Unfortunately, LabVIEW is not easily commented. Just a few comments can easily clutter a program. This overview is designed to explain some of the code blocks in the program and how to use them. This is not intended to be an extensive or detailed instruction guide for programming.

Overview

The REAL LabVIEW program is meant to be read on a rotated, wide screen monitor to facilitate navigation. This program implements a state machine with 15 states. The main loop includes 5 of the 15 states. The main structure of the code is a main case structure enclosed in a while loop structure. Each case in the case structure is a state in the state machine. The while loop structure is used to keep the program running and pass information from one state to the next using

shift registers. Shift registers are located at the top of each side of the while loop structure and look like big ports with carrots on them.

The values outside the while loop on the left are initialization variables. The format has to match the format expected in every state by the respective variables. The actual values are not that important since they will be set in the initialization states. The initialization of the DataRay WinCamD is visible at the bottom of the state. Fig. B.1 shows the front panel of the LabVIEW program used to operate the REAL as it would appear on the computer screen. Fig. B.2 shows the code in the first state as it would appear on the computer screen. Table B.1 enumerates the state machine states with states included in the main loop marked with a \star . Fig. B.3 shows the state diagram and Fig. B.4 describes the subroutines of each state.

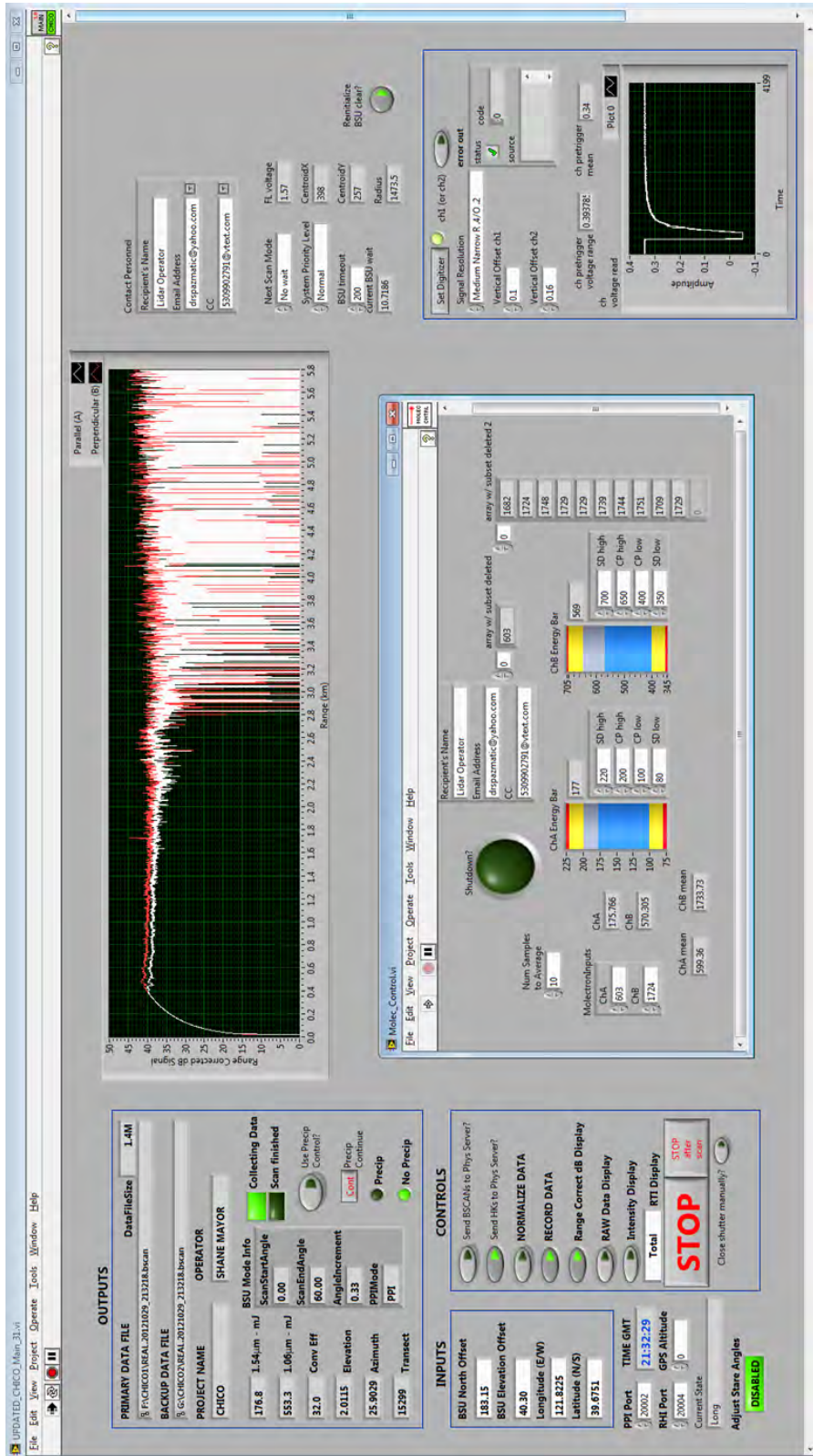


Fig. B.1. Screen capture of the front panel of the LabVIEW program used to operate the REAL.

TABLE B.1
STATE MACHINE STATES

Number	State Name
1	NI PCI Present
2	Open Comm Ports
3	Initialize NI Card
4	Allocate Display Memory
5	Start Laser
6	Start BSU
7	★Start NI Card
8	★Wait For NI Trigger
9	★Long
10	★Short
11	★New Scan
12	Precip Sleep
13	Stop Laser
14	Close Comm Ports
15	Abort

States included in the main loop are indicated with a ★.

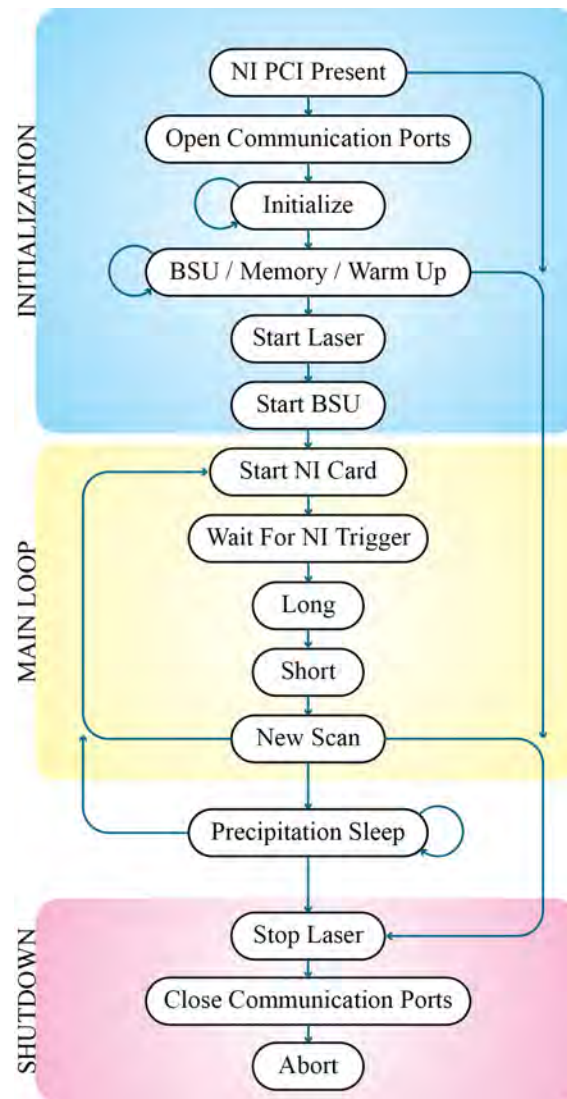


Fig. B.3. State diagram used to operate the REAL as implemented by the program.

NI PCI Present	Open Communication Ports	Initialize	BSU / Memory / Warm Up	Start Laser
Close Safety Shutter Find PCI 5122	BSU Seed Laser Nd:YAG Laser Molelectron Energy Meter Network Broadcast	Display Buffers Nd:YAG Laser Local Directories BSU	BSU to Start Position Turn Flashlamps ON Warm Up Flashlamps Set Molelectron Trigger	Initialize BSCAN and HK files Start Laser Pulses
Start BSU	Start NI Card	Wait For NI Trigger Timing Measurement	Long	Short
	Open Safety Shutter		Normalize Data Calculate SNR Process Data for Display Display Data Read System Variables Write System Variables to HK File	Write to BSCAN File Broadcast on Network
New Scan	Precipitation Sleep	Stop Laser	Close Communication Ports	Abort
Send Files to Server Create New BSCAN File Create New HK File Load Next Scan into BSU Read Precipitation Sensor	Stop Nd:YAG Laser Stop and Stow BSU Wait Until NO Precipitation Restart/Stop	Close Safety Shutter Stop Nd:YAG Laser Stop Seed Laser Stop and Stow BSU	BSU Seed Laser Nd:YAG Laser Molelectron Energy Meter Network Broadcast PCI 5122 Digitizer Close Files	Exit State Machine

Fig. B.4. States with subroutine descriptions.

Initialization

There are 6 initialization states. These states setup the variable formats and operator settings, and calibrate hardware before the system enters the main loop. Initialization states are:

1. NI PCI Present
2. Open Comm Ports
3. Initialize NI Card
4. Allocate Display Memory
5. Start Laser
6. Start BSU

NI PCI Present

The NI PCI Present state verifies that the digitizer is present and operable. If it is not, the system enters the shutdown procedure. In this state the safety shutter is closed. There is no reason for the safety shutter to be open yet.

Open Comm Ports

This state opens the communication and broadcast ports that will be used during operation. The code blocks that read “AZ” and “EL” are the azimuth and elevation angle controls for the BSU motors. Communication ports for the seed laser, Surelite, and Molelectron ports are also opened. The variable “Profiles Recorded” is initialized to zero and the two broadcast ports, “PPI” and “RHI”, are opened.

Initialize NI Card

This is the main initialization state. This state was previously divided into four states. It was decided to combine the four states into one so that only one pop-up start menu would appear each time the system initialized. The main subroutine, “Initialize_Master.vi,” is half-way down on the left side. Once this .vi is complete the initialization values are distributed to the appropriate variables.

The NI PCI-5122 setup is at the top of the event structure inside Initialize_Master.vi as shown in Fig. B.5.

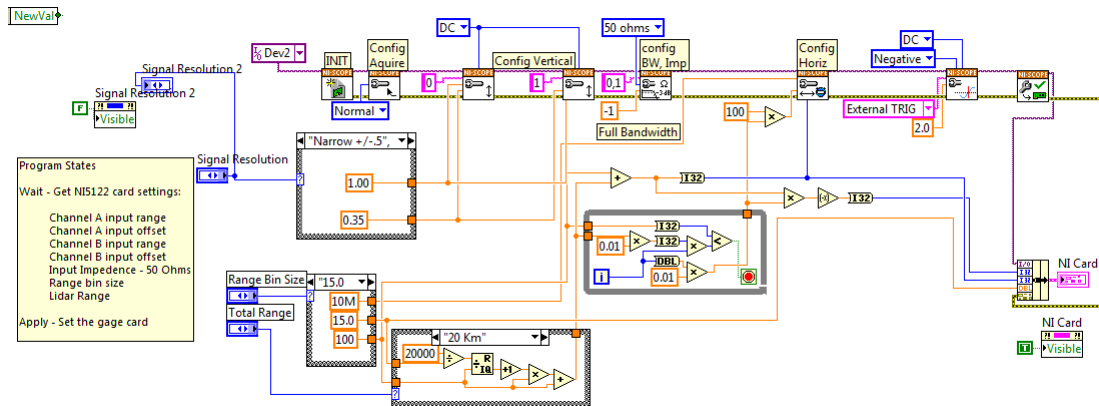


Fig. B.5. NI PCI-5122 initialization code.

This code initializes and configures the digitizer. The vertical configuration determines which voltage range the digitizer will read. The options from the manufacturer's manual are shown in Table 4 [71]. This code allows the operator to choose which calibration settings will be used at the beginning of operation but settings can also be changed once the system is in operation.

Other than the vertical range and offset, the NI PCI-5122 calibration settings need not be changed. A little farther down are the code blocks for the seed laser initialization, the Surelite initialization, and then the flashlamp LUT initialization which is shown in Fig. B.6. The file titled `Flashlamp_LUT.vi` initializes the look-up table (LUT) that the gain scheduler control will use to determine the flashlamp voltage output. Because the flashlamp voltage is such an important part of the system, this initialization process minimizes computation during operation. There are two LUT options: one for a 20 million flashlamp pulse

lifetime expectancy and another for a 30 million flashlamp pulse lifetime expectancy.

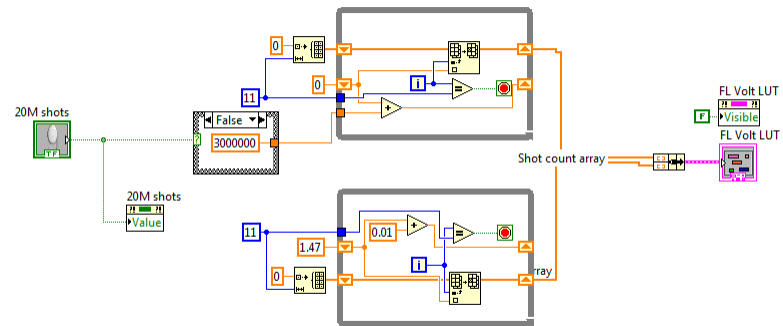


Fig. B.6. Flashlamp LUT Setup

The next step in the procedure is the project directory and file setup, followed by the BSU setup. The routine written for setting the new pulse count after installing new flashlamps is the event structure that follows next in the state.

Allocate Display Memory

This state first directs the BSU to the starting angles of the first scan. Then the history length is set on the intensity chart for readability during operation. The sequential structure starts the flashlamps and lets them warm-up if necessary. The Molectron energy meters are also initialized.

Start Laser

Once the flashlamps have warmed, the laser is started. The system variable measurements file (.hk for house-keeping) and black box file (.bb) are also created and initialized.

Start BSU

With the laser pulsing and the BSU pointed in the initial direction, the scan sequence of the BSU is started without delay.

Main Loop

At this point the program has completed the initialization states and has entered the main loop of the state machine. The states included in the main loop are:

1. Start NI Card
2. Wait For NI Trigger
3. Long
4. Short
5. New Scan

Start NI Card

The first state in the main loop includes a while loop structure, as shown in Fig. B.7, at the top on the left side.

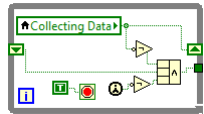


Fig. B.7. Code block produces a TRUE value when the system is not collecting data.

This while loop produces a TRUE signal when the BSU reaches the end of a scan and starts the return motion, or “fly-back.” This boolean variable is used throughout the program to execute processes that will be done during the time the system is not collecting data or as soon as a scan is completed. During the time the

BSU is in fly-back, processes are executed that would not be possible during the scan due to timing restrictions. For example, the vertical configuration of the digitizer is adjusted. This may take long enough that, if done during a scan, the delay may result in the loss of backscatter data. Also, if the configuration is changed during the scan, then part of the scan will have inconsistent resolution with the other part of the scan.

The most important part of this state is the sub .vi called “niScope Initiate Acquisition.vi.” If this is not executed, then the trigger from the Nd:YAG laser will never be seen by the digitizer and the program will be stuck in the Wait For NI Trigger state until manually aborted. The little bit on the bottom is to close the receiver box safety shutter if the elevation angle on the BSU ever drops below zero degrees. This is an attempt to avoid hard target reflections.

Wait For NI Trigger

This is the state that waits for the trigger to be seen by the digitizer so that the digitizer buffer can be read. The while loop inside the sequential structure, as seen in Fig. B.8, is how the program waits for the trigger. There is a time out feature so that if the trigger does not arrive within the allotted time, the problem is recognized and the system is stopped. As soon as the trigger from the digitizer is seen, the azimuth and elevation angles of the BSU are recorded to best represent the beam path in the atmosphere. This is also an appropriate place to manually measure the timing of the process.

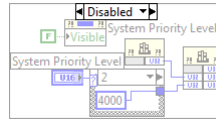


Fig. B.10. System Priority Level Setting

Long

This is the heart of the loop where the majority of computation takes place. It is called long because it is temporally the longest state. Several sections of code require significant time to execute and were combined into one state to enable as much parallel computation as possible. Starting at the top and working down, the code that reads the digitizer buffer is visible.

The block of code shown in Fig. B.11 calculates the signal-to-noise ratio of the captured backscatter data. Disabling this code reduces overall processing time. The SNR is plotted on the same type of chart as the intensity chart. The purpose of this is to compare the SNR from different scans when changing the vertical configuration of the digitizer.

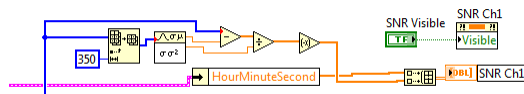


Fig. B.11. SNR code

The next bit of code, shown in Fig. B.12, is used to visually verify digitizer voltage range and offset on the front panel. Adjustments can be made during operation that are implemented in the Start NI Card state.

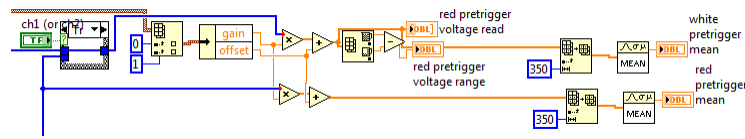


Fig. B.12. ADC Voltage offset

The next piece of code, shown in Fig. B.13, reads the digitizer buffer. At this point the trigger indicates that the digitizer’s buffer contains data that is ready to be read into the program. A `.vi` is used to read the data from the buffer into a 2-D array that is split into the two channels, one for each detector. The next bit of code scales, inverts, and normalizes the data to best represent the backscatter signal received. Normalization takes the background (pretrigger) level of both channels, aligns them, and offsets them to the bottom of the data spectrum. This is often referred to as the raw data. Only offset gain manipulation is performed.

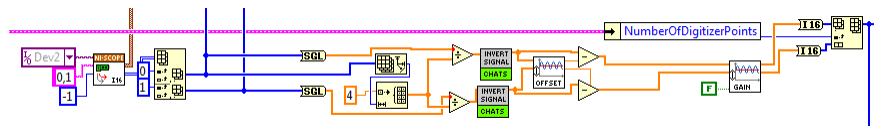


Fig. B.13. Read NI Card

Now the system checks to see if it should be “collecting data.” The code, shown in Fig. B.14, produces a TRUE for the “collecting data” variable if a scan is in progress and not in fly-back. This is done by stating, “If current angle sample is greater than or equal to the previous angle sample, then the system is collecting data, otherwise, the system is not collecting data.” If the current angle sample is less than or equal to the previous sample, then the BSU is in fly-back. If the current angle sample is the same, then the scan is in “stare” mode. If the scan

mode is horizontal then the azimuth angle will be the angle of interest, and if it is vertical the elevation angle will be the angle of interest. If it is a stare then collecting data is always true.

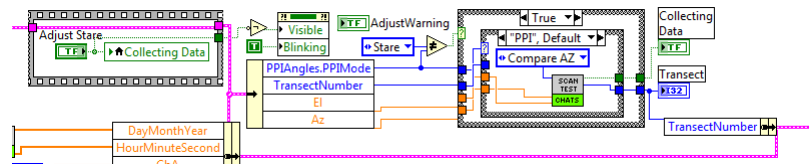


Fig. B.14. Check BSU movement

The Moletron instrument reads the energies of the Nd:YAG laser beam and the transmit beam. The two constants, 3.41 and 3.04, are scale factors for the transmit and Nd:YAG beams, respectively. With these two energy measurement values, conversion efficiency is calculated. The disabled section of code is used for the flashlamp voltage experiment mentioned in the body of the thesis. The system was operated for five minutes on each of the 11 flashlamp voltage levels (1.47, 1.48, ..., 1.56, 1.57 kV). The corresponding energies and conversion efficiencies were plotted in Fig. 14. The code that reads the Moletron measurements is shown in Fig. B.15.

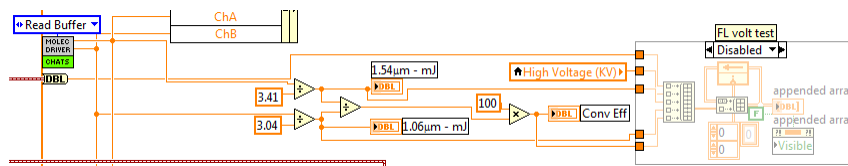


Fig. B.15. Moletron Readings

The next block of code, shown in Fig. B.16, writes the .hk and .bb files. The variables that will be recorded are seen on the left as they are “bundled.” There are two different .hk files because there are two directories. Two .vi’s write the two files because using one .vi to write both files is unnecessarily slow. The file `Housekeeper_2012.vi` sums the values of each variable during the scan and, right before writing the value to the file, the total sum is divided by the number of pulses in the scan to produce an average value of that variable for the scan.

Writing to the .bb files reuses much of the same code as writing to the .hk files. The difference is that the .bb file is written to after each pulse of the laser and, once the file reaches a certain number of pulses (ten minutes worth), it writes in the new values while erasing the oldest values. This records detailed information about the last 10 minutes of operation. The operator may change the amount of time recorded inside the file “black_box.vi.”

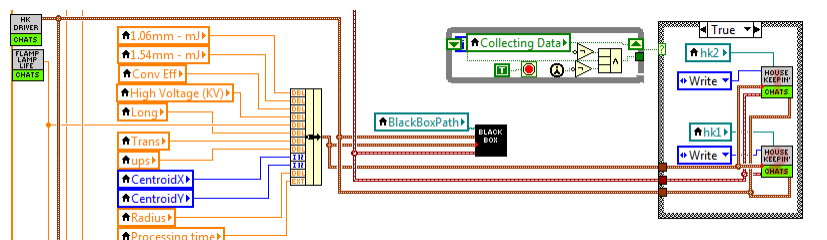


Fig. B.16. House-keeping and black box .vi’s.

The next block of code, shown in Fig. B.17, displays the data on the front panel of the program. The process is to: normalize to the pretrigger, range correct ($\frac{1}{R^2}$), and, since displaying data requires significant processing, determine whether or not to enable the display.

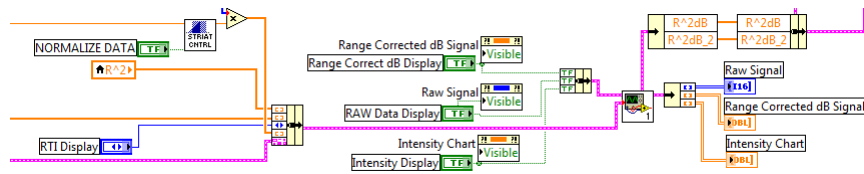


Fig. B.17. Data Display Code

The next block of code, shown in Fig. B.18, is the main control .vi's that were implemented during this research. Here the system decides to continue operating if everything is in order. The variables come in from the left. The .vi's in the middle are the control blocks. Then all the boolean shutdown signals are OR'd together. A "Shutdown Cause" indicator appears on the front panel when there is a shutdown, which facilitates quick identification of failure causes. For every variable there are contact personnel thresholds and shutdown thresholds. The notification emails are a custom part of individual .vi's. This facilitates specificity in the messages sent to personnel. The only control that happens outside this state is the utility power control. It uses FTP to read the utility power on the UPSs, so this process is slow. Fortunately, the UPSs provide power to the system for a half hour following a power outage which provides plenty of time for the failure to be detected before the system is affected. This code is located in the New Scan state and executed when not collecting data.

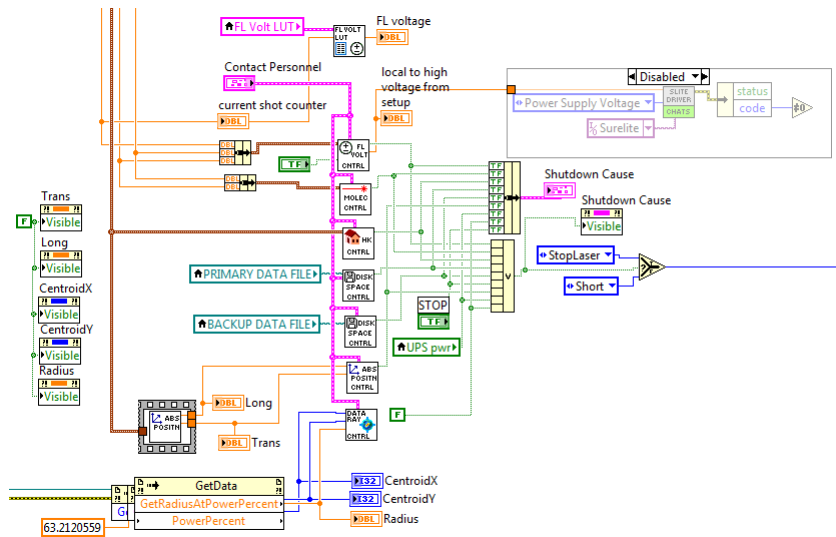


Fig. B.18. Control Block Code

The piece of code at the very bottom, shown in Fig. B.19, is for the DataRay. Because the DataRay code comes from special .dll's from the manufacturer, it cannot be placed in a sub .vi.

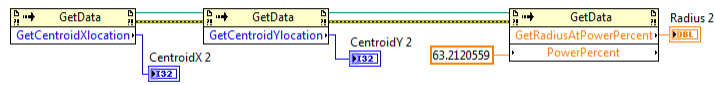


Fig. B.19. DataRay Code expanded

The absolute attitude control .vi at the bottom is in a sequential structure, because it executes only after the file HK_drive.vi has finished using the NI SCC-2345. Two .vi's cannot try to use the device at the same time.

Short

After the Long state, next is the Short state. Two processes take place in this state: write the BSCAN file and broadcast backscatter data. The top part, shown in Fig. B.20, is the BSCAN file write. Most of what is visible is the organization of the header. The header format is described in Table 5. Each BSCAN header word is a 4 byte floating point number. The zeros represent intentional blank slots in the header. Toward the bottom of the state is the broadcast code shown in Fig. B.21.

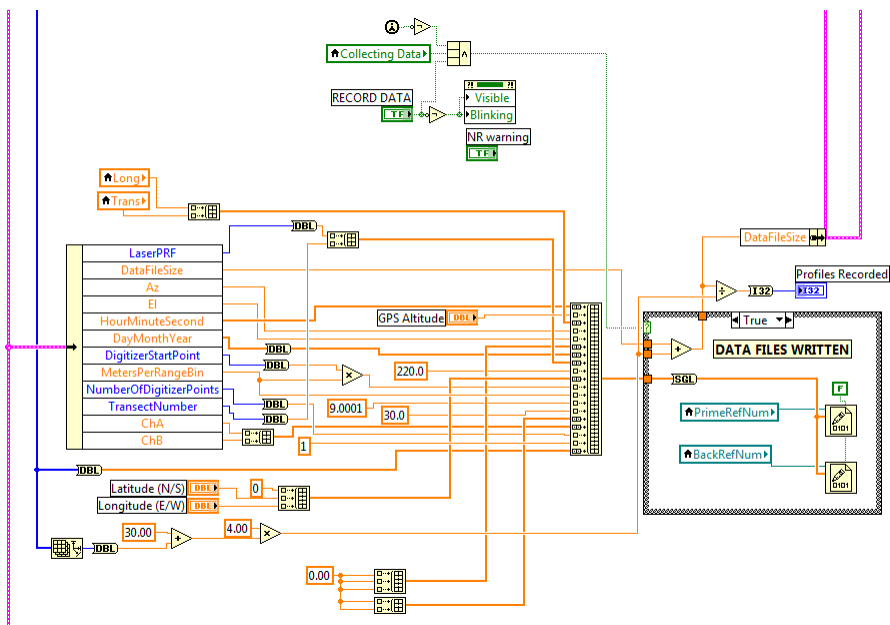


Fig. B.20. Write BSCAN file

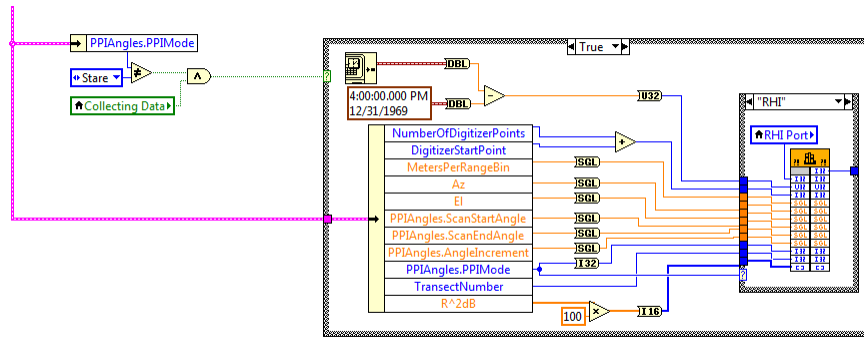


Fig. B.21. Broadcast data

New Scan

Following the Short state is the New Scan state. After each scan, new .BSCAN and .hk files are made. The while loop determines that the scan is completed before a new scan and file are initialized and loaded. This is also the appropriate time to SFTP the files to the server (before closing the current files). The current files are closed and new files are created with appropriate names. The process is the same for both the .BSCAN and the .hk files. The little case structure that closes and deletes the file just created is used when the stop command has been recognized. This is to prevent creating empty files in the directory when the operation is stopped. The code towards the bottom loads the appropriate scan from the scan sequence queue. The corresponding scan commands are sent to the BSU motors.

Precipitation Sleep

This state is not considered a state of the main loop. The little while loop in step 5 is where the system sits and waits for the rain to stop. If the rain doesn't stop after an operator-specified number of minutes, a time out feature will shut down the system. There are two stop buttons to manually abort the sleep

mode and continue operating or shut down. The “Precip Continue” button on the front panel will override the precipitation sleep and continue collecting data even though there is precipitation. The second button is the “STOP” button. This will end the precipitation sleep and stop the system. If the rain does stop in the allotted time, the while loop is exited, the lower code is executed, and the main loop is resumed. During the Precipitation Sleep state the flashlamps pulse, but no laser radiation is emitted from the laser head.

Shutdown

Stop Laser

1. Stop Laser
2. Close Comm Ports
3. Abort

Stop Laser

This state will stop the flashlamps, stow the BSU into a protective posture, stop the seed laser, and wait eight seconds. The eight-second wait is to ensure that the BSU has time to correctly stow before closing the communication ports to the BSU motors.

Close Comm Ports

This state appropriately closes files and communication ports to the Nd:YAG laser, the Molelectron energy meters, and the broadcast ports.

Abort

This state exits the most outer while loop in the program, ending code execution. This is the final state of the state machine.